University of Groningen

Cardiovascular molecular imaging

de Haas, Hans

IMPORTANT NOTE: You are advised to consult the publisher's version (publisher's PDF) if you wish to cite from it. Please check the document version below.

Document Version
Publisher's PDF, also known as Version of record

Publication date:
2018

[Link to publication in University of Groningen/UMCG research database](#)

Citation for published version (APA):
de Haas, H. (2018). *Cardiovascular molecular imaging*. [Thesis fully internal (DIV), University of Groningen]. Rijksuniversiteit Groningen.

Cardiovascular Molecular Imaging

Hans Joachim de Haas

Cardiovascular Molecular Imaging

Proefschrift

ter verkrijging van de graad van doctor aan de
Rijksuniversiteit Groningen
op gezag van de
rector magnificus prof. dr. E. Sterken
en volgens besluit van het College voor Promoties.

De openbare verdediging zal plaatsvinden op

maandag 5 maart 2018 om 12.45 uur

door

Hans Joachim de Haas

geboren op 29 januari 1988
te 's-Gravenhage

Promotores
Prof. dr. R.A.J.O. Dierckx
Prof. dr. R.H.J.A. Slart
Prof. dr. J. Narula

Copromotor
Dr. H.H. Boersma

Beoordelingscommissie
Prof. dr. L. Hofstra
Prof. dr. C.J.A.M. Zeebregts
Prof. dr. H.W. Strauss

Table of contents

Chapter 1

Introduction and outline of the thesis

1. Department of Nuclear Medicine and Molecular Imaging, University Medical Center Groningen, University of Groningen, the Netherlands.
2. Zena and Michael A. Wiener Cardiovascular Institute, Icahn School of Medicine at Mount Sinai, New York, New York.
3. Centro Nacional de Investigaciones Cardiovasculares Carlos III, Madrid, Spain
4. Centre for Inherited Cardiovascular Diseases, I.R.C.C.S Policlinico San Matteo, Pavia, Italy
5. Departments of Medicine and Radiology, University of Virginia Health System, Charlottesville, VA

Molecular imaging

Medical imaging is one of the principal sources of biological information in clinical practice and (bio) medical research. Two imaging paradigms can be distinguished: conventional imaging and molecular imaging. Conventional imaging techniques such as X-ray imaging, magnetic resonance imaging (MRI), and echography employ external sources of energy or radiation such as X-rays, magnetic fields and ultrasound, generating structural images. Molecular imaging allows visualization of biological processes on the cellular and molecular level. It utilizes tracer molecules, which are injected into the living organism and accumulate in tissues in proportion to presence of molecular or cellular targets.

To allow visualization of these phenomena, the tracer molecules are labeled with reporter molecules. Various molecular imaging platforms are available (Table 1).

Molecular imaging platforms

Nuclear imaging

The nuclear imaging techniques single photon emission computed tomography (SPECT) and positron emission tomography (PET) are routinely used in various fields, including oncology, cardiovascular medicine and neurology. These techniques employ radiolabeled tracer molecules, whose radiation signal is detected by cameras positioned or rotating around the patient and processed into tomographic (slices) and 3D images. The nuclear techniques share several advantages including excellent sensitivity ($10^{-10} - 10^{-12}$M) and depth penetration. Their disadvantages include the usage of ionizing radiation and limited spatial resolution. SPECT utilizes gamma ray emitting isotopes including ^{99m}Tc, ^{111}In and ^{123}I. PET utilizes positron emitters including ^{11}C ^{89}Zr and ^{68}Ga and ^{18}F, whose positrons annihilate with nearby electrons, resulting in the release of two 511KeV photons in opposite directions. PET has advantages over SPECT due to absolute quantitation and superior spatial resolution (~ 5mm versus ~ 10mm). Currently, SPECT is generally cheaper and more widely available than PET. For adequate anatomical characterization, integrated SPECT/CT and PET/CT scanners have been developed and have found widespread usage. Recently, the first generation of PET/MRI scanners has appeared. Although PET/MRI is associated with considerable costs, this approach benefiting from the advantages of both advanced imaging techniques holds substantial promise for clinical and academic use.

The work presented in this PhD thesis is focused on nuclear imaging techniques.

Echography

To obtain echo images, ultrasonic sound waves are sent into tissue using a probe. Part of the sound waves bounce back when faced with interfaces between different tissues, and are detected by the probe. A computer is used to construct 2D or 3D images showing tissue structure, movement or blood flow. It is the most widely used conventional imaging modality in clinical cardiology as it is widely available, relatively cheap, has good resolution and does not use ionizing radiation. Molecular echography strategies using targeted microbubbles, liposomes or perfluorocarbon emulsions are also

being developed. Although this allows for high-sensitivity (~ 10^{-12} M) imaging, the relatively large size of these contrast agents largely restricts this modality to vascular imaging.

Magnetic resonance imaging

For MRI imaging, the subject is placed in an MRI scanner and exposed to a strong static magnetic field. This puts the hydrogen atoms in the body's water molecules in the equilibrium state; aligned with the magnetic field. The scanner also repeatedly emits radiofrequency pulses, which knock part of the hydrogen atoms out of the equilibrium state. After each pulse, hydrogen atoms revert to the equilibrium state through T1 and T2 relaxation. The MRI scanner detects T1 and T2 signals, which are processed into tomographic and 3D images. Advantages of MRI include excellent spatial (~ 1mm) and temporal resolution, soft-tissue contrast and the fact that no ionizing radiation is used. To further enhance contrast, (super)paramagnetic molecules such as gadolinium and iron oxide, which alter the magnetic properties of surrounding atoms are used. In cardiovascular medicine, several non-targeted gadolinium agents are clinically used for detection of cardiac scarring. Given the toxicity of free gadolinium, the gadolinium ions need to be chelated or sequestered into macrocyclic molecules. (Super)paramagnetic molecules have also been used to label tracer molecules, to allow molecular MRI imaging. Low sensitivity of MRI imaging ($10^{-3} - 10^{-5}$ M) limits this approach and necessitates use of large doses contrast agents. However, signal enhancement strategies are progressing and render molecular MRI a viable approach, especially for intravascular imaging.

Computed tomography

Computed Tomograpy (CT) utilizes X-ray source and detector combinations, which are positioned on opposite sides of each other on a ring which rotates around the subject. The resulting collection of X-ray data is combined to generate tomographic images. Advantages of CT imaging include high resolution (0.5-1.0mm), short acquisition time (less than one minute with state-of-the-art scanners), widespread availability and cost-effectiveness. CT imaging, enhanced with iodinated contrast agents is extensively used in clinical cardiovascular medicine, to visualize vascular anatomy and pathology. Drawbacks of CT imaging are nephrotoxicity of iodinated contrast agents and radiation burden (although the latter is decreasing with technological progress). Targeted contrast agents based on iodine and other X-ray annihilators have also been developed. Of the modalities described in this section, molecular CT has the lowest sensitivity ($10^{-1} - 10^{-2}$ M), which poses a formidable challenge. And although initial pre-clinical studies have appeared, translation to clinical studies is still awaited.

Optical imaging

Optical imaging is based on the detection of photons, either transmitted or reflected by the reporter molecules. Various distinct subcategories have been developed including near-infrared fluorescence imaging, diffuse optical tomography, diffuse optical spectroscopy, confocal microscopy. Optical imaging has excellent sensitivity ($10^{-10} - 10^{-12}$ M) and spatial resolution and does not involve ionizing radiation. The limited tissue penetrance (mm – cm) restricts clinical non-invasive optical imaging to superficial bodily structures. However, optical imaging during invasive procedures such as surgery, endoscopy or

catheterization is emerging. As the limited penetrance is less relevant in small-animal models, optical imaging is widely used in preclinical research.

Modality	Imaging agents	Resolution	Penetrance	Cost
Echo	Microbubbles	+	Cms	€
CT	Iodinated	++	Unlimited	€€
MRI	Paramagnetic particles	++	Unlimited	€€€
Optical	Fluorochromes	+	Mm-cms	€-€€€
SPECT	Gamma emitters (e.g. ^{99m}Tc, ^{111}In)	--	Unlimited	€€
PET	Annihilation gamma emitters (e.g. ^{18}F, ^{64}Cu, ^{68}Ga)	-	Unlimited	€€€

Table 1. General comparison of molecular imaging platforms. CT = computed tomography; MRI = Magnetic resonance imaging; PET = positron emission tomography; SPECT = single photon emission computed tomography.

Clinical and academic uses of molecular imaging

Given the direct biological information yielded by molecular imaging, it can be employed to optimize disease phenotyping and subsequent personalization of clinical management. However, given the inherent drawbacks of molecular imaging including radiation burden, contrast toxicity, cost, time-consumption, substantial expected impact on clinical management of individual patients is required to justify molecular imaging in standard clinical practice. Thus, molecular imaging will likely be largely limited to situations where stakes are high, such as the identification of patients who would benefit from surgery interventional treatment or other potent therapies carrying high cost or risk.

Molecular imaging is also an excellent tool tool for pre-clinical and clinical research. It is increasingly used to evaluate the (temporal) role of specific cellular or molecular targets in pathologic processes, thereby playing a hypothesis-generating role in development of novel diagnostic, preventative and therapeutic strategies. Moreover, molecular imaging is emerging as a tool in development/validation of such strategies by guiding patient selection for studies, serving as a gold standard to compare novel diagnostic approaches with and providing a mechanistic read-out for (novel) therapeutic or preventative regimens.

Molecular imaging of cardiovascular disease part I: atherosclerosis

Atherosclerosis, a chronic inflammatory disease of the arterial wall characterized by the formation of atherosclerotic plaques, is the driver of cardiovascular disease and the main cause of myocardial infarction. Currently, treatment of atherosclerosis is guided by risk factor-based cardiovascular risk scores, and conventional imaging techniques such as ultrasound, CT angiography and coronary angiography. However, these strategies are inadequate to detect patients who would benefit from aggressive therapy to prevent myocardial infarction, as large proportions of plaques causing events (culprit plaques) are too small to cause clinical symptoms or be identified as obstructive by conventional

imaging strategies.

Histological studies have identified a number of characteristics of plaques with higher risk of rupture ("vulnerable plaques") (1,2). These include the presence of inflammatory cells, a thick necrotic core, cell death, angiogenesis, and the presence of a thin fibrous cap covering the necrotic core. Initially, research focused on the development of molecular imaging strategies to identify the individual plaques at high risk of rupture ("vulnerable plaques") to guide (invasive) therapy at the single-plaque level. However, it has been established that only a very small percentage of plaques with a high-risk morphology result in the occurrence of events. Therefore, the attention has shifted towards using molecular imaging to identify vulnerable patients by measurement of atherosclerotic disease activity across larger portions of the vascular bed (3,4). Moreover, molecular imaging has been used study pathology of atherosclerosis and to evaluate the efficacy of novel therapies.

Physiological imaging: myocardial perfusion and metabolism

As perfusion and metabolism are physiological processes, imaging strategies focusing on these phenomena are distinguished from molecular imaging as "physiological imaging". However, as nuclear perfusion and metabolism imaging are vital components of the diagnostic arsenal for identification and (invasive management) management of coronary artery disease (5-7), they deserve to be mentioned here. ^{99m}Tc-sestamibi, ^{99m}Tc-tetrofosmin and ^{201}Tl were the first perfusion tracers to be developed for gamma imaging and later SPECT imaging. They are still the most widely used worldwide, although PET imaging using ^{13}N-NH3 and ^{82}Rb are emerging as their replacement in developed countries (8,9). Besides nuclear imaging techniques, perfusion imaging by CT (10,11) and MRI (12,13) are also being developed. A standard myocardial perfusion imaging exam consists of rest scan and a stress scan following physical exertion or administration of a vasodilator such as adenosine. This allows distinction of

infarcted, reversibly ischemic and normally perfused myocardial regions. Thereby, myocardial perfusion imaging informs clinical decision-making regarding pharmacological management and invasive procedures aimed at restoring cardiac perfusion (i.e. including percutaneous coronary intervention (PCI) and coronary artery bypass graft surgery (CABG)).

Perfusion imaging is often combined with PET imaging after administration of ^{18}F-2-Fluoro-2-Deoxy-D-Glucose (^{18}F-FDG). The cellular accumulation of this glucose analog is relative to the rate of cellular metabolism. ^{18}F-FDG uptake in regions with reduced perfusion indicates their viability and in selected cases justifies PCI or CABG.

Inflammatory cells

As the infiltration of inflammatory cells is the driving force of the atherosclerotic disease process and also one of the main characteristics of high risk plaques (14,15), considerable effort has gone into development of imaging techniques to visualize inflammatory cells.

^{18}F-FDG PET is the most widely used molecular imaging technique. A glucose analog, ^{18}F-FDG accumulates in tissues proportionally to the rate of cellular sugar metabolism. As such, it is established as an imaging tracer to diagnose, stage and monitor cancer (16,17), detect various types of infection

(18) and evaluate cardiac viability (19).

As macrophages are the most metabolically active cells in the inflamed vascular wall, ^{18}F-FDG PET has also been extensively evaluated as an imaging tracer to visualize vascular inflammation. The correlation between vascular ^{18}F-FDG uptake and vascular macrophage content has been demonstrated in atherosclerosis, aortic aneurysms (20), and vasculitis (21).

Retrospective studies in oncologic cohorts have shown that vascular ^{18}F-FDG uptake correlates with cardiovascular risk factors (22) and predicts occurrence of cardiovascular events (23,24). A prospective study confirmed the predictive value of FDG: in 60 patients with symptomatic carotid artery stenosis, stroke reoccurrence was higher with increased FDG uptake in the ipsilateral plaque (25).

The value of ^{18}F-FDG PET to evaluate the effect of novel anti-inflammatory therapies for the treatment of atherosclerosis is also increasingly recognized. PET imaging studies have revealed reduced vascular ^{18}F-FDG uptake after initiation of treatment with statins (Figure 1) (26,27) and pioglitazone (28,29). These drugs also have shown beneficial effects in hard-endpoint based studies (30,31). On the other hand, no reduction in vascular ^{18}F-FDG uptake was seen after treatment with a lipoprotein-associated phospholipase A2 inhibitor (32) and the cholesteryl ester transfer inhibitor dalcetrib (33). These drugs did not confer a beneficial effect in hard-endpoint studies (34,35). Thus, vascular ^{18}F-FDG uptake is an attractive surrogate marker for atherosclerosis therapy trials.

Although ^{18}F-FDG imaging of larger arteries is widely established, coronary imaging remains a challenge because of physiological ^{18}F-FDG uptake in the myocardium. Diet-based strategies are used to suppress this uptake, but are unsuccessful in sometimes over 50% of cases (36). Further strategies are continually developed, but this remains a drawback of ^{18}F-FDG imaging.

Besides FDG, several other inflammation tracers have been developed. One promising tracer is ^{68}Ga-DOTATATE. This tracer binds to the somatostatin receptor and is used clinically in the management of neuroendocrine tumors. As this receptor is also present on subgroups of macrophages (37), it may also find a role in vascular imaging. An initial retrospective study in an oncologic cohort revealed feasibility of identifying active coronary atherosclerosis using this tracer (38). Moreover, a recent small-scale prospective study confirms that atherosclerotic plaque uptake of this probe reflects macrophage infiltration, and suggests that it superior to ^{18}F-FDG for coronary imaging and identification of high-risk coronary lesions (39).

Another modality that deserves mention is MRI using ultra small superparamagnetic particles of iron oxide (USPIO). These particles are taken up by macrophages, and have been exploited for identification of these cells vascular disease. Initial studies indicate feasibility of identifying unstable plaques (40-42) and monitoring effect of anti-inflammatory therapy (43). However, low sensitivity (especially because of intense blood pool images) and long duration of imaging protocols are current challenges for this technique. Finally, initial reports suggest the feasibility of assessing coronary plaque vulnerability (44) and inflammation (45) by CT-based measurement of pericoronary adipose tissue. ^{18}F-FDG PET imaging was used as the gold standard for detection of coronary inflammation (45), illustrating the potential of molecular imaging techniques for the development of novel diagnostic stragegies with lower cost and radiation burden.
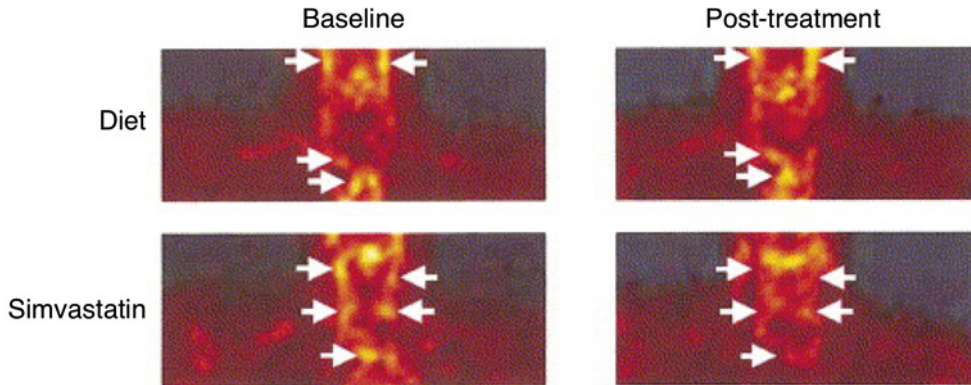
Figure 1. ^{18}F-FDG PET imaging to evaluate the effect of simvastatin on human atherosclerotic plaque inflammation. ^{18}F-FDG PET imaging was performed in patients with carotid atherosclerosis before (baseline, left column) and after three months of treatment (post-treatment, right column) with dietary management (diet, top row) or simvastatin (bottom row). Dietary management did not affect ^{18}F-FDG uptake (arrows) in the aortic arch and the carotid arteries. Simvastatin attenuated ^{18}F-FDG uptake (arrows) in the carotid arteries and aortic arch. ^{18}F-FDG = ^{18}F-2-Fluoro-2-Deoxy-D-Glucose; PET = Positron Emission Tomography. Adapted from (26).

Apoptosis

Apoptosis is a genetically programmed, highly organized form of cell death morphologically characterized by cell shrinkage, chromatin condensation, chromosomal DNA fragmentation, and finally cellular fragmentation into apoptotic bodies which are cleanly removed by inflammatory cells. Although apoptosis plays a vital role in tissue development and cellular turnover, it's also implicated in various pathological processes. In atherosclerotic plaques, it drives plaque destabilization through contributing to formation of the necrotic core and stimulating the inflammatory response. Thus, apoptosis has been used as a diagnostic and therapeutic target for unstable atherosclerotic plaques.

Several imaging tracers have been developed for detection of apoptosis. The most widely studied of these is ^{99m}Tc-annexin A5, which targets the membrane-bound apoptosis marker phosphatidyl serine (PS). Initial studies in atherosclerotic rabbits (46) and swine (47) demonstrated feasibility of atherosclerotic plaque imaging using this tracer. Histologic analyses correlation of ^{99m}Tc-annexin A5 uptake and markers of apoptosis and macrophage infiltration.

Next, a small-scale clinical study using ^{99m}Tc-annexin A5 imaging in patients with cerebrovascular accident (CVA) was performed. It revealed more intense radiotracer uptake and histological characteristics of plaque instability in culprit plaques at 3 – 4 days than at 3 – 4 months post-CVA (48). This demonstrated feasibility of detection of unstable plaque using ^{99m}Tc-annexin A5 and supports the concept that unstable plaque, even after giving rise to acute events, can develop to stable morphology.

Also, animal studies have shown that *in vivo* ^{99m}Tc-annexin A5 imaging can be used to demonstrate efficacy of anti-apoptotic pharmacotherapy (49) and statins (50).

Finally, animal studies have used radiolabeled annexin A5 and a molecular tracer targeting matrix metalloproteinases (MMP) to demonstrate relation between two targets. These studies are described in the following section.

Matrix metalloproteinases

MMP are a group of zinc-dependent proteases that degrade various components of the extracellular matrix and thereby allow cell migration and extracellular matrix remodeling necessary in physiologic tissue development and remodeling. However, they are also up regulated in various pathologic states, resulting in tissue destruction. In the case of atherosclerosis, MMP are usually derived from macrophages and contribute to growth of the necrotic core and thinning of the fibrous cap, thus contributing to atherosclerotic plaque advancement and vulnerability to rupture. As such, MMP have been targeted in atherosclerosis.

Extensive preclinical experience has been obtained with the wide spectrum MMP-inhibitor RP805 labeled with [99m]Tc. Initial feasibility studies in atherosclerotic rabbits (51) and mice (52) demonstrated arterial ^{99m}Tc-RP805 and that uptake corresponds to MMP activity and macrophage infiltration. Subsequent animal studies showed that ^{99m}Tc-RP805 SPECT can be used to monitor the effect of dietary and pharmacological therapy (51,53) and to predict development of plaque size over time in MMP imaging (54). Finally, two studies have compared uptake of ^{99m}Tc-RP805 and ^{111}In-annexin A5 in atherosclerotic rabbits (55) and mice (56), showing a correlation between uptake of the two tracers and higher absolute ^{99m}Tc-RP805 uptake. ^{99m}Tc-RP805 has also been used to visualize MMP activity in animal models of aortic aneurysm (57), myocardial infarction (58), aorta stenosis (59) and pulmonary inflammation (60).

Besides nuclear imaging, other molecular imaging platforms have been evaluated for MMP targeting. P947, a broad spectrum MMP inhibitor, has been labeled with gadolinium. Feasibility of MMP targeting in atherosclerotic plaques has been shown in atherosclerotic rabbits, mice and *ex vivo* in human excised carotid plaques (61-64). Moreover, several probes have been developed for optical imaging of MMP (65,66).

Calcification

Another hallmark of atherosclerotic disease is presence of (micro)calcifications. Conventional CT is the gold standard to detect vascular calcifications. CT detects presence of calcifications larger than ~ 200 −500 μm (67). Although total coronary calcium (expressed as coronary artery calcium score) is a marker of atherosclerotic disease burden and predicts outcomes, presence of macro calcification does not correspond with plaque instability (68). Micro calcifications, tiny calcium deposits of < 50 μm, cannot be detected by CT but constitute a highly attractive imaging target as they are correlated with accelerated atherosclerosis and plaque instability (69). In this regard, ^{18}F-Sodium Fluoride (^{18}F-NaF) PET, which is used clinically to detect primary and secondary bone malignancies, may serve as a complement to vascular CT. The ^{18}F ion binds directly to hydroxyapatite, and thus allows detection of vascular micro calcifications. Moreover, ^{18}F-NaF PET can and can distinguish early, active macrocalcifications from more advanced, stabilized calcifications (67). Retrospective studies have shown that global vascular ^{18}F-NaF uptake corresponds with vascular risk factors and cardiovascular outcome (70,71). Moreover, studies regarding patients with stroke and myocardial infarction have revealed higher uptake in the culprit plaques giving rise to the events than the asymptomatic plaques (Figure 2) (72,73). This indicates

that increased ^{18}F-NaF uptake may correspond with an unstable plaque subtype. An important clinical advantage of ^{18}F-NaF is that its physiologic uptake into the myocardium is negligible, which results in excellent coronary imaging characteristics.
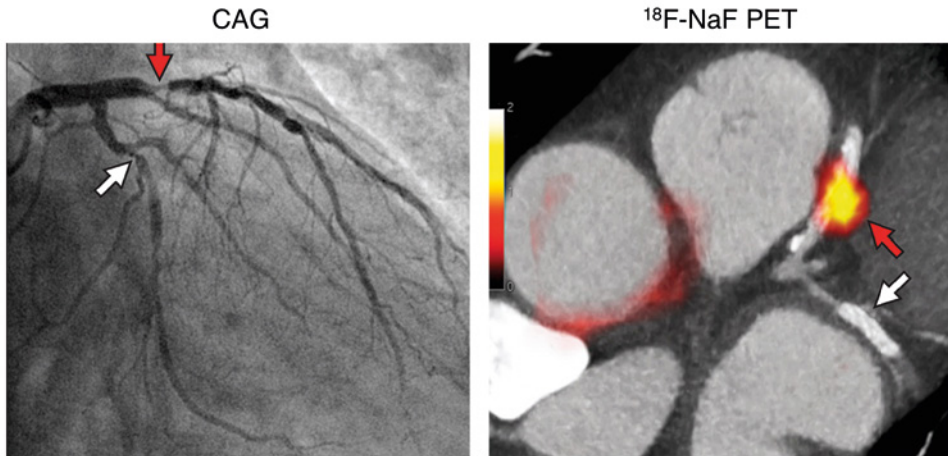

Figure 2. Coronary ^{18}F-NaF PET imaging in a patient with acute myocardial infarction. Coronary angiography (CAG, left panel) in a patient with anterior non-ST-segment elevation myocardial infarction revealing culprit (red arrow; left anterior descending artery) and bystander non-culprit (white arrow; circumflex artery) lesions; both were stented afterwards. ^{18}F-NaF PET (right panel) was performed after both vessels were stented and revealed increased radiotracer uptake in the culprit lesion (red arrow), but not in the bystander non-culprit lesion (white arrow). ^{18}F-NaF = ^{18}F-sodium fluoride; CAG = coronary angiography. Adapted from (72).

Angiogenesis

Neovascularization is another hallmark of unstable plaques. The newly formed vessels contribute to plaque advancement and destabilization by allowing entrance of lipid particles, red blood cells, and inflammatory cells into the plaque (74). For visualizing of angiogenesis, most research has focused on imaging tracers containing the sequence arginine-glycine-aspartate (RGD). This tripeptide binds to $\alpha_v\beta_3$ integrin, which is present on proliferating endothelial cells, but also on macrophages (75), platelets (76) and myofibroblasts (77).

Following substantial pre-clinical and clinical work focused on tumor angiogenesis imaging using ^{18}F-galacto-RGD PET, initial studies have evaluated this probe for atherosclerosis imaging.

Two studies in atherosclerotic mice revealed feasibility of targeting atherosclerotic plaques and monitoring the effect of dietary intervention (78,79). Interestingly, intraplaque angiogenesis was not observed in these studies; ^{18}F-galacto-RGD uptake correlated with extent of macrophage presence. Next, ^{18}F-galacto-RGD PET imaging was performed in ten patients with high grade stenotic carotid plaques, scheduled for carotid endarterectomy. In the five patients with increased radiotracer uptake, uptake corresponded with degree of stenosis and of $\alpha_v\beta_3$ integrin expression (80).

Although ^{18}F-galacto-RGD is an interesting tracer for research purposes, its time consuming production process likely prevents its use in clinical practice. Recently feasibility of targeting newly formed vessels using ^{18}F-RGD-K5 has been reported (81). This tracer is similar to ^{18}F-galacto-RGD, but has a faster

and more straight-forward labeling procedure. Also, feasibility of atherosclerosis imaging in mice and patients using ^{68}Ga-NOTA-RGD, a novel PET tracer, has recently been reported (82). Finally, several RGD based probes to allow MRI (83,84) and SPECT (85) and optical imaging (86,87) have been developed. As the uptake of RGD-based imaging probes reflects angiogenesis or macrophages, it may be regarded as a non-specific marker of the unstable plaque. The role of this imaging approach needs to be established by further research.

Thrombus

Endothelial damage triggers platelet activation and a fibrin-forming coagulation cascade, which converge in the formation of thrombi. These fibrin-laced platelet plugs in turn serve to restore endothelial integrity. Inappropriate or excessive formation of thrombus is the cause of myocardial infarction, cerebrovascular accident, deep venous thrombosis and pulmonary emboli. Therefore, various markers of platelet activation and players in the coagulation cascade have been exploited as imaging targets.

Initial reports of clinical thrombus imaging using fibrin-targeted SPECT tracers were published three decades ago (88,89). More recently, substantial experience has been obtained with molecular MR imaging using the gadolinium-based nanoparticle EP-2104R. Feasibility of thrombus detection with this nanoparticle has been demonstrated in > 5 different animal models of arterial and venous thrombosis (90-95). Subsequently, clinical feasibility of thrombus imaging was shown in a small group of patients with arterial, venous and cardiac thrombi (96). In addition, feasibility of SPECT (97,98) and PET (99) imaging using fibrin-targeted peptides has been reported. Besides fibrin, the fibrin-producing enzyme thrombin (100,101) and fibrin-crosslinking coagulation factor XIIIa (102,103) have been evaluated as targets for thrombus imaging in the preclinical studies.

Activated platelets have also been targeted, using ultrasound (104,105), SPECT (106,107) and MRI (108,109) probes specific for Glycoprotein IIb/IIIa. It remains to be seen whether activated platelets are or fibrin is the optimal target for the molecular imaging of thrombus. If the sensitivity of fibrin-targeted probes proves too low to clinically detect older thrombi with lower fibrin content, platelet imaging may prove to be superior. However, if fibrin targeting is sensitive enough even to detect the older plaques, its advantage of predicting effect of thrombolytic therapy may become decisive.

Molecular imaging of cardiovascular disease part II: myocardial injury and remodeling

Myocardial infarction is caused by the acute occlusion of a coronary artery, usually as a result of rupture of an atherosclerotic plaque and subsequent formation of an occlusive thrombus (110). Timely restoration of blood flow (reperfusion) salvages part of the ischemic myocardium, but also triggers cell death in a subset of cardiomyocytes (a process called ischemia/reperfusion injury) (111).

Currently, the main therapeutic goal for acute myocardial infarction is to achieve reperfusion, preferably by PCI. The widespread implementation of this catheter-based technique has substantially improved survival rates of patients with myocardial infarction.

The repair process after myocardial infarction is traditionally divided into three consecutive and partly overlapping phases. During the first (inflammatory) phase, inflammatory cells infiltrate the tissue and removing cellular debris. During the second (proliferatory) phase, fibroblasts transdifferentiate into myofibroblasts, which deposit collagen in the infarct area. In the third (maturation) phase, the newly formed fibrous scar is consolidated through cross-linking of collagen fibers and other extracellular matrix components.

The extracellular matrix plays an important role in the healing process and an imbalance between matrix deposition and degradation can lead to adverse myocardial remodeling spiraling to heart failure. Excessive collagen deposition beyond the infarct area (remote fibrosis) contributes to myocardial stiffening and loss of contractile function. On the other hand, inadequate deposition of collagen or excessive collagen degradation can lead to infarct expansion, aneurysm formation, LV dilation and even cardiac rupture.

Currently, no cardio-protective drugs are available to complement reperfusion therapy in the acute setting of myocardial infarction. To reduce remodeling after myocardial infarction and prevent heart failure, virtually all infarction patients are treated with a combination of a beta-blocker and a modulator of the renin-angiotensin-system. Molecular imaging strategies may aid development of novel drugs and personalize treatment.

Apoptosis and necrosis

As myocardial infarction results in substantial cell death, various cell death imaging tracers have been developed and used in this setting. The first studies focused on imaging of necrosis, an uncoordinated process usually initiated by sudden cell stress, pathogenic insult or energy depletion. It is characterized by loss of cellular homeostasis, swelling and eventually rupture of the cell membrane resulting in spilling of cellular contents triggering an intense inflammatory response.

Most experience was obtained with ^{111}In-labeled antimyosin, a single chain murine antibody fragment targeting myosin. When the cardiomyocyte cell membrane is disrupted this probe gains access to the intracellular space, where it accumulates through binding with myosin. After extensive studies in animal models, clinical feasibility of cardiac cell death imaging using this tracer was shown not only in patients with myocardial infarction but also with myocarditis (112), transplant rejection (113), doxorubicin

cardio toxicity (114) and dilated cardiomyopathies (115). It was approved for clinical use for diagnosis of myocardial infarction, however it has never been widely used. The main reason for this was the slow blood clearance, which necessitated imaging of cell death after > 9 hours (and preferably 24 – 48 hours) after injection, and the discovery of serum biomarkers for myocardial infarction. However, it has been used in pre-clinical studies to gain insight in biochemical processes of cell death in myocardial infarction (see below). Besides antimyosin, several other radiotracers have been evaluated for clinical detection of myocardial infarction, including [99mTc]-glucarate (116) and [99mTc]-pyrophosphate (117), however development halted after the first clinical feasibility trials.

After the discovery that besides necrotic cell death, apoptotic cell death also plays a role in myocardial infarction, this type of cell death has also been targeted for imaging. As in atherosclerosis, the main imaging probe for apoptosis was [99mTc]-annexin A5. Preclinical studies in animal models of acute myocardial infarction showed feasibility of targeting PS overexpression using fluorescently labeled annexin A5 (118,119) and with radiolabeled annexin A5 in animal models of heart and lung transplantation (120). Next, two preliminary clinical studies were undertaken using [99mTc]-annexin A5 imaging in myocardial infarction patient (Figure 3) (121,122). Both studies employed [99mTc]-annexin A5 SPECT imaging immediately after PCI and reported strong [99mTc]-annexin A5 uptake in the infarct area as identified by myocardial perfusion imaging. Although the larger scale studies required for approval for clinical usage were never performed, the [99mTc]-annexin A5 studies have contributed to knowledge of cell death in ischemia through raising relevant research questions and triggering further mechanistic (imaging) studies. In the first clinical myocardial infarction imaging study mentioned above, a surprising finding was the increased uptake in the entire perfusion defect. Until then, necrosis was thought to be the main type of cell death, especially in the core of the infarct. Although different explanations were also proposed, it resulted in the speculation that apoptosis and necrosis constitute a continuum, with initiation of apoptotic signaling during early ischemia and a switch to a necrotic phenotype at a later timepoint (123). This was further evaluated in a study employing a rat model of cardiac ischemia (20 min) followed by reperfusion (124). Rats received [99mTc]-annexin A5, [111In]-antimyosin or both and subgroups received the tracers at varying timepoints after onset of reperfusion. The study revealed colocalization of [99mTc]-annexin A5 and [111In]-antimyosin, with [99mTc]-annexin A5 uptake peaking at an earlier timepoint than antimyosin. This supported the hypothesis that apoptotic signaling precedes necrotic cell death in the ischemic myocardium.

The second clinical study revealed that the region of increased [99mTc]-annexin A5 uptake after the acute ischemic event extended to beyond the limits of the perfusion defect as shown by [99mTc]-sestamibi SPECT at three weeks after the event, suggesting that even advanced apoptotic signaling may be reversible. This was later studied in a rabbit model of ischemia and reperfusion. Using varying ischemia durations, the investigators confirmed that brief ischemia resulted in reversible [99mTc]-annexin A5 expression and cellular survival. This supported the search for anti-apoptotic drugs to complement reperfusion therapy in the setting of acute myocardial infarction (125,126).
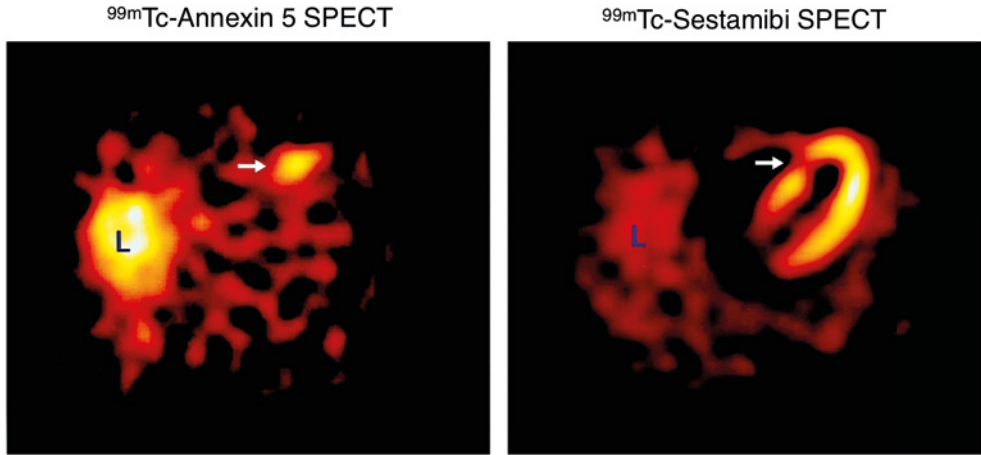
Figure 3. Cardiac ^{99m}Tc-annexin A5 imaging in a patient with myocardial infarction. ^{99m}Tc-annexin A5 imaging (left panel) at < 24 hours after reperfusion revealed increased cardiac radiotracer uptake (arrow). ^{99m}Tc-sestamibi imaging (right panel) at 6 – 8 weeks after discharge revealed an irreversible perfusion defect, corresponding to the area with of increased ^{99m}Tc-annexin A5 uptake (arrow). Adapted from (121).

Collagen

Imaging of collagen is of interest, as it is the main component of fibrous tissue. Clinically, MRI is used to detect localized scarring by late gadolinium enhancement, and detection of diffuse fibrosis by T1 mapping is emerging (127). For Targeted collagen imaging by MRI after administration of the gadolinium-labeled peptide EP-3533 has been demonstrated in various animal models of organ fibrosis (128-130). Notably, visualization of cardiac scarring by EP-3533 has been demonstrated in a mouse model of myocardial infarction (Figure 4) (131). Dynamic MRI at 6 weeks after myocardial infarction revealed probe uptake in the infarcted areas, with longer retention than non-targeted gadolinium.

CNA35 is another collagen-avid peptide with high affinity to collagen-I. CNA35-based probes have been used for targeting of vascular collagen in animal models of abdominal aneurysm, atherosclerosis and colon cancer using MRI, two-photon laser scanning microscopy, and γ-imaging, respectively (132-134). Also, feasibility of identifying cardiac scar using CT imaging enhanced by gold labeled CNA-35 has been demonstrated in mice with myocardial infarction.

Finally, feasibility of collagen imaging in a mouse model of myocardial infarction by SPECT using a ^{99m}Tc-labeled peptidomimetic of platelet collagen receptor glycoprotein VI called collagelin has been shown (135).

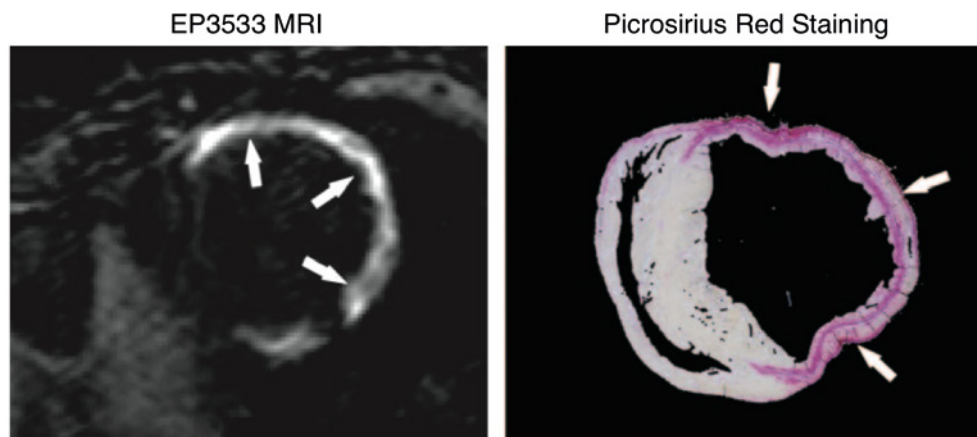**Figure 4.** Targeted MRI imaging of cardiac collagen in a mouse with myocardial infarction. MRI imaging (left panel) after administration of nanoparticle EP3533 in a mouse at 6 weeks after experimental myocardial infarction, revealed marked regional cardiac contrast enhancement (arrows). Picrosirius red staining in midventricular section of same mouse (right panel) confirmed collagen deposition in the region of contrast enhancement. Adapted from (131).

Myofibroblasts and renin-angiotensin-system

During cardiac remodeling, cardiomyocytes and other cardiac cells produce angiotensin II, which binds to the angiotensin II receptor type 1 (AT1R), which in the myocardium is mainly present on myofibroblasts and fibroblasts. This induces TGF-β, which is responsible for the fibroblast differentiation into a collagen-secreting myofibroblast subtype, and cardiomyocyte hypertrophy (136-138). As the renin-angiotensin-system and myofibroblasts are key determinants of fibrosis, they have been extensively evaluated as cardiac imaging targets.

First angiotensin converting enzyme (ACE), the enzyme responsible for splicing angiotensin I into active angiotensin II, was visualized using lisinopril-based nuclear imaging probes to visualize in sections of explanted hearts of patients with ischemic cardiomyopathy undergoing heart transplantation (116) and in ACE overexpressing transgenic rats (139,140).

Also, successful targeting of AT1R to visualize the cardiac myofibroblast has been shown. In an initial study in mice with experimental myocardial infarction, fluorescently labeled angiotensin peptide analog (APA) and 99mTc-labeled losartan were evaluated (141). Probe accumulation was increased from week 1-12 after myocardial infarction, peaking at 3 weeks. Accumulation was histologically traced to myofibroblasts. Although this is an interesting proof of principle study, ^{99m}Tc-losartan's target-to-background ratio of 2.5 is likely too low for imaging of myocardial scarring in the clinical situation. More recently, this work was expanded using KR31173, a non-peptide AT1R selective antagonist (SK-1080) labeled with [11]C (142). In a pig model of myocardial infarction, increased myocardial retention of this tracer in the infarct and remote areas were observed (142). Pilot clinical imaging experiments in healthy volunteers showed that KF31173 could detect cardiac AT1R, although blocking studies suggested limited specificity of the compound.

Besides the AT1R receptor, $\alpha_v\beta_3$ integrin has been targeted for visualization of myofibroblasts. For the

proof of concept, the fluorescently and radiolabeled ^{99m}Tc-Cy5.5 RGD imaging peptide (^{99m}Tc-CRIP) was used in mice with experimental myocardial infarction (Figure 5) (143). Increased uptake was observed in the infarct area, peaking at 2 weeks after myocardial infarction. Interestingly, a trend of increasing uptake over time in the remote uptake was observed, indicating that it may become possible to target remote remodeling. Histologic studies confirmed binding of the peptide to myofibroblasts and correlation between tracer uptake and collagen deposition. In a subsequent study, ^{99m}Tc-CRIP imaging was used to evaluate the therapeutic effects of captopril, losartan and spironolactone, individually or in combination (144). Treatment groups demonstrated reduced tracer uptake, which correlated with collagen deposition and echo parameters of adverse remodeling. Finally, clinical feasibility of myofibroblast imaging using of ^{99m}Tc-CRIP without the Cy5.5 label (RGD imaging peptide, RIP) was shown in ten patients with myocardial infarction (Figure 5) (145). In five patients, increased radiotracer uptake was seen in the infarct area as shown by myocardial perfusion imaging, corresponding to myocardial scarring at 1 year as shown by late gadolinium enhancement (LGE) MRI.

Because $\alpha_v\beta_3$ integrin is also expressed on endothelial cells of proliferating vessels, RGD tracers have also been explored for imaging of angiogenesis after myocardial infarction in rats and dogs (146,147). Similar to the ^{99m}Tc-CRIP studies, uptake peaked at 3 weeks after myocardial infarction. Uptake correlated with histologic markers of angiogenesis, but mechanism of tracer targeting was not demonstrated. As angiogenesis and fibrosis often occur hand in hand, it is likely that in some instances, both mechanisms contribute to tracer uptake. One further study revealed that ^{18}F-galacto-RGD uptake was a significant predictor of increase in MRI-verified left ventricular end-diastolic diameter at 12 weeks (148) and finally feasibility of cardiac ^{18}F-galacto-RGD imaging was demonstrated in one patient at two weeks after myocardial infarction (149).
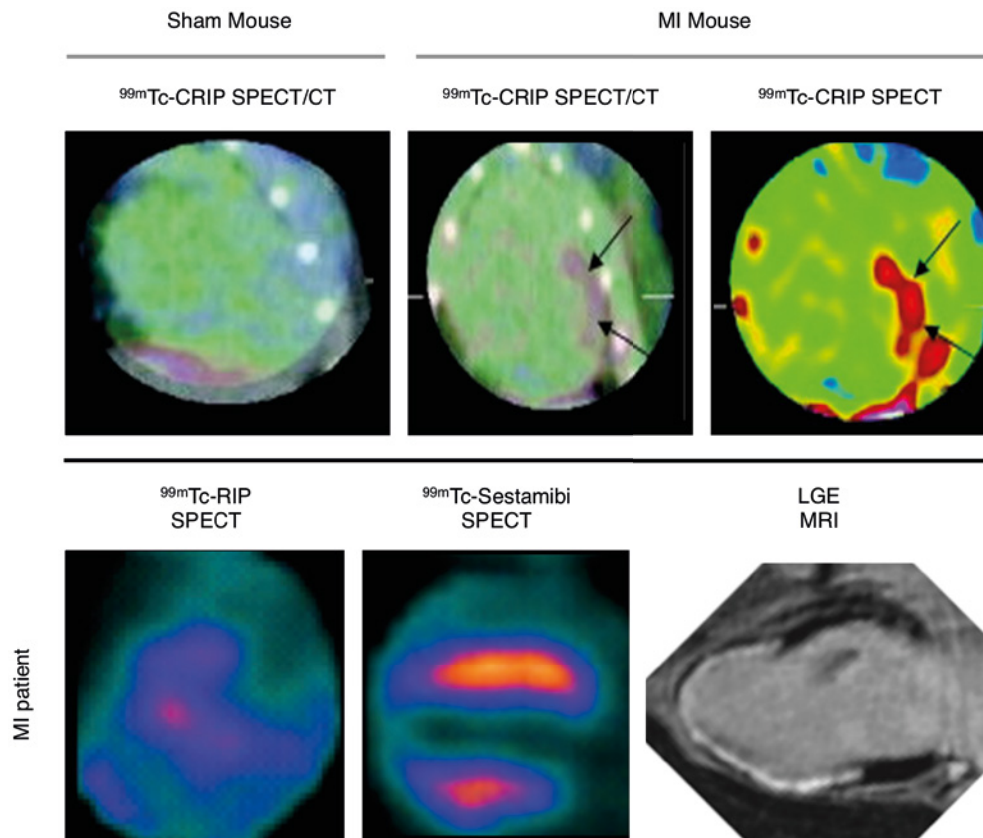
Figure 5. Targeted imaging of αvβ3 integrin to show myofibroblasts in experimental and clinical myocardial infarction. Top row: SPECT/CT imaging after administration of $\alpha_v\beta_3$-avid ^{99m}Tc-Cy5.5 RGD imaging peptide (CRIP) to a control mouse (left panel) showed no radiotracer uptake, whereas SPECT (middle panel) and SPECT/CT (right panel) imaging in a mouse at 4 week after myocardial infarction showed intense cardiac CRIP uptake. Adapted from (143).
Bottom row: SPECT imaging after administration of ^{99m}Tc-RGD imaging peptide (RIP; left panel) to a patient 3 weeks after myocardial infarction revealed apical uptake, extending beyond the infarct area (perfusion defect) as demonstrated by ^{99m}Tc-sestamibi myocardial perfusion imaging (middle panel) and corresponding to the area of fibrosis as shown by late-gadolinium enhanced (LGE) MRI at 1 year after myocardial infarction (right panel). Adapted from (145).
^{99m}Tc-CRIP = ^{99m}Tc-Cy5.5 RGD imaging peptide; ^{99m}Tc-RIP = RGD imaging peptide; LGE = late gadolinium enhancement; MI = myocardial infarction.

Matrix metalloproteinases

MMP upregulation during remodeling allows adaptive changes such as infiltration of cellular debris-removing inflammatory cells, migration of cardiomyocytes and myofibroblasts, angiogenesis and novel matrix deposition, and counterbalances (excessive) deposition of extracellular matrix components. However disproportionate MMP-induced degradation of extracellular components can lead to wall thinning, dilatation and predispose to heart failure, or aneurysm formation and cardiac rupture.

Targeting of cardiac MMP activity has been reported using optical imaging (150) and nuclear imaging

(58,151,152) probes. Besides atherosclerosis and other models of cardiovascular disease, MMP-inhibitor ^{99m}Tc-RP805 was used for imaging of myocardial infarction in a mouse model (58). When comparing with control mice, uptake in infarct area was five-fold higher from week $1 - 3$, with a slight reduction over time. Interestingly, uptake was also two-fold higher in remote area, suggesting that remote imaging could become feasible. A follow-up study employing a porcine myocardial infarction model, revealed a similar uptake pattern and development over time (151). Magnetic resonance imaging (MRI) roughly paralleled radiotracer uptake with global contractile dysfunction at 1 week, normalization of remote function at 2 weeks and only akinesia and dyskinesia in the infarct area at 4 weeks. More recently, *in vivo* targeting of MMP in mice with myocardial infarction has been proposed with an activatable cell-penetrating peptide probe (152). Gamma counting and autoradiography revealed a ten-fold higher uptake of the activated probe in the infarct over remote area. As this uptake is more than three-fold higher than that reported for the RP805 studies, this might evolve as an attractive imaging strategy. However, these results are still preliminary as biodistribution studies revealed considerable uptake in vasculature and liver, and no *in vivo* imaging was performed.

Sympathetic innervation

The heart is innervated by parasympathetic and sympathetic nerves. Evidence is mounting that damage to cardiac innervation plays a role in various cardiac pathologies including remodeling after myocardial infarction (153). ^{123}I-meta-iodobenzylguanidine (^{123}I-MIBG), a norepinephrine analog has been employed for evaluation of cardiac innervation. Like norepinephrine, this molecule enters neurons through the norepinephrine transporter-1, but unlike norepinephrine accumulates intracellular and allows for imaging (154). ^{123}I-MIBG imaging is usually performed by anterior planar imaging with global cardiac uptake being expressed semi-quantitatively as heart/mediastinum ratio (HMR) (155). Studies in heart failure patients have consistently shown increased mortality in patients with reduced cardiac ^{123}I-MIBG accumulation (HMR < 1.6) (156-158). ^{123}I-MIBG may contribute to clinical decision-making regarding higher-cost and risk interventions. For instance, ^{123}I-MIBG imaging may contribute to identification of heart failure patients who will benefit from implantable cardioverter-defibrillators, as HMR is an independent predictor of occurrence of and mortality resulting from ventricular tachycardia and fibrillation (155,157,159,160). Currently, a large-scale clinical trial is ongoing to test this hypothesis (admire ICD). Also, initial studies have shown that ^{123}I-MIBG imaging may improve selection of heart failure patients to receive cardiac resynchronization therapy (161,162). However, results are preliminary and the mechanism is unknown. Besides ^{123}I-MIBG, several PET radiotracers, including ^{11}C-meta-hydroxyephedrine (163), ^{11}C-epinephrine (164) and ^{18}F-labeled LMI1195 (16), have been developed for imaging of cardiac sympathetic innervation and may eventually replace ^{123}I-MIBG imaging.

Conclusions

Extensive pre-clinical experience has been obtained with molecular cardiovascular imaging. Notably, in atherosclerosis, inflammation, proteolysis, angiogenesis and ongoing calcification have been targeted. In the setting of myocardial infarction and subsequent repair and adverse remodeling, cell death, collagen, proteolysis, and various players involved in fibrosis have been visualized. A substantial number of these techniques were used in turn to study pathology over time or evaluate efficacy of novel therapies.

Molecular cardiovascular imaging is increasingly being translated to the clinic. Indeed, molecular imaging in atherosclerosis is reaching maturity. For instance, predictive value of vascular ^{18}F-FDG PET imaging has been established and this probe is increasingly being used in clinical therapy trials and imaging of ongoing calcification using ^{18}F-NaF bears promise as a clinical predictor of cardiac events. In the setting of myocardial infarction, clinical imaging of cell death using ^{111}In-antimyosin was even approved for clinical use, although it has faded again because of insufficiently favorable imaging characteristics and emergence of biomarkers of myocardial infarction.

Molecular imaging is a fascinating set of techniques to study pathology, evaluate the efficacy of (novel therapies) and personalize medicine, that will likely have an increasingly important influence of cardiovascular research and clinical practice.

Outline of the thesis

In this thesis, the following aspects of molecular imaging in cardiovascular disease were studied:

Feasibility of imaging vascular inflammation using ^{18}F-2-fluoro-2-deoxy-D-mannose (^{18}F-FDM) PET in a rabbit model of atherosclerosis. (see chapter 2)

Molecular imaging of cell death using ^{99m}Tc-annexin A5 to visualize cardioprotective effects of the tetracycline antibiotic minocycline in rabbit and mouse models of acute myocardial infarction (see chapter 3)

Molecular imaging of cell death using ^{111}In-labeled 4-(N-(S-glutathionylacetyl)amino) phenylarsonous acid (^{111}In-GSAO) in rabbit and mouse models of acute myocardial infarction and a mouse model of chronic myocardial infarction (see chapter 4)

Molecular imaging of cell death using ^{111}In-GSAO to visualize cardioprotective minocycline in rabbit and mouse models of acute myocardial infarction (see chapter 5)

Chapter 2

[18]F-2-Fluoro-2-Deoxy-D-Mannose Positron Emission Tomography Imaging in Atherosclerosis

Hans J. de Haas[1,2],*, Nobuhiro Tahara[3],*, Jogeshwar Mukherjee[4],*, Artiom D. Petrov[1], Ahmed Tawakol[5], Nezam Haider[1], Atsuko Tahara[3], Cristian C. Constantinescu[4], Hendrikus H. Boersma[2], Tsutomu Imaizumi[3], Masataka Nakano[7], Aloke Finn[6], Zahi Fayad[1], Renu Virmani[7], Valentin Fuster[1,9], Lisardo Bosca[8], Jagat Narula[1]

1.   Mount Sinai School of Medicine and Medical Center, New York, New York;
2.   University of Groningen, University Medical Center Groningen, Groningen, Netherlands;
3.   Kurume University School of Medicine, Kurume, Japan;
4.   University of California, Irvine and Medical Center, Irvine, California;
5.   Harvard Medical School and Massachusetts General Hospital, Boston, Massachusetts;
6.   Emory University School of Medicine and Medical Center, Atlanta, Georgia;
7.   Cardiovascular Pathology Institute, Gaithersburg, Maryland;
8.   Instituto de Investigaciones Biomédicas Alberto Sols (Centro Mixto CSIC-UAM), Madrid, Spain
9.   Centro Nacional de Investigaciones Cardiovasculares Carlos III (CNIC), Madrid, Spain

* Authors contributed equally

Abstract

Progressive inflammation in atherosclerotic plaques is associated with increasing risk of plaque rupture. Molecular imaging of activated macrophages with ^{18}F-2-deoxy-2-fluoro-D-glucose (^{18}F-FDG) has been proposed for identification of patients at higher risk for acute vascular events. Mannose is an isomer of glucose that is taken up by macrophages through glucose transporters and because mannose receptors are expressed on a subset of the macrophage population in high-risk plaques, we hypothesized that ^{18}F-labeled mannose (^{18}F-2-deoxy-2-fluoro-D-mannose, ^{18}F-FDM) would be superior to ^{18}F-FDG for targeting of plaque inflammation. Here, we describe comparable uptake of ^{18}F-FDM and ^{18}F-FDG in atherosclerotic lesions in a rabbit model; ^{18}F-FDM uptake was proportional to the plaque macrophage population. Moreover, FDM competition studies in cultured cells with ^{14}C-2-deoxy-2-carbon-D-glucose (^{14}C-CDG) support at least 35% higher ^{18}F-FDM uptake by macrophages. We also demonstrate that FDM restricts binding of anti–mannose receptor antibody to macrophages by approximately 35%, indicating that mannose receptor targeting may provide an additional avenue for imaging of plaque inflammation.

Introduction

Macrophage-rich inflammation is an obligatory component of active atherosclerotic plaques and is particularly intense in the high-risk plaques associated with acute coronary events and symptomatic carotid vascular disease (14,165-168) Positron emission tomography (PET) imaging using radiolabeled glucose (^{18}F-2-deoxy-2-fluoro-D-glucose, ^{18}F-FDG) (169,170) has been employed for visualization of vascular inflammation and identification of high-risk plaques, as well as for the demonstration of the efficacy of pharmaceutical interventions (26,33). ^{18}F-FDG PET imaging is based on the higher metabolic glucose demand of macrophages than that of their surrounding cells in the plaque; and upregulated hexokinase (HK) facilitates increased radiolabeled glucose accumulation, mostly through the glucose transporters (GLUTs) (171).

Although ^{18}F-FDG imaging is a convenient and widely investigated strategy, the quest for new, potentially more specific targeting agents for the detection of plaque inflammation has continued (46,48,172-176). At least two types of macrophages are observed in atherosclerotic plaques: the proinflammatory M1 subtype (including lipid-triggered foam cells) and the anti-inflammatory M2 subtype (177,178). A subset of macrophages, especially M2, express mannose receptors (MRs) (177,178). As these macrophages are common in lesions with neovascularization and intraplaque hemorrhage (177).

Mannose and glucose are C2-epimeric sugar molecules; their structures differ only in the opposite orientation of oxygen and hydroxyl groups on the second carbon atom (Figure 1a,b). Like glucose, mannose enters cells through GLUTs (179) and is a substrate of hexokinase (180). Therefore, we hypothesized that PET imaging of atherosclerotic plaques using radiolabeled mannose would show macrophage metabolism similarly to ^{18}F-FDG PET and would offer added specificity to the imaging of high-risk atherosclerotic plaques by targeting the MR-bearing macrophages that are abundant in such lesions. Accordingly, we synthesized (^{18}F-2-deoxy-2-Fluoro-D-mannose, ^{18}F-FDM) by applying a straightforward

2

protocol similar to the one used for ^{18}F-FDG production. We evaluated ^{18}F-FDM imaging for inflammation in atherosclerosis in an experimental model. Because intraplaque hemorrhage rarely occurs in any experimental models of atherosclerosis, upregulation of MR expression may not be easily induced in preclinical studies. Therefore, we designed our *in vivo* imaging experiments to describe the non-inferiority of ^{18}F-FDM imaging as compared to ^{18}F-FDG imaging. In addition, we performed cell culture studies comparing FDM and FDG metabolism in macrophages under various conditions mimicking the atherosclerotic plaque microenvironment. We also evaluated FDM binding to the MRs. Finally, we immunohistochemically evaluated MR expression in atherosclerotic lesions of varying severity derived from humans after sudden cardiac death.

Methods

Histopathological evaluation of human coronary plaques.

This study was exempted from the provisions of the CVPath Institute Human Use Committee, as it involved material from nonliving subjects. The IRB has reviewed the research protocols of the characterization of the atherosclerotic plaques involving specimens collected from postmortem material and provided an exemption letter indicating that it was aware of the work with the de-identified human specimens and that universal precautions were strictly followed. The enrollment involved examination of sudden coronary death cases received in consultation from the Maryland Medical Examiner Office and added to the Sudden Coronary Death Registry. We obtained the coronary specimens from 5 patients 53.8 ± 13.3 years of age (4 males). Morphology of each plaque was characterized by modified Movat's pentachrome staining. For immunohistologic characterization, we cut adjacent cryosections at 10 µm. After treating the sections with 0.15% H_2O_2 and protein block (Dako, Denmark), we incubated the sections using primary antibodies against CD68 (Dako, clone KP1, 1:800), CD163 (Santa Cruz, clone GHI/61, 1:800) and CD206 (HyCult Biotechnology, clone 15-2, 1:800). For detection of primary antibody binding, we used a streptavidin–alkaline phosphatase 4plus Universal Detection System (Biocare Medical), and for visualization we used a Ferangi Blue chromogen substrate (Biocare Medical). Antibody binding for cryosections used either an EnVision + Dual Link System HRP (Dako) or Universal LSAB 2 HRP (Dako), both with a NovaRed chromogen (Vector). For analysis of the stained sections, we used an Olympus BX51 microscope equipped with a wide-format liquid-crystal display and the following objective lenses: PlanApo 1.25×/0.04 numerical aperture (NA), PlanApo 2×/0.08 NA, UPlanApo 4×/0.16 NA, UPlanFl 10×/0. 30 NA, UPlanFL N 20×/0.50 NA and UPlanFl 40×/0.75 NA. We used an Olympus DP71 camera and DP Controller imaging software (version 3.2.1.276) to capture images. After white-balancing on digital imaging software, we acquired images including entire coronary cross-sections at 20× magnification (432 d.p.i., bit depth 24) in the same setting (ISO-200, exposure time 1/800 s). In each plaque, we further photographed 2 macrophage-rich regions of interest at a magnification of 400× (4,080 × 3,072 pixels, 432 d.p.i., bit depth 24, ISO-200, exposure time 1/280 s). We assessed presence of CD68, CD163 and CD206 (expressed as average of area density) in 200 × 200 µM areas within these regions of interest using IPLab for Mac OS X.

Macrophage culture experiments

The Institutional Review Board of Hospital La Paz, Madrid, Spain, approved all macrophage culture experiments. We obtained peripheral blood from healthy volunteers (50 mL from each) with their written informed consent, through the blood bank Cruz Roja, Blood Bank, Madrid, Spain. We obtained monocytes from buffy coats by Ficoll-Paque (density 1.077 g/ml) (GE Healthcare Bio-Sciences Corp., Piscataway, NJ) and collected the CD14-enriched fraction after binding to MACS human CD14– specific magnetic beads (Miltenyi Biotec). We differentiated the monocytes to macrophages using human colony-stimulating factor-1 (CSF-1, 20 ng/ml, PeproTech, Rocky Hill, NJ) for 5 d in RPMI 1640 supplemented with antibiotics and 10% CSF. When we used THP-1 cells, we grew them at circa 200 $\times$ 10^3 cells per well in RPMI 1640 medium supplemented with 10% CSF and antibiotics. To promote differentiation, we treated THP-1 monocytes with 100 nM 12-0-tetradeca-noyl-phorbol 13-acetate for 24 h. ^{14}C-2-deoxy-2-carbon-D-glucose (^{14}C-CDG) was obtained from PerkinElmer. For the first set of experiments, we maintained volunteer-derived macrophages under normoxia or for 18 h under hypoxia (1% O_2) and then replaced the medium with fresh medium containing 1 µCi/ml ^{14}C-CDG (^{14}C-CDG, 250 µCi/mmol), 0.5 mM glucose and 0.2 mM unlabeled FDG or FDM. We then determined the ^{14}C-CDG incorporation time course after lysis of the cells by quantification of the radioactivity. In the second set, we incubated THP-1 cells with LDL (100 µg/ml) or LDLox (50 µg/ml) overnight and treated them as in the first set for 7 min. Next, we lysed the cells and determined uptake. In the third set, we incubated THP-1 cells with 1 mM glucose, 0.2 mM FDG or 0.2 mM FDM in RPMI 1640 medium lacking glucose and phenol red and measured lactate release using a commercial kit. In the fourth set, we prepared cell extracts from normoxic or hypoxic volunteer-derived macrophages, filtered these through Sepharose G-25 columns to deplete endogenous metabolites and assayed the total HK activity in the presence of 1 mM adenosine triphosphate (ATP) and FDM or FDG (0.2 mM) and FDM-6-phosphate (FDM6P) or FDG-6-phosphate (FDG6P) at 0.1 mM. In the fifth set, we used the same protocol to assay the HK activity in extracts from volunteer-derived macrophages. In the sixth set, we evaluated the binding of a PE-labeled antibody against MR (Beckman Coulter, PN IM2741) to the MR of the THP-1 cells incubated with unlabeled FDG, unlabeled FDM, mannan, and both unlabeled FDM and mannan for 30 min at the previously described concentrations. Mannan was used at 10 µg/ml.

Production of ^{18}F-FDM.

We produced ^{18}F-FDM using a relatively straightforward three-step protocol (Figure 1a). In the first step, we let β-D-mannopyranose-1,3,4,6-tetra-O-acetate-O-trifluoromethanesulfonate (mannose triflate) react with silver tosylate in acetonitrile under refluxing conditions for 24 h. Thereafter, we removed the solvent. We then took up the residue in dichloromethane and washed it with water. Thereafter, we let the dichloromethane layer dry over magnesium sulfate and purified it. Then, we isolated the product, β-D-glucopyranose 1,3,4,6-tetra-O-acetate-O-toluenesulfonate (glucose tosylate) by preparative thin-layer chromatography plate and characterized it by nuclear magnetic resonance and mass spectra ([M+H]$^+$=503).

In the second step, a chemistry processing computer unit (CPCU) was used. We passed ^{18}F in H$_2$^{18}O from an MC-17 cyclotron through a QMA-light Sep-Pak (Waters Corp.), preconditioned with 3 ml of K$_2$CO$_3$,

140 mg/ml, followed by 3 ml of anhydrous acetonitrile. We then eluted the ^{18}F trapped in the QMA-light Sep-Pak (using nitrogen gas) with 24 ml of acetonitrile and 1 ml of water containing 360 mg of Kryptofix222 (4,7,13,16,21,24-hexaoxa-1,10-diazabicyclo[8.8.8]-hexacosane) and 75 mg of K_2CO_3 and transferred it to the CPCU reaction vessel. Then we dried the ^{18}F, Kryptofix and K_2CO_3 mixture at 120 °C for 10 min. Subsequently, we added acetonitrile (1 mL) and evaporated it at 120 °C for 7 min to ensure dryness of the ^{18}F mixture. Next, we added the precursor, glucosetosylate (2 mg in 0.5 ml of anhydrous acetonitrile), and let it react for 30 min at 96 °C. Subsequent to the reaction, we added 5 mL methanol to the mixture, after which we passed the methanol contents through a neutral alumina Sep-Pak prewashed with methanol (in order to remove any unreacted ^{18}F). The collected methanol solution from the CPCU contained ^{18}F-FDM tetraacetate.

In the third step, we evaporated the methanol solvent in the ^{18}F-2-fluoro-D-mannopyranose-1,3,4,6-tetra-O-acetate solution and took the residue in 1 N hydrochloric acid (1 ml). After heating the resulting solution at 125 °C for 15 min, we let it cool and passed it through AG 11 A8 BioRad 50–100 mesh resin and C-18 Sep-Pak. Then we added sterile 0.9% saline (USP, Abbot Laboratories) to the resulting solution as needed, and filtered it through a 0.2-micron Millex-FG Millipore sterile filter (Millipore). After thin-layer chromatography demonstrated radiochemical purity of ^{18}F-FDM of over 95%, we used this solution for PET imaging studies (Figure 1c). The final radiochemical yields of ^{18}F-FDM were very low, < 5–10%. More efficient methods are currently being developed (181).
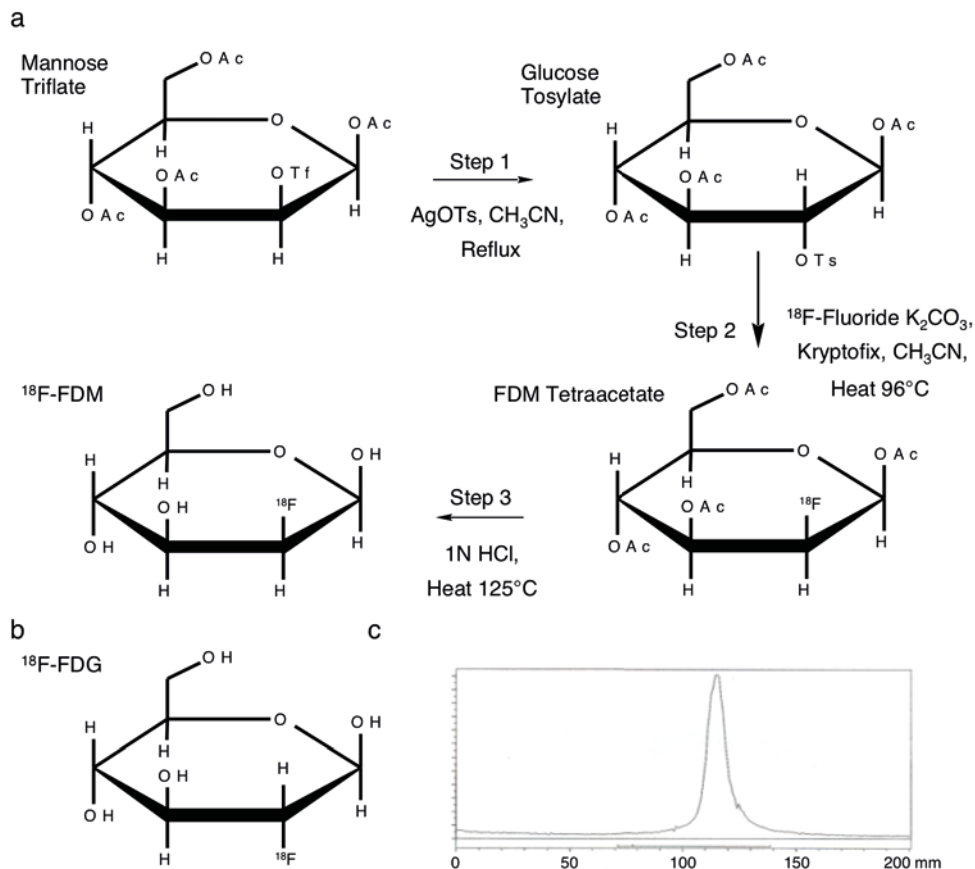
Figure 1. Radiotracer preparation. (a) Schematic representation of the synthesis of ^{18}F-2-deoxy-2- fluoro-D-mannose (^{18}F-FDM). (b) Chemical formula of ^{18}F-2-deoxy-2-fluoro-D-glucose (^{18}F-FDG). (c) thin-layer chromatography demonstrated radiochemical purity of ^{18}F-FDM of over 95%. ^{18}F-FDM = ^{18}F-2-fluoro-2-deoxy-D-mannose; ^{18}F-FDG = ^{18}F-2-fluoro-2-deoxy-D-glucose.

Induction of atherosclerosis in rabbits

New Zealand White (NZW) rabbits (Western Oregon Breeding Laboratories) weighing $3.0 - 3.6$ kg were used. Before imaging experiments, they were kept on a high-fat, high-cholesterol diet that contained 0.5% cholesterol and 6% peanut oil. One week after start of diet, a trained professional performed balloon de-endothelialization of the abdominal aorta (46,51). Animals were anesthetized with a mixture of ketamine and xylazine (100 mg/ml, 10:1 vol/vol; 2.0 to 3.0 ml subcutaneously). Next, a 4F Fogarty embolectomy catheter (12-040-4F, Edwards Lifesciences) was inserted via an arteriotomy site and advanced 20 cm proximally, approximately up to the level of the diaphragm. The catheter was inflated with 0.75 mL of saline and dragged antegrade to the bifurcation of aorta for endothelial denudation; five such passes were made. After removing the catheter, the femoral artery was ligated and the incision site was closed. After recovering form anesthesia, the rabbits were returned to their cages. All rabbit experiments followed the guidelines for the Care and Use of Laboratory Animals established by the US

National Institutes of Health and were approved by the Institutional Laboratory Animal Care and Use Committee at the University of California, Irvine.

In vivo and ex vivo ^{18}F-FDM imaging

We fasted the rabbits for 12 h before the scan. We anesthethized rabbits using isoflurane (3–4% induction, 2–3% maintenance), administered either ^{18}F-FDG (1.75 ± 0.78 mCi IV) or ^{18}F-FDM (1.48 ± 0.64 mCi IV) and then placed the rabbit on the bed of the Inveon microPET scanner (Siemens Medical Solutions) in the supine position. Emission data were acquired dynamically in list mode for 2.5 h.

We killed rabbits with an overdose of sodium pentobarbital (120 mg per kg body weight). Thereafter, we harvested the aortas for ex vivo imaging. As the aortas were longer than the field of view, we cut them in half and performed the ex vivo scan with the halves alongside each other. Thereafter, we segmented aortas at 1-cm intervals and determined radiotracer uptake (%ID/g) in aortic tissue by γ-counting. For comparison of normal versus atherosclerotic regions of each animal, we compared aorta specimens with lowest radiotracer uptake versus specimens from the region of balloon denudation with maximal radiotracer uptake. Also, we determined %ID/g tissue uptake in samples of various organs and in blood samples taken at 1 and 45 min and at 2, 3 and 4 h. To correct for radioactive decay, we set aside aliquots of the injected dose and counted them simultaneously with tissue and blood samples.

We rebinned the list-mode PET data using a Fourier rebinning algorithm and reconstructed the PET data using two-dimensional filter back projection with a Hanning filter with a frequency cutoff at 0.5 Nyquist and corrected for attenuation using [57]Co attenuation scan data. We performed three-dimensional multiplanar reconstruction of raw CT images. We evaluated the PET images on a workstation using ASI Pro VM Micro PET Analysis software (Concorde Microsystems, Knoxville, TN). We measured the SUV score with a standardized two-dimensional circular region of interest on contiguous image projections obtained at 120 − 150 min after injection. We placed a region of interest on the transaxial image to totally surround the most intense area of the tracer uptake and calculated the SUV value by using the maximum and minimum pixel activity value within the region of interest. We corrected SUV values for body weight and injected tracer dose. For quantification of radiotracer uptake in tissue samples, we used a well-type gamma counter (PerkinElmer Wallac).

(immuno)histopathological evaluation of rabbit aorta.

After γ-counting, we fixed one-half (5 mm) of each aorta specimen in 4% paraformaldehyde in phosphate-buffered saline (PBS, pH 7.4, at 4 °C overnight) and stored the fixed tissue in PBS with 0.02% sodium azide (NaN$_3$) at 4°C until use. For histopathological characterization, we used tissue specimens from 5 animals imaged with ^{18}F-FDM, 7 animals imaged with ^{18}F-FDG and 3 control animals imaged with ^{18}F-FDM. From each animal, we took two 5-mm aorta specimens from each uptake tertile for histopathological characterization. We dehydrated specimens using a graded series of ethanol, embedded them in paraffin and cut at 4-μm intervals. Of each 5-mm specimen, adjacent slices were stained with Movat's pentachrome for morphological characterization and with primary antibodies against α-SMA and RAM-11 to detect smooth muscle cells and macrophages, respectively. For antibody-based stainings, we deparaffinized sections and incubated them in antigen-unmasking solution (Vector

Labs) for 25 min in a water bath at 90°C for antigen retrieval. We treated the sections in 3% H_2O_2 and 2% immunoglobulin G–free, protease-free bovine serum albumin (001-000-161, Jackson) with 0.1% Triton X-100 in PBS. We incubated sections with primary antibody against α-actin isotypes (MAB1420, 1:10,000, R&D Systems) to detect smooth muscle cells and RAM-11 (M 0633, 1:3,000, DAKO, Carpinteria, California) to detect macrophages. We then incubated sections with biotinylated secondary antibody (1:200, PK-6100,Vector Labs). For a color reaction, we incubated the sections with diaminobenzidine and counterstained the sections with Gill's hematoxylin. We used sections incubated in parallel without primary antibody for quality control of the staining procedure. For evaluation of stained secions, we took photomicrographs on a Carl Zeiss Axiovert-200 microscope with a 10× objective lens using a Carl Zeiss Axiocam high-resolution digital color camera and Axiovision 3.1 software at 1,300 × 1,300 pixels. We obtained digital images using the same settings, and the segmentation parameters were constant within a range for a given marker and experiment. Images were analyzed using Image-Pro Plus version 5.0. For both markers, we determined the percentage of immunopositive area (immunopositive area/ total intimal area × 100) (Image-Pro) and calculated the correlation with radiotracer uptake.

Autoradiographic evaluation of rabbit aorta

After ^{18}F-FDM imaging and γ-counting, we defolded one-half of each 1-cm specimen aorta tissue of an atherosclerotic animal (the other half of each specimen of this animal we used for histopathological characterization). We laid these specimens flat on a Phosphor Cyclone Imager (Packard Instruments) for 24 h. We analyzed the generated autoradiographs using a computer-based image analysis system (OptiQuant Version 4.0, Packard Instruments), and we expressed uptake as digital light units (DLU) /mm.

Statistical analysis.

We presented all values as mean ± SD We compared groups using independent Student's t-test. For multiple group comparisons, we employed one-way analysis of variance with post hoc Student-Newman-Keuls test for pairwise comparison. For correlations, we calculated Pearson correlation coefficients. We considered $P < 0.05$ as statistically significant. We calculated the biological half-life of both radiotracers using nonlinear regression analysis using a least-squares weighted simplex algorithm, with data weighted with the reciprocal of the observed value.

Results

Presence of MR-bearing macrophages in high-risk plaques

To confirm that MRs are upregulated in unstable atherosclerotic plaques in humans, we stained frozen coronary sections after sudden cardiac death from subjects enrolled in the Cardiovascular Pathology Institute Sudden Coronary Death Registry; we compared five stable and five unstable (including thin-cap fibroatheromas or TCFA) coronary artery atherosclerotic plaques (Figure 2). We employed modified Movat's pentachrome staining for morphologic characterization CD68 staining revealed modest macrophage infiltration in the stable plaques, mostly around the lipid core. In the TCFAs, macrophage

infiltration was more extensive and occurred in the entire necrotic core and thin fibrous cap. CD163 and CD206 staining revealed very few M2 and almost no MR-bearing macrophages in the stable plaque, respectively. On the other hand, infiltration of both M2 and MR-bearing subpopulations was intense in the TCFAs, mostly in the fibrous cap. The quantitative evaluation of macrophage-rich areas in TCFAs and stable plaques revealed significantly higher area density (positively stained percentage of evaluated area) of M2 (6 ± 4 versus 0.6 ± 0.9, $P < 0.05$) and MR-bearing macrophages (3 ± 2 versus 0.1 ± 0.1, $P < 0.05$) in these regions in TCFAs than in stable plaques.
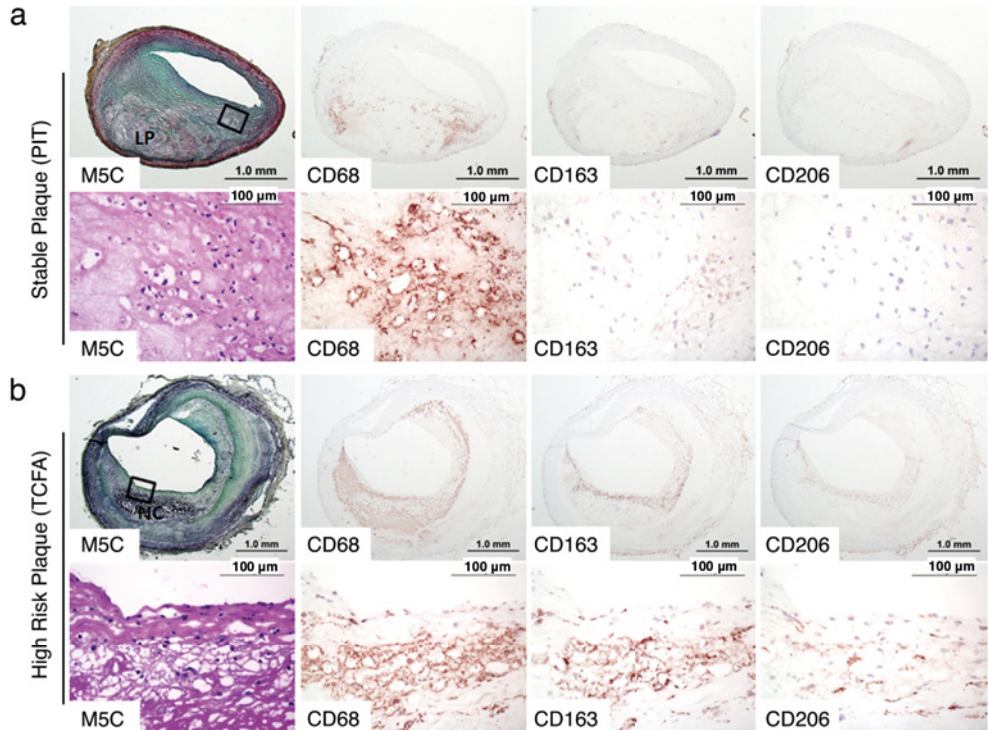
Figure 2: Mannose receptor-bearing macrophages in human stable and high-risk atherosclerotic plaques. (a) Top, photomicrographs of adjacent sections of stable coronary atherosclerotic plaque stained with M5C (plaque morphology) or for CD68 (macrophages), CD163 (M2 macrophages) or CD206 (MR-bearing macrohages). Bottom, high-power views of the plaque shoulder region corresponding to the black box in the top left photomicrograph. (b) Top, photomicrographs of adjacent sections of a high-risk coronary atherosclerotic plaque (TCFA) stained with M5C, CD68, CD163 or CD206 (MR). Bottom, high-power views at the border between the NC and the fibrous cap corresponding to the black box in the top left photomicrograph. LP = lipid pool; M5C = Movat's Pentachrome, NC = necrotic core; PIT = pathologic intimal thickening; TCFA = thin-cap fibroatheromas

FDM and FDG uptake by cultured macrophages

To evaluate the FDG and FDM uptake in macrophages, we performed cell culture studies using macrophages derived from CD14+ cells isolated from human volunteers and THP-1 monocytes. These studies suggest substantially higher uptake of FDM as compared to FDG in macrophages. In the first set of experiments, we evaluated the effects of co-incubation with unlabeled FDM and FDG on 14C-CDG

accumulation (Figure 3a). In normoxic conditions, co-incubation with FDG significantly reduced ^{14}C-CDG uptake, whereas co-incubation with FDM resulted in a statistically nonsignificant reduction at all time points before 15 min; ^{14}C-CDG accumulation was approximately 40% higher in cells incubated with FDM compared to those incubated with FDG. In hypoxic conditions, ^{14}C-CDG uptake was higher than in normoxic conditions; the accumulation was approximately 50% higher in cells incubated with FDM compared to those incubated with FDG.

In the second set of experiments, in the presence of low-density lipoprotein (LDL) and oxidized LDL (LDLox), ^{14}C-CDG uptake was higher, and the inhibitive effect of FDM remained smaller than that of FDG; in cells incubated with FDM, when compared to cells incubated with FDG, ^{14}C-CDG accumulation was approximately 90% higher in normal conditions, approximately 35% higher in the presence of LDL and approximately 55% higher in the presence of LDLox (Figure 3b).

In the third set of experiments with lactate as the readout of glucose metabolism, cells incubated with FDM showed approximately 35% higher lactate production than cells incubated with FDG (Figure 3c).

In the fourth set, we measured the HK activity in extracts from macrophages maintained under hypoxic and normoxic conditions and assayed in the presence of FDM and FDG or their phosphorylated end products FDM-6-phosphate (FDM6P) and FDG-6-phosphate (FDG6P). There was significantly lower inhibition of HK activity by FDM compared to FDG and by FDM6P when compared to FDG6P. In the normoxic and hypoxic conditions, HK activity was approximately 20% higher in presence of FDM than in the presence of FDG. In normoxic and hypoxic conditions, HK activity was approximately 60% higher in presence of FDM6P than in the presence of FDG6P (Figure 3d).

As mannose and glucose are isomers (Figure 1b) that enter the cell through the glucose transporter, we had expected that the inhibitory effect of FDM on ^{14}C-CDG uptake would be similar to that of FDG in these competition studies or, in other words, that ^{18}F-FDG and ^{18}F-FDM uptake in macrophages would be identical. However, the lower inhibitory effect of FDM on sugar incorporation, which was also confirmed by higher lactate production, was explained by lower inhibition of HK activity. This suggested relatively more efficient metabolism of FDM to downstream metabolites, resulting in lower inhibition of HK activity, which allows uninhibited entry of six-carbon sugars into the cell.

This became more evident after the fifth set of experiments, where we incubated macrophage extracts with FDM6P and FDG6P. We observed a time-dependent decrease in the inhibition of HK by FDM6P, whereas FDG6P-based inhibition remained constant (Figure 3e). As HK activity is the force driving cellular FDG and FDM uptake, the lower HK inhibition by FDM supports a higher ^{18}F-FDM uptake when compared to ^{18}F-FDG uptake. Based on the experiments described above that consistently favor FDM (versus FDG) transport (by 35 − 90%, depending on the conditions), we estimate at least 35% higher ^{18}F-FDM uptake by macrophages, if all ^{18}F-containing ^{18}F-FDM metabolites remain intracellular.

In addition to metabolic uptake of FDM, we also evaluated FDM accumulation through MRs on macrophages in the sixth set of experiments. By titrating the binding of an antibody specific for the MR (CD206), we evaluated the relative interaction with MR by FDG, FDM and mannan, a mannose polymer known to bind the MR (Figure 3f). FDM and mannan both reduced antibody binding by approximately 35%. Mannan and FDM together reduced the antibody binding even further, by approximately 60%. This demonstrates that FDM binds to the MR. On the other hand, as expected, FDG did not reduce

binding of the anti-MR antibody and thus does not bind the receptor (Figure 3f). Specific binding of 18F-FDM to the MR may provide another clinically relevant avenue for 18F-FDM uptake in high-risk atherosclerotic plaques.
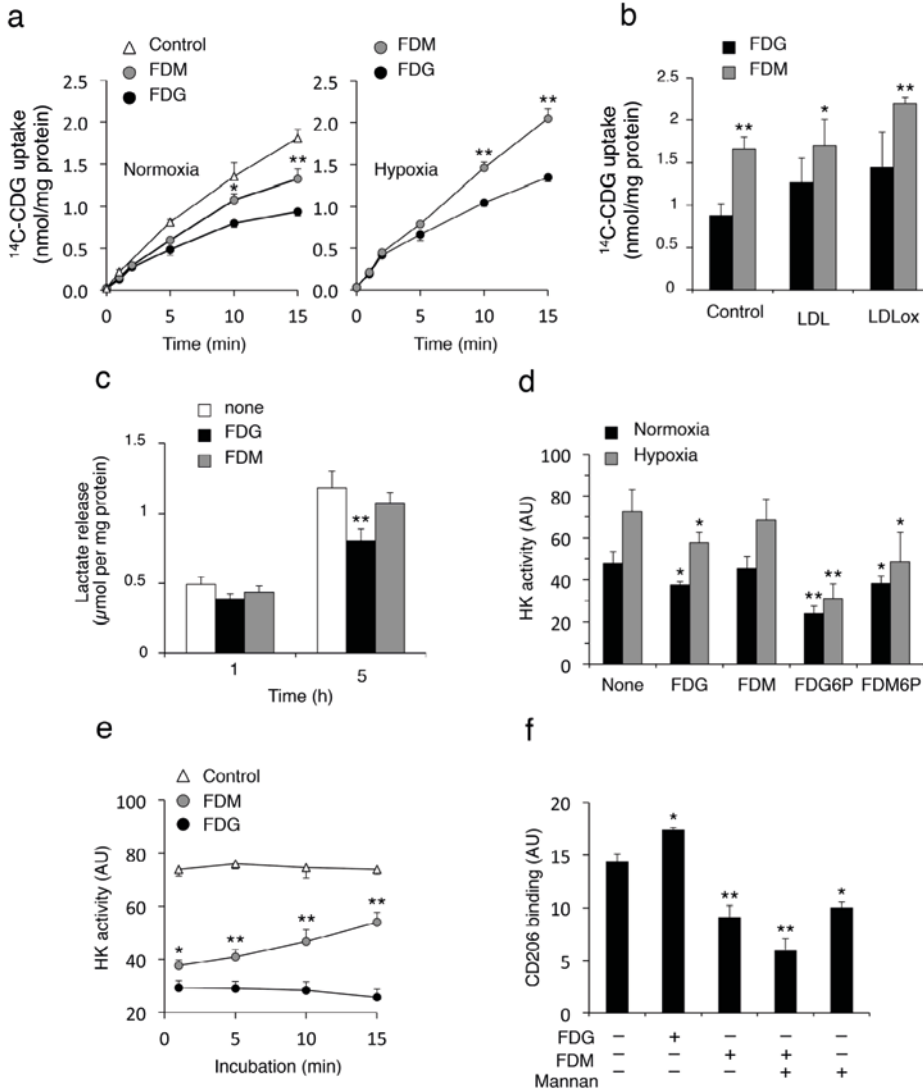
Figure 3: Characterization of FDM and FDG uptake by cultured macrophages. (a) Effect of unlabeled FDM versus unlabeled FDG on ^{14}C-CDG accumulation in volunteer-derived macrophages maintained under normoxia or hypoxia. (b) Effect of non-radioactive 2-deoxy-2-fluoro-D-mannose versus non-radioactive 2-deoxy-2-fluoro-D-glucose on ^{14}C-CDG uptake in THP-1 macrophages maintained with human LDL or LDLox. (c) Effect of co-incubation with FDM versus on lactate release from THP-1 macrophages. (d) Effect of versus FDG and FDM6P versus FDG6P on HK activity of volunteer-derived macrophages in hypoxic and normoxic conditions. (e) Inhibitory effect of FDM6P versus FDG6P on HK activity of volunteer-derived macrophages over time. (f) Effect of co-incubation with FDG, FDM, mannan and FDM + mannan on binding of anti-CD206 antibody to CD206 (MR) on THP-1 macrophages.Data presented are means ± SD of at least 3 experiments. * = P < 0.05, ** = P < 0.01; ^{14}C-CDG = ^{14}C-2-deoxy-2-carbon-D-glucose; AU = arbitrary units; FDG = 2-fluoro-2-deoxy-D-glucose, FDM = 2-fluoro-2-deoxy-D-mannose ; FDG6P = FDG-6-phosphate; FDM6P = FDM-6-phosphate.

^{18}F-FDM imaging, quantification, autoradiography and pharmacokinetics

We produced ^{18}F-FDM using a radiolabeling protocol similar to that used for ^{18}F-FDG (Figure 1a); thin-layer chromatography confirmed radiochemical purity of over 95% (Figure 1c). We evaluated the feasibility of PET imaging with ^{18}F-FDM in a rabbit model of atherosclerosis (Figure 4) produced by high-cholesterol diet and subdiaphragmatic aorta denudation (n = 8); unmanipulated animals were used as disease controls (n = 3). We performed ^{18}F-FDG PET imaging to provide the positive-control group in separate sets of atherosclerotic (n = 8) and control (n = 3) animals for comparison with ^{18}F-FDM. Blood-pool images obtained 0 − 10 min after intravenous injection showed the aorta similarly in both atherosclerotic and control animals (Figure 4a). Atherosclerotic lesions were best visualized by ^{18}F-FDM at 120 − 150 min after the radiotracer injection. By this time, the blood activity had subsided, and we observed marked radiotracer uptake in the aortas of atherosclerotic animals (Figure 4a) and only scant uptake in the control animals. SUV evaluation revealed significantly higher uptake in atherosclerotic abdominal aortas when compared to relatively normal thoracic aortic aortas (1.69 ± 0.26 versus 0.35 ± 0.21, P < 0.05) (Figure 4b).

After *in vivo* imaging and euthanasia, we obtained *ex vivo* PET images of aortas. These paralleled *in vivo* images, as the aortas of atherosclerotic animals revealed intense ^{18}F-FDM uptake; we observed maximum uptake in the abdominal parts and aortic arches corresponding to the gross distribution of atherosclerotic lesions (Figure 4c). No atherosclerotic plaques or specific radiotracer accumulation was present in aortas of control animals.

After *ex vivo* imaging, we cut aortas at 1-cm intervals and quantified radiotracer uptake by γ-counting, which confirmed the imaging data (Figure 4d). ^{18}F-FDM uptake (%ID/g) in atherosclerotic regions was higher than in relatively normal regions (0.04 ± 0.01 versus 0.018 ± 0.006, P < 0.05) and higher than the maximum detected in the control animals (0.016 ± 0.003, P < 0.05).

After γ-counting, we further characterized ^{18}F-FDM uptake in the aorta of one animal by autoradiography. Autoradiographic uptake was higher in regions with grossly visible atherosclerotic plaque than in normal areas (Figure 4e), and quantitative analysis revealed maximal ^{18}F-FDM uptake to be almost 100-fold higher than minimal uptake (Figure 4f).
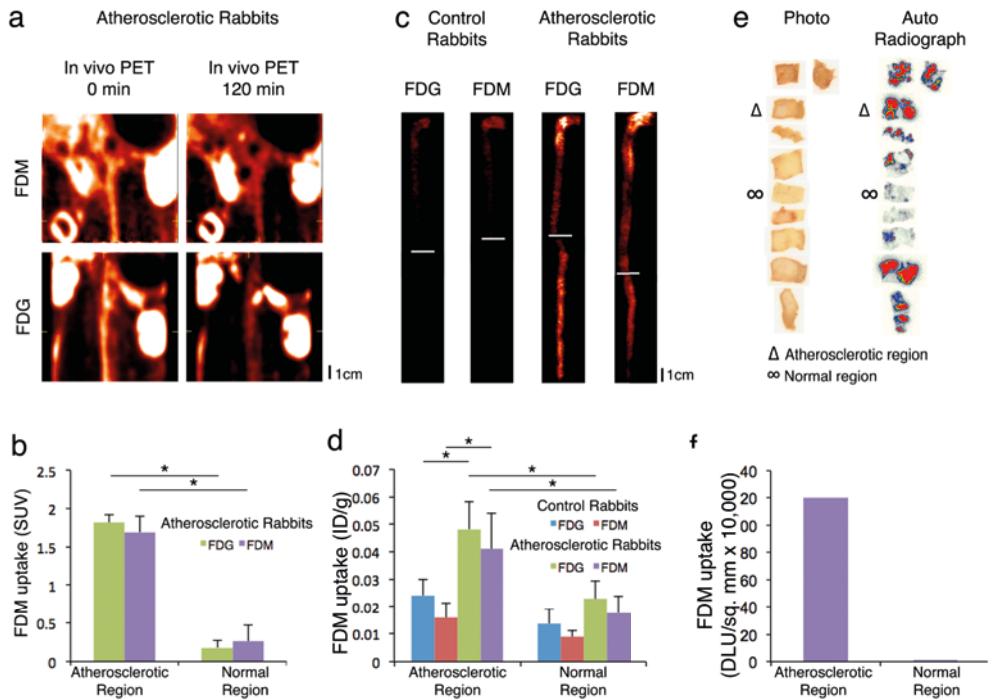
Figure 4: *In vivo* and *ex vivo* radionuclide imaging and uptake quantification in atherosclerotic rabbit aorta. (a) Representative coronal views of *in vivo* ^{18}F-FDM PET imaging (n = 8, top) and ^{18}F-FDG PET imaging (n = 8, bottom) in atherosclerotic animals. Early (blood-pool) acquired at 0 – 10 min after radiotracer administration (left) and late images acquired at 120 – 150 min (right) show uptake of both radiotracers in the arterial wall. (b) SUV analysis of *in vivo* ^{18}F-FDM (n = 4) and ^{18}F-FDG PET (n = 3) images of atherosclerotic rabbits. (c) Representative examples of *ex vivo* ^{18}F-FDM and ^{18}F-FDG PET imaging in atherosclerotic (n = 8 for each tracer) and control animals (n = 3 for each tracer). Before imaging, aortas were cut in half; halves were imaged alongside each other. White lines indicate the point of division. (d) γ-counting results of ^{18}F-FDM and ^{18}F-FDG uptake in atherosclerotic and relatively normal aorta regions of atherosclerotic and control animals. (e) Photo and ^{18}F-FDM autoradiography images of 0.5-cm aorta specimens from an atherosclerotic rabbit. (f) Results of quantification of autoradiography image (expressed as DLU/mm); comparison of uptake in atherosclerotic versus relatively normal region. * = P < 0.05. SUV = standardized uptake value.

Biodistribution and pharmacokinetic studies revealed maximum radiation burden to the kidneys (Figure 5a), a low burden in all other organs and a median circulating tracer half-life of 74 min (Figure 5b).
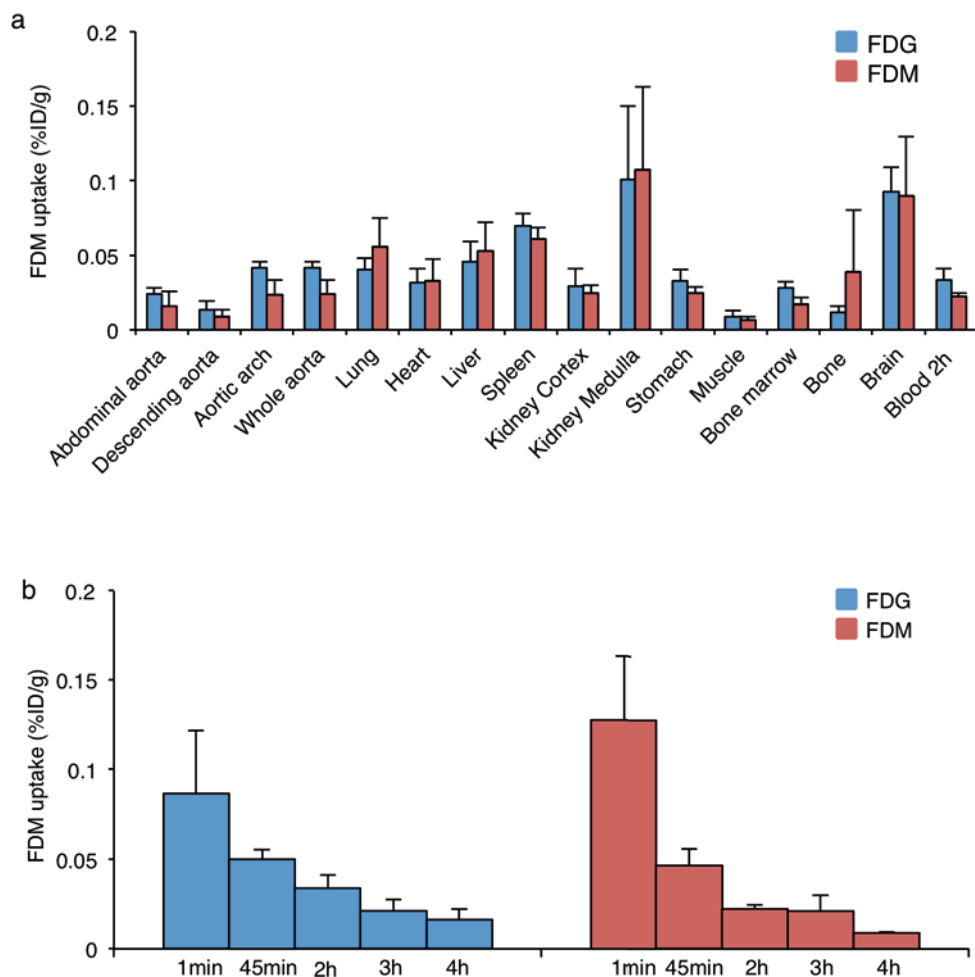
Figure 5. Pharmacokinetic studies. (a) Biodistribution of ^{18}F-FDG and ^{18}F-FDM. (b) Blood clearance studies of ^{18}F-FDM and ^{18}F-FDG.

^{18}F-FDM uptake: autoradiography and (immuno)histopathology

After γ-counting, we histopathologically characterized aorta specimens with high, moderate and low uptake (Figure 6). ^{18}F-FDM uptake was highest in specimens with morphologically inflamed and lipid-rich plaques (as shown by modified Movat's pentachrome staining) and correlated with the extent of macrophage infiltration (as shown by RAM-11 staining) (r = 0.45, P < 0.01) but not with the abundance of smooth muscle cells (as shown by staining for α-smooth muscle actin, α-SMA).
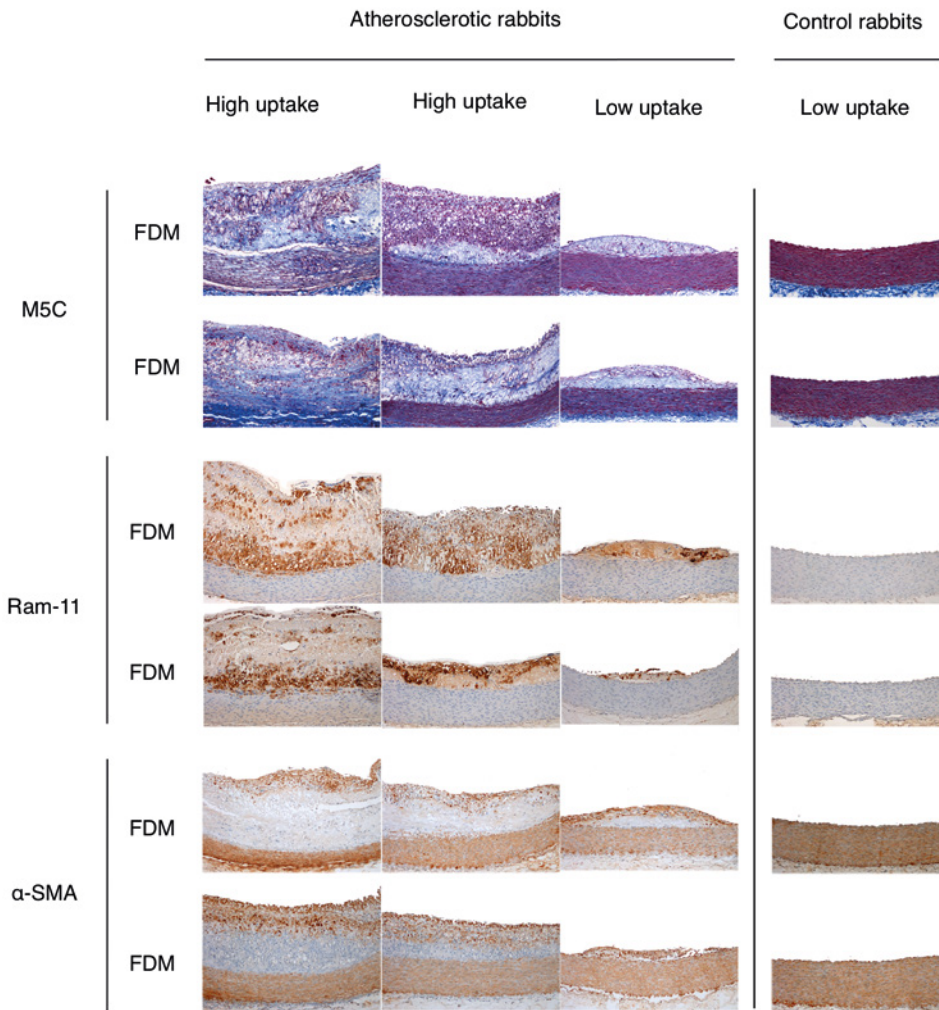
Figure 6: Histopathological characterization of ^{18}F-FDM uptake in atherosclerotic rabbit aorta. Representative photomicrographs of aortic tissue sections from atherosclerotic animals with high (column 1), moderate (column 2) and low (column 3) ^{18}F-FDM or ^{18}F-FDG uptake and aortic tissue sections from control animals after imaging with ^{18}F-FDG or ^{18}F-FDM (column 4) are shown. Rows show results of M5C staining (top), RAM-11 staining for macrophages (middle) and α-sma for smooth muscle cells (bottom). We used specimens from 7 animals imaged with ^{18}F-FDG, 5 animals imaged with ^{18}F-FDM and 2 control rabbits for histopathological analysis. From each animal, we selected 2 specimens in each uptake tertile. We stained adjacent sections from all selected specimens with all 3 stains, one section per stain. α-SMA = smooth muscle actin.

Comparison of ^{18}F-FDM and ^{18}F-FDG imaging

To evaluate whether ^{18}F-FDM imaging was non-inferior to ^{18}F-FDG imaging, we performed ^{18}F-FDG imaging in additional sets of atherosclerotic (n = 8) and control (n = 3) rabbits. Blood pool ^{18}F-FDM and ^{18}F-FDG images obtained from 0 − 10 min after IV injection show the aorta. *In vivo* ^{18}F-FDM and ^{18}F-FDG images obtained from 120 − 150 min after injection showed comparably high specific uptake of

both tracers in the abdominal aortas and aortic arches of atherosclerotic animals (Figure 4a); this was confirmed by *ex vivo* imaging. *In vivo* and *ex vivo* ^{18}F-FDM and ^{18}F-FDG images showed comparably high specific uptake of both tracers in the abdominal aortas and aortic arches of atherosclerotic animals (Figure 4c). No specific uptake of either radiotracer was observed in aortas of the control animals (Figure 4). SUV evaluation of ^{18}F-FDM (n = 4) and ^{18}F-FDG (n = 3) imaging in atherosclerotic animals revealed similar uptake in atherosclerotic (1.69 ± 0.26 versus 1.82 ± 0.17, NS, and also in non-atherosclerotic (0.35 ± 0.21 versus 0.33 ± 0.12, NS) regions (Figure 4b). γ-counting confirmed that ^{18}F-FDM and ^{18}F-FDG uptake (expressed as %ID/g) were similar in atherosclerotic (atherosclerotic region, 0.042 ± 0.01 versus 0.048 ± 0.01, NS; non-atherosclerotic regions, 0.018 ± 0.005 versus 0.023 ± 0.003, NS) and control animals (maximal uptake, 0.016 ± 0.005 versus 0.024 ± 0.005, NS; minimal uptake, 0.009 ± 0.003 versus 0.014 ± 0.005, NS) (Figure 4d).

The relationships between uptake of ^{18}F-FDM and ^{18}F-FDG and their respective histopathological plaque characteristics were also comparable (Figure 6). Both tracers showed a direct correlation with the extent of macrophage infiltration (^{18}F-FDM, r = 0.45, P < 0.05 and ^{18}F-FDG, r = 0.57, P = 0.0001). Also, ^{18}F-FDM and ^{18}F-FDG had similar biodistribution (Figure 5a) and circulating half-life data (74 min versus 115 min, NS, Mann-Whitney test) (Figure 5b).

Discussion

Although ^{18}F-FDG has been extensively employed for the detection of plaque inflammation, we evaluated the feasibility of ^{18}F-FDM imaging in the present study. The use of ^{18}F-FDM was based on the premise that mannose, being an isomer of glucose, should be similarly taken up by macrophages and that expression of MRs by a subset macrophages should provide an additional target for macrophage imaging. We observed increased expression of MR-bearing M2 macrophages in unstable plaques and specific binding of FDM to the MR receptor. We propose that the overexpression of MRs in high-risk plaques could provide an additional avenue for ^{18}F-FDM uptake. Furthermore, although determining the superiority of metabolic uptake of ^{18}F-FDM was not one of our study objectives, the in vitro macrophage studies indicated at least 35% higher FDM uptake when compared to that of FDG, based on lower inhibition of HK activity.

This study reports the feasibility of imaging of atherosclerotic lesions with ^{18}F-FDM, radiolabeled mannose, and demonstrates that ^{18}F-FDM uptake is non-inferior to ^{18}F-FDG uptake. Because cell studies in human macrophages indicated higher metabolic FDM uptake and MRs are upregulated in high-risk plaques in humans, we believe clinical ^{18}F-FDM imaging would demonstrate superior imaging characteristics. To confirm this, clinical studies are required.

Chapter 3

Minocycline inhibits cell death in mouse and rabbit models of acute myocardial infarction: evaluation with ^{99m}Tc-annexin A5 imaging

Hans J. de Haas[1,2], Reza Golestani[1], Riemer Slart[1], Artiom D. Petrov[2], Nicole Bitsch[3], Y. Chandrashekhar[4], Masayoshi Sarai[5], Chao Wu[1], Leo M. Stolk[6], Robert H. Henning[7], Clark J. Zeebregts[8], Rene A. Tio[9], Jos G. W. Kosterink[7], Rudi A.J.O. Dierckx[1], Chris P.M. Reutelingsperger[10], Hendrikus H. Boersma[1, 7], Jagat Narula[2]

1.   Department of Nuclear Medicine and Molecular Imaging, University of Groningen, University Medical Center Groningen, Groningen, the Netherlands
2.   Zena and Michael A. Wiener Cardiovascular Institute, Mount Sinai School of Medicine, New York
3.   Department of Cardiology, Maastricht University Medical Center, Maastricht, the Netherlands
4.   Division of Cardiology, VA Medical Center and University of Minnesota, Minneapolis, Minnesota
5.   Division of Cardiology, Fujita Health University School of Medicine, Toyoake, Japan.
6.   Department of Clinical Pharmacy and Toxicology, Maastricht University Medical Center, Maastricht, the Netherlands
7.   Department of Clinical Pharmacy and Pharmacology, University of Groningen, University Medical Center Groningen, Groningen, the Netherlands
8.   Division of Vascular Surgery, Department of Surgery, University Medical Center Groningen, Groningen, the Netherlands
9.   Department of Cardiology, University of Groningen, University Medical Center Groningen, Groningen, the Netherlands
10.   Department of Biochemistry, Cardiovascular Research Institute, University of Maastricht, Maastricht, The Netherlands.

Abstract

Background: studies in animal models of acute myocardial infarction have shown cardioprotection by minocycline. In these studies, minocycline was administered before ischemia, which in clinical practice is rarely possible. This study aims to determine whether minocycline, when administered at reperfusion, reduces cardiac damage.

Methods. To simulate acute myocardial infarction, myocardial ischemia and reperfusion were induced in mice (n = 13) and rabbits (n = 8), subgroups were randomized to receive minocycline treatment upon reperfusion, or to remain untreated. Cell death was evaluated in all rabbits by planar ^{99m}Tc-annexin A5 imaging of explanted heart followed by gamma counting and in mice by absolutely quantified ^{99m}Tc-annexin A5 SPECT imaging and terminal deoxynucleotidyl transferase dUTP nick end labeling (TUNEL) staining.

Results. In mice, *in vivo* SPECT imaging showed lower ^{99m}Tc-annexin A5 uptake (expressed as percent injected dose per gram of tissue, %ID/g) in treated than in control animals (1.31 ± 0.32 versus 2.15 ± 0.52, P < 0.01). TUNEL staining confirmed a reduction of percentage of apoptotic cardiomyocytes in minocycline-treated mice versus controls (0.16 ± 0.10 versus 0.54 ± 0.32, P = 0.034). In rabbits, *ex vivo* planar imaging showed reduced radiotracer uptake in minocycline-treated animals. *Ex vivo* gamma counting showed a trend of reduced radiotracer uptake (%ID/g) in the infarcted apex in minocycline-treated animals versus control animals (0.29 ± 0.14 versus 0.4 ± 0.16, P = 0.332).

Conclusions. The results of this study indicate cardioprotection by minocycline in a clinically translatable protocol.

Introduction

Myocardial ischemia results in myocardial apoptosis and necrosis. Early restoration of perfusion limits myocardial damage. For this reason, mechanical and pharmacological revascularization remains the mainstay of management of acute coronary events. Reperfusion, although highly beneficial on balance, also has detrimental effects. It bathes cells in calcium, triggers a bout of oxidative stress, resulting in substantial cell death, which is further enhanced by an exaggerated inflammatory response (182). This process is called ischemia/reperfusion injury, and constitutes an attractive target for cardioprotective strategies.

Minocycline is a semi-synthetic tetracycline antibiotic with anti-apoptotic, anti-inflammatory and antioxidant properties. Extensive preclinical data (183) and initial clinical studies (184-187) suggest that minocycline is neuroprotective in setting of cerebro-vascular accident (CVA). Similarly, several pre-clinical studies in animal models of acute myocardial infarction have demonstrated cardioprotective effects of minocycline (188-191). In these studies minocycline was administered before the induction of ischemia. This does not mimic the clinical situation, in which therapy can be administered during or after myocardial ischemia.

[99m]Tc-annexin A5 has been successfully employed as a tracer for identification of cell death by the apoptotic process. Annexin A5 binds to apoptotic cells because it has specific affinity for phosphatidyl serine (PS), which is specifically expressed on the cell surface of apoptotic cells (192). ^{99m}Tc-annexin A5 imaging has been used in animal models and patients with myocardial ischemia to visualize apoptosis (121,125,126). The present study evaluated the efficacy of acute minocycline administration in animal models of acute myocardial infarction. Minocycline was administered at the time of reperfusion to simulate the clinical situation. For evaluation of apoptosis, ^{99m}Tc-annexin A5 imaging was employed.

Materials and Methods

[99m]Tc-labeling protocol of annexin A5

100 µg of human recombinant hynic-annexin A5 (Theseus Imaging Corp, Cambridge MA) was thawed after storage (at -20°C) and mixed with ca. 740 MBq pertechnetate (1 ml). Subsequently, 0.1 ml stannous tricine buffer was added to the vial for pertechnetate reduction. This mixture was allowed to incubate for 30 min at room temperature. The pH was measured (limits pH 5-7) and radiochemical purity (RCP) was assessed by TLC on silica impregnated paper (Gelman Sciences, Ann Arbor, MI) using ACD buffer as the eluent. This method showed that the radiolabeling protocol yielded a radiochemical purity of 91.3 ± 4.3%.

Induction of acute myocardial infarction and minocycline treatment in mice

All mouse experiments were conducted according to the NIH guidelines and were approved by the Institutional Laboratory Animal Care and Use Committees at the University of Groningen. Thirteen C57BL/6 mice were anesthetized with pentobarbital (100 mg/kg IP), intubated and ventilated on room

air (MiniVent HSE-HA, Harvard Apparatus, Holliston, Massachusetts). Subsequently, the mice were placed on a heating bed and body temperature was maintained at 36.5°C during surgery and imaging. After exposure of the heart through left thoracotomy, the left coronary artery was ligated after its main branching point with 6-0 polypropylene suture.

The suture was tied over a 1-mm polyethylene tube. After 30 min of ischemia, reperfusion was instituted through removal of the coronary suture. The occurrence of reperfusion was confirmed by the observation of blood flow in epicardial coronary arteries through the operation microscope. The mice were randomized to either receive a single dose of minocycline (30 mg/kg, I.V. n = 7) immediately after onset of reperfusion or to remain untreated (n = 6). When correcting for the first pass effect, this dosage was consistent with previous studies, in which minocycline dosages of approximately 50 mg/kg/day were administered intraperitoneally (188-191).

Induction of acute myocardial infarction and minocycline treatment in rabbits

All rabbit experiments were conducted according to the NIH guidelines and were approved by the Institutional Laboratory Animal Care and Use Committees at the University of California, Irvine. Eight male New Zealand White Rabbits weighing 3.0 – 3.5 kg were anesthetised with 2.0 – 3.0% isoflurane. Surgical tracheostomy was performed, animals were intubated and mechanically ventilated on room air (MiniVent HSE-HA, Harvard Apparatus, Holliston, Massachusetts). The heart was exposed by parasternal thoracotomy, and the pericardium was removed. The region of the left anterior descending coronary artery was identified between the aortic root and the left auricle, and a monofilament suture was placed to occlude the artery. After 40 min of occlusion, the suture was removed to induce reperfusion. The animals were randomized to either receive a single dose of minocycline (30 mg/kg, IV n = 4) immediately after onset of reperfusion or to remain untreated (n = 4).

***Ex vivo* SPECT imaging of rabbit heart**

After 30 min of reperfusion, ^{99m}Tc-annexin A5 (370 ± 29 MBq, containing 100 µg annexin A5 protein), was administered through the marginal ear vein. At three hours after radiotracer administration, the rabbits were sacrificed using an overdose of sodium pentobarbital (120 mg/kg), hearts were carefully removed and placed in a two-head micro-SPECT gamma (X-SPECT, Gamma Medica, Inc; Northridge, CA). Planar imaging was performed in a 128 ×128 scaffold using a low-energy 1mm pinhole collimator. Thereafter, hearts were cut into 4 equidistant short-axis; slices were photographed and cut into a total of 32 pieces. Each piece was weighed and radiotracer uptake was quantified by γ-counting using an automated well-type gamma scintillation counter (1480 Wizard 3", Wallac Oy Finland). To correct for the radioactive decay and permit calculation of the radioactivity in pieces as percent injected dose per gram of tissue (%ID/g), aliquots of the injected dose were counted simultaneously.

***In vivo* SPECT imaging in mice**

Two min after onset of reperfusion, ^{99m}Tc-annexin A5 (13± 3.5MBq) and ^{201}Tl (10 ± 2.5 MBq) were injected through the penile vein. Thereafter the mice were positioned on a half open cylindrical bed in a small-animal SPECT equipped with a 75-pinhole collimator, three NaI gamma-cameras positioned in a

Minocycline inhibits cell death in mouse and rabbit models
of acute myocardial infarction: evaluation with 99mTc-annexin A5 imaging

3

triangle and three optical cameras (USPECT II, MILabs, the Netherlands)(193). Photographs acquired by the optical cameras were used to define the volume of interest with the heart in the center. SPECT images were acquired for 30 min. Thereafter, the mice were euthanized through cervical dislocation. 99mTc-annexin A5 and 201Tl imaging results were reconstructed separately. Reconstruction of 99mTc-annexin A5 images was performed using a fully 3D pixel-based ordered subset expectation maximization (POSEM) (194) algorithm with six iterations, sixteen subsets and a 0.1875 mm voxel size. A triple-energy-window method was applied for scatter correction during the reconstruction process. The projections of scatter photons within the range of photopeak window (140 keV, 20% width) were estimated by using photons in two background windows (115 keV, 10% width, and 163 keV, 7% width), and were incorporated in the POSEM reconstruction according to the Bowsher method (195). An attenuation map was drawn using optical photographs, which were taken for VOI selection. The attenuation coefficient µ was considered homogeneous within the animal and was set as the value for 140 keV photon travelling in water (0.151/cm).

For reconstruction of 201Tl images, the same protocol was used with a different photopeak window (72 KeV, 27% width) and background windows (56 KeV, 11% width and 94 KeV, 10%) applied. Thereafter, 99mTc-annexin A5 SPECT images were absolutely quantified as described by Wu et al (196). Briefly, voxel values were multiplied by a calibration factor (the known ratio between voxel values and the corresponding activity concentrations). Due to high scatter from 99mTc, the heart region was only visible in the 201Tl images of 3 animals. The best 201Tl image was selected and a region of interest (ROI) was drawn around the heart. The 201Tl image was co-registered with the 99mTc-annexin A5 image of the same mouse and 99mTc-annexin A5 uptake within the ROI was absolutely quantified. The 99mTc-annexin A5 image of this mouse was co-registered with the 99mTc-annexin A5 images of the remaining mice based on liver uptake and myocardial 99mTc-annexin A5 uptake in the ROIs. Next, the %ID/g in the hearts was obtained by dividing the average activity per mL in the ROI by the injected dose, assuming a heart density of 1g/cm^3. For image analysis, Inveon Research Workplace software (Siemens) was used.

Immunohistopathological measurement of cardiac apoptosis in mice

After harvesting, mid-ventricular slices (2 − 3 mm) were cut, fixed for 48 hours in 4% paraformaldehyde at 4°C, and paraffin-embedded. To measure the rate of apoptosis in the specimens, terminal deoxynucleotidyl transferase-mediated deoxyuridine triphosphate nick-end labeling (TUNEL) staining was performed on 4-µm slices using a commercially available kit (In Situ Cell Death Detection Kit, Fluorescein; Roche Diagnostics Nederland B.V, Almere, the Netherlands). The protocol of the manufacturer was followed. After deparaffinization and rehydration, the sections were permeabilized with Proteinase K (20 uL/mL in Tris/HCl, Roche Diagnostics Nederland B.V, Almere, the Netherlands) for 30 min and rinsed with phosphate-buffered saline (PBS) three times. Samples were incubated with TUNEL reaction mixture consisting of nucleotides and TdT for 1 hour at 37°C in the dark. Then, the slides were rinsed with PBS three times. Thereafter, nuclei were counterstained by mounting with medium containing 4,6-diamino-2-phenylindole (DAPI) (Vectashield Mounting Medium with DAPI, Vector Laboratories Ltd. United Kingdom, Peterborough, United Kingdom). Slides were stored in a light tight container at 4°C until analysis. Overview photographs were taken at 20× magnification with an

automatic photomicroscope (TissueFaxs, TissueGnostics GmbH, Vienna, Austria). The number of cells was determined automatically based on DAPI staining by a specialized software program (TissueQuest, TissueGnostics GmbH, Vienna, Austria). Next, the number of TUNEL positive cells was determined by eye by a blinded operator.

Statistical analysis

Unless otherwise indicated, data are expressed as expressed as mean ± standard deviation. For pairwise comparisons, the Student's T-test was used. P values of < 0.05 were considered significant. All statistical analyses were performed using IBM SPSS Statistics (IBM corporation, Chicago, IL).

Results

[99mTc]-annexin A5 imaging in mice and rabbits.

In C57BL/6 mice, apoptosis was visualized by *in vivo* SPECT imaging after administration of ^{99m}Tc-annexin A5. Figure 1 a shows representative examples of ^{99m}Tc-annexin A5 SPECT images of minocycline-treated and untreated animals. Uptake of ^{99m}Tc-annexin A5 is markedly lower in treated animals than in untreated animals. Absolute quantification of the myocardial uptake of ^{99m}Tc-annexin A5 (Figure 1b) revealed lower ^{99m}Tc-annexin A5 uptake (expressed %ID/g) in minocycline-treated animals than in non-treated animals (1.31 ± 0.32 versus 2.15 ± 0.52, P < 0.01).
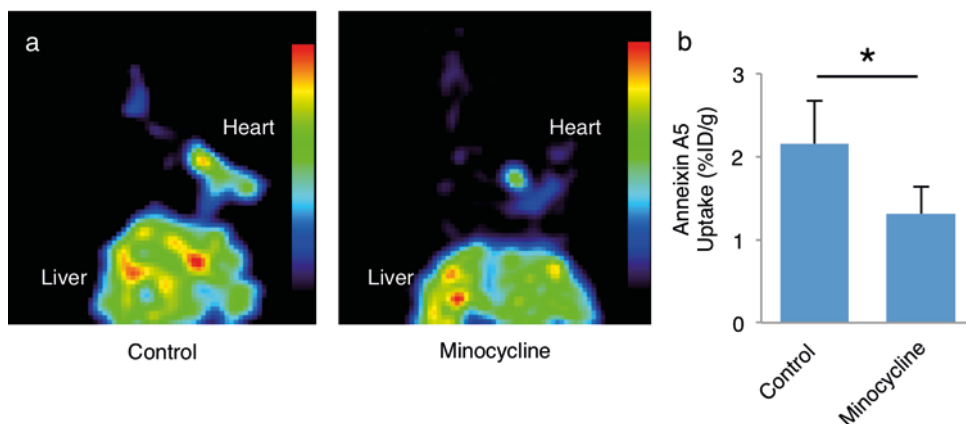
Figure 1. Quantified ^{99m}Tc-annexin SPECT imaging in mice with experimental acute myocardial infarction. *In vivo* SPECT images (a) and absolute quantification (b) revealed marked reduction of cardiac annexin A5 uptake in minocycline-treated versus untreated control mice. * = P < 0.05; SPECT = single photon emission computed tomography

To measure apoptosis in rabbits, *ex vivo* ^{99m}Tc-annexin A5 SPECT/CT imaging was performed at 3.5 hours after intravenous administration of ^{99m}Tc-annexin A5 (Figure 2a). Comparison between the two groups shows lower uptake of ^{99m}Tc-annexin A5 in the minocycline-treated rabbits. Quantification of radiotracer uptake by gamma counting revealed a trend of lower radiotracer uptake (%ID/g) in the infarcted apical

slice of minocycline treated animals versus non-treated animals (0.29 ± 0.14 versus 0.4 ± 0.16, P = 0.33, Figure 2b).

In slices 2 and 3, uptake was similar in treated and non-treated animals (Slice 2: 0.19 ± 0.07 versus 0.21 ± 0.10, P = 0.86, slice 3: 0.14 ± 0.05 versus 0.16 ± 0.07, P = 0.70).
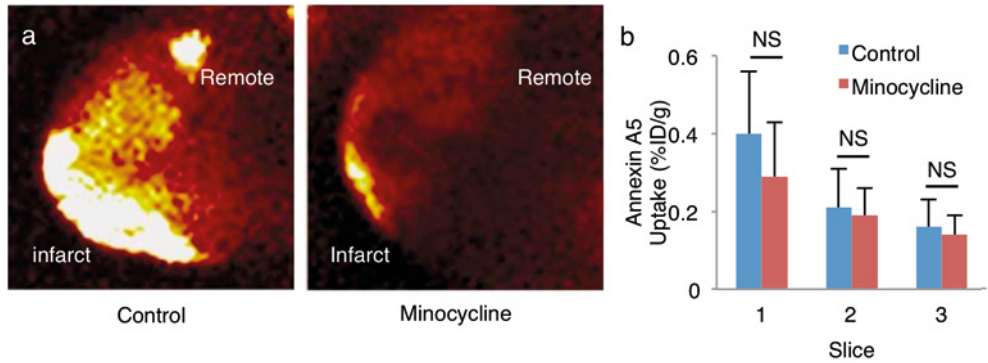
Figure 2. ^{99m}Tc-annexin A5 uptake in rabbits with experimental acute myocardial infarction. *Ex vivo* planar imaging (a) and gamma counting (b) show a trend of lower uptake in the infarcted apical slice in minocycline-treated than in untreated control animals. NS = statistically not significant

Immunohistopathological measurement of cardiac apoptosis in mice

Figure 3a shows representative examples of TUNEL-stained myocardial tissue sections. The percentage of TUNEL positive cells was markedly lower in minocycline treated mice than in non-treated mice (0.16 ± 0.10 versus 0.54 ± 0.32, P = 0.034, Figure 3b).

Figure 3. TUNEL staining in mice with experimental acute myocardial infarction. Representative examples of TUNEL staining (a) and their quantification (b) demonstrate a marked reduction of apoptotic cells among minocycline-treated versus untreated control mice. Arrows: TUNEL-positive cells. * = P < 0.05. TUNEL = terminal deoxynucleotidyl transferase-mediated deoxyuridine triphosphate nick-end labeling

Discussion

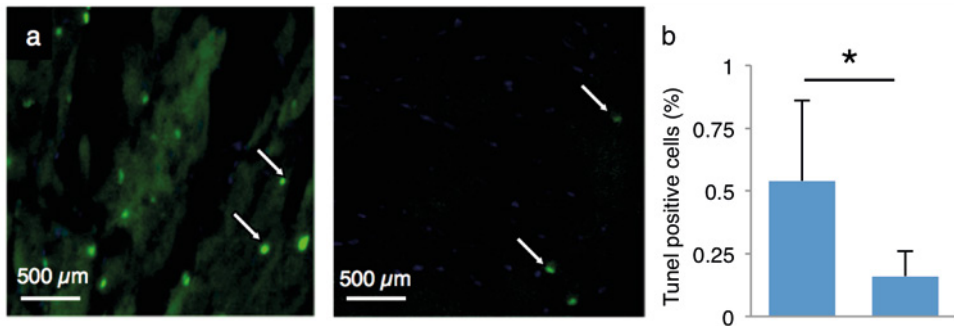Here were report initial evidence of reduction of (apoptotic) cell death by minocycline administration upon reperfusion in mice and rabbits with experimental acute myocardial infarction. For optimal assessment of cardiac apoptosis, in and *ex vivo* ^{99m}Tc-annexin A5 imaging was employed.

Considerable experience with minocycline therapy in cerebrovascular event, the pathology of which is similar to that of myocardial infarction, has been obtained. Extensive pre-clinical work suggests that minocycline therapy after CVA, reviewed in (183) Initial clinical studies indicate that minocycline therapy after CVA is well tolerated in intravenous doses of up to 10mg/kg (184), may reduce hemorrhagic transformation (197) and improve neurologic functional outcome (185-187).

Moreover, several studies have demonstrated cardioprotection by minocycline in animal models of acute myocardial infarction. Employing a Langendorff set-up, Scarabelli and co-workers reported the first evidence of minocycline's protective effects in cardiac ischemia and reperfusion (8). They demonstrated that minocycline reduces apoptosis, and infarct size, and decline in heart function. They moreover demonstrated that the anti-apoptotic effect is multifaceted and encompasses direct inhibition of the caspase cascade, and reduction of mitochondrial leakage of pro-apoptotic mediators (189). Next, Romero-Perez and colleagues confirmed in a rats with experimental cardiac ischemia and reperfusion that minocycline treatment reduces infarct size by approximately 33% (188). Moreover, they demonstrated that minocycline specifically accumulates in the infarct area, reduces Matrix Metalloproteinase-9 (MMP-9) activity and oxidative stress. Thereafter, Hu offered further support for reduction of apoptosis and infarct size by minocycline, and added that this may in part be due to reduced release of the inflammatory mediator high mobility group box 1 protein release (190). Finally, a second study by Hu et al demonstrated minocycline-induced reduction of ventricular arrhythmias after myocardial ischemia and reperfusion (191).

In the studies evaluating cardio protective effects of minocycline, time of administration was before induction of ischemia. This challenges translation to clinical practice, where treatment can only be administered after onset of ischemia. The current study adds to the previous studies, as it is the first study evaluating cardioprotection by minocycline administration upon reperfusion.

The current study has several limitations. Gamma counting demonstrated a trend of reduced ^{99m}Tc-annexin A5 uptake in the infarcted apical slice of rabbit hearts. However, due to unexpectedly high mortality rates, sample size (4 in each group) was too small to obtain statistically significant results. Moreover, although reduction of cardiac apoptosis in mice was demonstrated in a robust manner by TUNEL staining, ^{99m}Tc-annexin SPECT image analysis was sub-optimal due to technical difficulties with dual tracer image reconstruction. Thus, the current results indicating cardioprotection by minocycline administration upon reperfusion in mouse and rabbit models of acute myocardial infarction may best be seen as exploratory rather than definitive.

Chapter 4

Noninvasive Molecular Imaging of Cardiac Cell Death using ^{111}In-GSAO

Hans J. de Haas[1,2],*, Nobuhiro Tahara[3],*, H. Reinier Zandbergen[4],*, Artiom Petrov[1], Raghu Pandurangi[5], Takayoshi Yamaki[6], Jun Zhou[1], Tsutomu Imaizumi[3], Riemer H.J.A. Slart[2], Mary Dyszlewski[5], Tiziano Scarabelli[1], Annapoorna Kini[1], Chris Reutelingsperger[4], Navneet Narula[7], Valentin Fuster[1,8], Jagat Narula[1]

1. Zena and Michael A. Wiener Cardiovascular Institute, Icahn School of Medicine at Mount Sinai, New York, New York;
2. Department of Nuclear Medicine and Molecular Imaging, University of Groningen, University Medical Center Groningen, the Netherlands;
3. Division of Cardio-Vascular Medicine, Department of Medicine, Kurume University School of Medicine, Kurume, Japan;
4. Cardiovascular Research Institute Maastricht, Maastricht University, Maastricht, Netherlands;
5. Covidien Imaging Solutions, Hazelwood, Missouri;
6. Department of Cardiology and Hematology, Fukushima Medical University, Japan;
7. Department of Pathology, Weill Cornell Medical College, New York, NY;
8. Centro Nacional de Investigaciones Cardiovasculares (CNIC), Madrid, Spain.

* Authors contributed equally

Abstract

Acute insult to the myocardium is associated with substantial loss of cardiomyocytes during the process of myocardial infarction. In this setting, apoptosis (programmed cell death) and necrosis may operate on a continuum. Because the latter is characterized by the loss of sarcolemmal integrity, we propose that an appropriately labeled tracer directed at a ubiquitously present intracellular moiety would allow non-invasive definition of cardiomyocyte necrosis. A trivalent arsenic peptide, GSAO (4-(N-(S-glutathionylacetyl)amino)phenylarsonous acid), is capable of binding to intracellular dithiol molecules such as heat shock protein 90 (HSP90) and filamin-A. Since GSAO is membrane impermeable and dithiol molecules are abundantly present intracellularly, we propose that myocardial localization would represent sarcolemmal disruption or necrotic cell death. In rabbit and mouse models of acute myocardial infarction and a mouse model of chronic myocardial infarction, we employed ^{111}In-labelled GSAO for noninvasive radionuclide molecular imaging. ^{111}In-GSAO uptake was observed within the regions of apoptosis seeking agent ^{99m}Tc-annexin A5 uptake, suggesting the co-localization of apoptotic and necrotic cell death processes.

Introduction

Cell death plays a central role in various cardiovascular diseases. Two morphologically distinct modes of cell death - apoptosis (a programmed process characterized by enzymatic degradation and clean removal of the cell) and necrosis (an uncontrolled process characterized by cell swelling, membrane rupture and spill of its contents) have been reported to contribute to the myocardial tissue loss. It is being increasingly realized that apoptosis and necrosis, rather than being entirely independent, may operate on a continuum, at least in response to noxious stimuli (198-200).

Numerous strategies have been proposed for the detection of cell death early after onset of ischemia within the time window amenable to intervention. Most experience for the recognition of apoptosis has been obtained with single photon emission computed tomography (SPECT) using ^{99m}Tc-annexin A5. ^{99m}Tc-annexin A5 targets externalized phosphatidylserine (PS) on membranes of cells with active apoptotic signaling (201) and the clinical feasibility of ^{99m}Tc-annexin A5 imaging has been demonstrated in the setting of myocardial infarction (121,202), transplant rejection (203) and heart failure(122). On the other hand, several radiotracers targeting necrotic cells through membrane disruption have been developed (116,204,205). Notably, antimyosin antibody imaging has been successfully employed for the detection of myocardial necrosis associated with myocardial infarction (204), myocarditis (204), heart failure (206) and cardiac allograft rejection (206). However due to technical disadvantages, the necrosis-avid radiotracers have not become popular.

4-(N-(S-glutathionylacetyl)amino)phenylarsonous acid (GSAO) labelled with fluorophores and radionuclides has been used for targeting of cell death in culture, in tumor-bearing mice, and in mice with experimental brain trauma (207-209). The principle behind GSAO cell death targeting is displayed in Figure 1. GSAO is a tripeptide with a trivalent arsenic moiety. The arsenic group binds to dithiols, which are abundantly present in intracellular milieu and virtually absent from the extracellular space (210). GSAO cannot reach its intracellular target molecules in intact cells, because it is not able to negotiate across the cell membrane (211). Cell membrane γ-glutamyl transferase (GGT) is upregulated during ischemic stress and other situations, splices off GSAO's glutamyl residue and allows cellular entrance of GSAO's metabolite GCAO (4-(N-(S-cysteinylglycylacetyl)amino) phenylarsonous acid) (211). However, when radioactive or fluorescent reporter molecules are attached to glutamyl residue of GSAO it is not able to bind to GGT, rendering the molecule membrane impermeable(207). After the necrotic process sets in and the sarcolemmal integritiy is lost; and GSAO gains free entry to the intracellular microenvironment. Of numerous dithiol-bearing intracellular targets including filamin A, eukaryotic translation elongation factor 2, and protein disulfide isomerase (PDI), HSP90 is most widely present (207). HSP90 comprises approximately 2% of the intracellular protein content and increases by two-threefold in response to acute stress including ischemia (212).

4
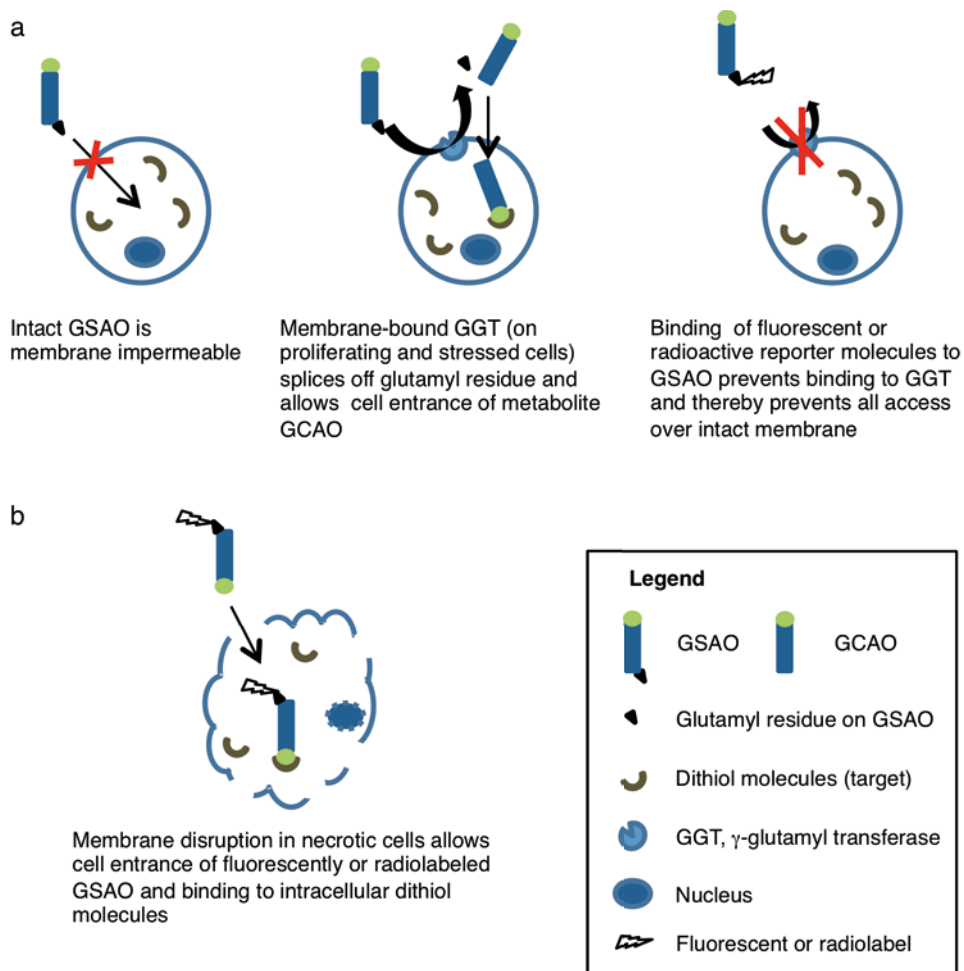
Figure 1. Targeting mechanism of GSAO. GSAO binds to dithiol molecules, which are abundant in the intracellular space and virtually absent in the extracellular space. When labelled with radioactive or fluorescent reporter molecules, GSAO cannot negotiate across the cell membrane of healthy cells (a) but gains free access through disrupted membranes of dying cells (b). Thus, labeled GSAO accumulates in dying cells. GGT = γ-glutamyl transferase; GSAO = 4-(N-(S-glutathionylacetyl)amino)phenylarsonous acid; GSCA = (4-(N-(S-cysteinylglycylacetyl)amino) phenylarsonous acid)

In this study we evaluated feasibility of cell death imaging using ^{111}In-GSAO in mouse and rabbit models of acute myocardial infarction and a mouse model of chronic myocardial infarction. In a subgroup of animals, serial SPECT and computed tomography (CT) imaging using ^{99m}Tc-annexin A5 and ^{111}In-GSAO was performed to determine the relationship between the two modes of cell death in the setting of myocardial ischemia and reperfusion. Fluorescent GSAO and annexin A5 were employed in another subgroup of animals for pathological characterization of the modes of cell death.

Methods

Production of ^{111}In-GSAO

GSAO was labeled with ^{111}In as described previously (207). Briefly, 9.2 µg GSAO coupled with diethylenetriaminepentaacetic acid (DTPA-GSAO) or DTPA-GSCA (kind gift of Covidien Imaging Solutions, Hazelwood, Missouri) was dissolved in 95 µL of 0.9% sterile saline and then added to buffer (36 µL; 0.5 mmol/L sodium acetate, trihydrate and 0.25 mmol/L ascorbic acid) and 200 µl of [111]InCl$_3$. The mixture was incubated at room temperature for 15 min. Radio-chemical purity of more than 99% was confirmed by instant chromatography.

Ethical statement

The experimental protocols followed the NIH Guidelines and were approved by the Institutional Laboratory Animal Care and Use Committees at the University of California, Irvine and University of Maastricht, Maastricht, The Netherlands.

Induction of acute and chronic myocardial infarction in mice

For fluorescence experiments, C57Bl6/j (Age: 3 months, weight: ~ 50 g, Jackson Laboratories, Sacramento, CA) and for radionuclide studies Swiss-Webster mice (Age: 3 months, weight ~ 50 g, Charles River, Wilmington, MA) were used. To simulate acute myocardial infarction followed by reperfusion therapy, ischemia and subsequent reperfusion were induced under isoflurane anesthesia (2 − 3%) using a stereomicroscope (Leica MZ FL III, Leica, Switzerland) as described previously (143). Animals were placed on a heating pad in the supine position, intubated under direct laryngoscopy, and mechanically ventilated using a small animal respirator (tidal volume, 1.0 ml; rate, 120 breaths/min, Harvard Apparatus, Holliston, MA). After a minimum thoracotomy, the anterior descending branch of the left coronary artery was ligated with a 6.0-silk suture 3 to 4 mm below the tip of the left atrium, to institute cardiac ischemia. Successful ligation was verified by visual inspection of the LV apex for myocardial blanching, indicating interruption in coronary flow. To allow reperfusion, the suture was removed after 30 min to induce reperfusion. The acute myocardial infarction animals remained under anesthesia for ensuing radionuclide imaging or fluorescence experiments. The sham operation was identical, except for the fact that the ligation was not tied.

For induction of chronic myocardial infarction, the ligation was not released. In these animals, the chest cavity was closed in layers with 6.0-silk and the skin was closed with 4.0-silk sutures. Thereafter, animals were gradually weaned from the respirator and put back into their cages until imaging procedure.

Induction of acute myocardial infarction in rabbits

To simulate reperfused acute myocardial infarction, ischemia and reperfusion were induced by temporary occlusion of left anterior descending coronary artery (LAD) in New Zealand White male rabbits (weight, 3.0–3.5 kg) as described previously (126,213). All rabbits were anesthetized with a mixture of ketamine and xylazine (100 mg/ml, 10:1 vol/vol; 2.0 to 3.0 ml subcutaneously). Surgical

tracheostomy was performed, and ventilation was maintained with a volume-cycled rodent respirator (Harvard Apparatus, Holliston, MA) provided positive pressure ventilation at 50 mL/cycle and a respiratory rate of 50 cycles/min. After the surgical procedure, anesthesia was maintained on 3 – 4% isoflurane Briefly, the heart was exposed through parasternal thoracotomy, and the pericardium was fenestrated. The LAD was identified and a monofilament suture was placed at the site. The LAD was occluded by tightening the snare created by passing suture through a polyethylene tube. The snare was removed after 40 min of occlusion to induce reperfusion. Lead II or III of the electrocardiogram was continuously monitored during the experiments to confirm myocardial ischemia. Animals remained anesthetized for ensuing radionuclide imaging experiments.

Ex vivo cardiac fluorescence microscopy in mice

Mice with acute myocardial infarction and sham-operated mice were injected with Cy5.5-labelled GSAO (a kind gift of Covidien Imaging Solutions (Hazelwood, Missouri, United States) at 5 min before ischemia and 1 hour before sacrifice, respectively. All mice received Oregon Green-labeled annexin A5 10 min before sacrifice. Of each fluorescent probe, a dosage of 2.5 mg/kg was used. Animals with acute myocardial infarction were sacrificed after 30 min after reperfusion, sham mice at 1 hour after surgery. Hearts were snap-frozen in liquid nitrogen, 7-μm frozen sections were obtained, dried and mounted in 4,6-diamino-2-phenylindole (DAPI) containing medium and examined with a confocal scanning laser microscope (Bio-Rad) equipped with a krypton/argon mixed gas laser (Ion Laser Technology).

In vivo and *ex vivo* radionuclide imaging in mice and rabbits

For mice and rabbits, the same imaging procedure was followed. *In vivo* SPECT imaging was performed at 3 hours after radiotracer administration using a dual-head micro-SPECT γ-camera combined with micro-CT (X-SPECT, Gamma Medica, Inc., Northridge, CA) under isoflurane anesthesia. SPECT images of the heart were acquired in a 64 × 64 matrix at 32 steps at 60 seconds per step with a 247 keV photo peak of ^{111}In with 15% windows using a medium energy parallel-hole collimator. In the animals also undergoing ^{99m}Tc-sestamibi or ^{99m}Tc-annexin A5 imaging, this was followed by imaging using the same protocol, at a 140 keV photo peak of ^{99m}Tc with 15% windows using a low-energy, high-resolution parallel-hole collimator. Gating was not performed. After SPECT imaging acquisition, a CT scan was acquired using an X-ray tube operating at 50 kVp and 0.6 mA. Images were acquired for 2.5 seconds per view for 256 views in a 360° rotation. After transferring to 256 × 256 matrix, the SPECT images and CT studies were fused. After imaging, anesthetized animals were terminated by heart excision. *Ex vivo* SPECT/CT of excised hearts was performed using the same protocols but at 45 seconds per step for SPECT. Thereafter, planar ^{111}In-GSAO imaging of the hearts was performed for 15 min, followed by ^{99m}Tc-sestamibi or ^{99m}Tc-annexin A5 planar imaging in GSAO-sestamibi and GSAO-annexin A5 animals. After *ex vivo* imaging, rabbit hearts were cut into 4 short axis slices and further divided into 31 – 32 pieces. Mouse hearts were cut in 3 short-axis slices. All sections were weighed, and γ-counted in an automatic well-type γ-counter (Perkin Elmer Wallac Inc., Gaithersburg, MD) for calculation of the percent injected dose per gram of tissue (%ID/g) uptake. Tissue samples of the main organs were used for calculation of the %ID/g uptake to evaluate the bio distribution. To correct for the radioactive decay and permit

calculation of the concentration of radioactivity as a fraction of the administered dose, aliquots of the injected dose were counted simultaneously. For evaluation of infarct ^{111}In-GSAO uptake in rabbits, the section with the highest ^{111}In-GSAO uptake in the infarct area was used of each animal, and for evaluation of remote ^{111}In-GSAO uptake, the section with the lowest ^{111}In-GSAO uptake in the remote area was selected. In all mice, the apical slice was used for evaluation of infarct uptake, the middle slice for uptake in the border zone and the basal slice for remote uptake.

Pharmacokinetic studies in rabbits

The pharmacokinetic parameters were derived using the KINFIT module of the MW/PHARM computer program package (Version 3.60, MediWare, Groningen, The Netherlands) (214). The data, consisting of the blood concentration of ^{111}In radioactivity or GSAO versus time, were analyzed by non-linear regression analysis using a least-squares weighted simplex algorithm, with data weighted with the reciprocal of the observed value.

(Immuno)histopathologial evaluation of cardiac cell death

After γ-counting of ^{111}In-GSAO uptake, myocardial pieces of seven rabbits were processed for histopathologic characterization. Of each animal, two pieces from each region (infarct, border zone, remote) were selected.

The myocardial pieces were fixed overnight 4% paraformaldehyde in phosphate-buffered saline (PBS) (pH 7.4 at 4°C), and stored in PBS with 0.02% sodium azide at 4°C until used. The specimens were further processed by dehydration in a graded series of ethanol for paraffin-embedding. The blocks were cut in 5-μm thick sections, floated on a water bath containing deionized water (43°C), and transferred to vectabond (Vector Laboratories Burlingame, California) reagent-treated slides (Vector SP-1800, Vector Laboratories), dried overnight, and stored until ready for use. Sections were deparaffinized by heating (25 min at 56°C) and dehydration using xylene and graded series of ethanol. Tissue sections were stained with standard Haematoxylin & Eosin and Masson's trichrome staining. For immunohistochemical characterization, adjacent sections were incubated with primary antibodies against Caspase-3. After washing with PBS, sections were incubated with a biotinylated secondary antibody. The presence of apoptotic cells was further evaluated using terminal deoxynucleotidyl transferase-mediated deoxyuridine triphosphate nick-end labeling (TUNEL) staining as described previously. Briefly: exposed DNA fragments were labeled with biotinylated nucleotides and terminal deoxynucleotidyl transferase for 1 h at 37°C after blocking of endogenous peroxidase activity using 0.3% hydrogen peroxide and incubation with proteinase K (46). For color reactions, sections were incubated with diaminobenzidine. For the assessment of the immunopositive area, stained tissue sections were observed under appropriate magnification (Carl Zeiss, Thornwood, New York), and the images were captured with a high-resolution digital camera (Axiocam, 1,300 × 1,030 pixels, Carl Zeiss) using Axiovision 3.1 software. Digital images were analyzed using Image-Pro Plus 5.0 (Media Cybernetics, Bethesda, Maryland).

Statistical analysis

All results are presented as the mean ± SD In most cases, the data did not meet the assumptions of parametric tests. For consistency, non-parametric tests were used for all comparisons. Related samples were compared using Wilcoxon Signed Rank test (two groups) or Friedman's Two Way analysis of variance (ANOVA) followed by post-hoc Wilcoxon Signed-Rank tests and Bonferroni correction for pair-wise significance (more than two groups). Unrelated samples were compared using Mann Whitney U tests (two groups) or Kruskal-Wallis ANOVA followed by Mann-Whitney U tests and Bonferroni Correction for pair-wise significance (more than two groups). When the Kruskal-Wallis test revealed no significant differences among groups, no post-hoc tests were performed and P = NS was reported. Bonferroni correction was also applied to results of multiple Wilcoxon signed rank tests regarding the uptake of radiotracers in infarct versus remote areas in rabbits. To assess the correlation between ^{111}In-GSAO uptake and ^{99m}Tc-annexin A5 uptake, ^{99m}Tc-sestamibi uptake and histological findings (caspase-3 and TUNEL), Spearman's ρs were calculated. P values < 0.05 were considered statistically significant.

Results

Fluorescence microscopic characterization of GSAO uptake

Uptake characteristics of GSAO were evaluated and compared with annexin A5 in mice with acute myocardial infarction and sham-operated mice. Experimental acute myocardial infarction was induced by 30-min coronary ligation followed by 30 min of reperfusion. Sham procedure was identical, except that coronary ligation was not performed. Mice with acute myocardial infarction (n = 3) and sham-operated mice (n = 3) were injected Cy5.5-labelled GSAO and Oregon Green-labeled annexin A5. Qualitative fluorescent microscopic analysis of heart sections showed that cardiomyocytes of sham-operated mice were positive neither for GSAO nor for annexin A5. In contrast, in hearts of mice with experimental acute myocardial infarction, cardiomyocytes positive for GSAO and annexin A5 were observed (Figure 2a–c). Interestingly, all GSAO-positive cardiomyocytes bound annexin A5 (Figure 2a–c), suggesting that necrosis in the reperfused myocardium coexists with apoptotic signaling. Not all annexin A5-positive cardiomyocytes had taken up GSAO (Figure 2c).
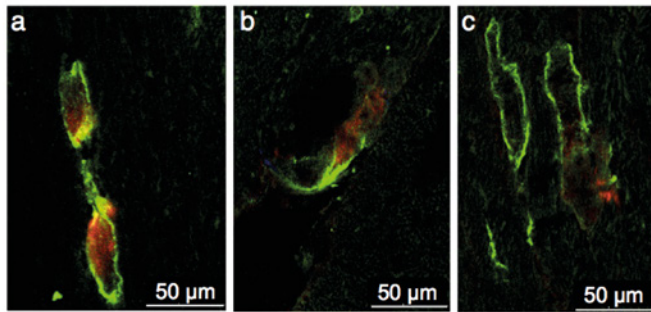
Figure 2: Characterization of target binding of GSAO in mice with experimental acute myocardial infarction. Heart sections of mice with experimental acute myocardial infarction, injected with fluorescently labeled GSAO and annexin A5. (a, b) GSAO accumulation (red) was only observed in cells with annexin A5-positive cell membranes (green). (c) Not all annexin A5-positive cells were not GSAO-positive.

^{111}In-GSAO imaging in rabbits and mice with acute myocardial infarction

Acute myocardial infarction was induced in rabbits and mice by coronary ligation for 40 and 30 min, respectively. Reperfusion was achieved by removal of the suture and ^{111}In-GSAO was administered thirty min later. Three hours thereafter, *in vivo* SPECT/CT imaging was performed, animals were sacrificed and hearts were explanted. Next, *ex vivo* SPECT/CT and planar cardiac imaging were performed. Then, rabbit hearts were cut into ca. 32 small pieces and mice hearts were sectioned in three short axis slices: basal (remote area), middle (border zone) and apical (infarct). Radiotracer uptake was quantified by γ-counting, and myocardial pieces were histopathologically characterized.

In vivo SPECT/CT imaging in rabbits with acute myocardial infarction (n = 10) revealed intense uptake of ^{111}In-GSAO in the apical area (Figure 3a). *Ex vivo* SPECT/CT (not shown) and planar imaging (Figure 3b) of explanted hearts confirmed intense apical radiotracer uptake. γ-counting confirmed that the ^{111}In-GSAO uptake (%ID/g) in the myocardial infarct was markedly higher than the ^{111}In-GSAO uptake in the remote region (1.10 ± 0.45 versus 0.03 ± 0.01, P = 0.005, Figure 3c).
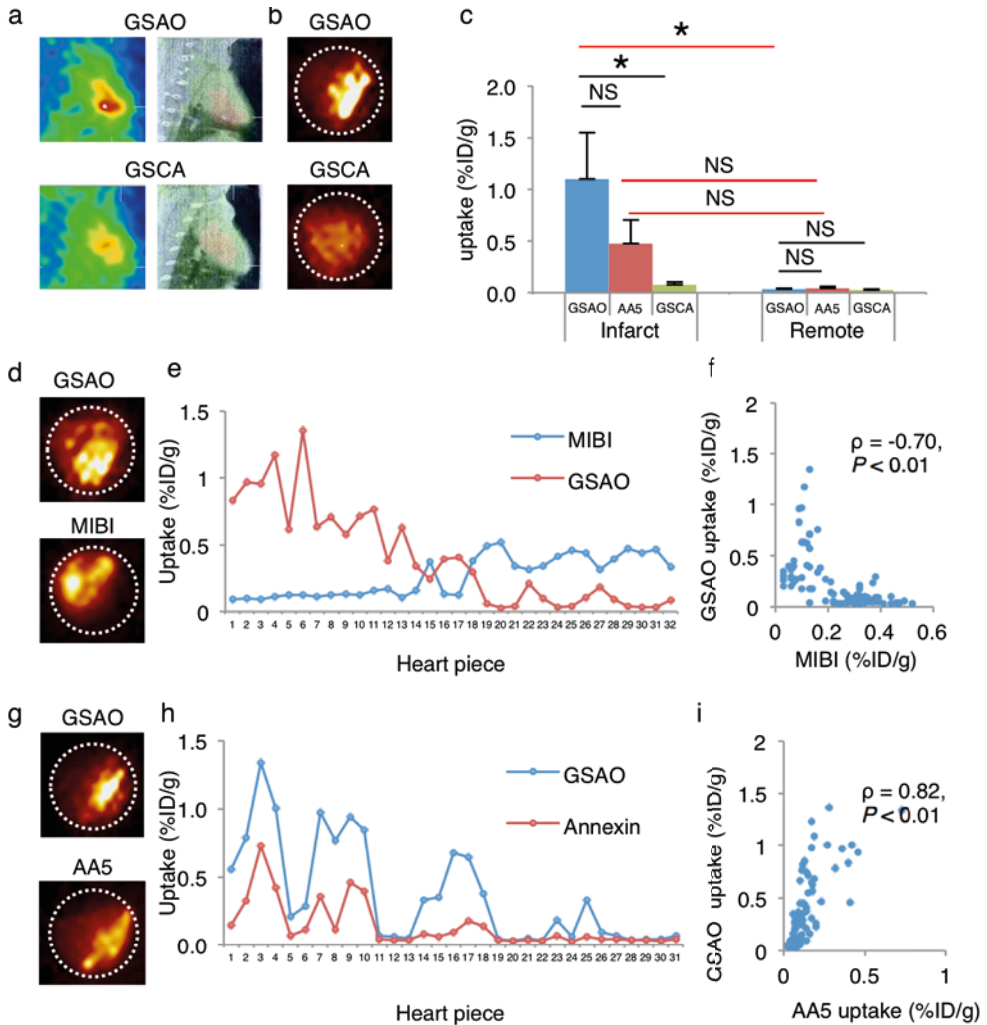
4

Figure 3: ^{111}In-GSAO imaging, quantification and comparison with ^{99m}Tc-annexin A5 and ^{99m}Tc-sestamibi in rabbits with experimental acute myocardial infarction. (a) *In vivo* SPECT (left panels), and fused SPECT/CT images (right panels) in rabbits with acute myocardial infarction revealed intense ^{111}In-GSAO uptake (top) and only modest uptake of radiotracer control compound ^{111}In-GSCA (bottom). (b) *Ex vivo* planar images confirmed intense ^{111}In-GSAO uptake (top) and modest ^{111}In-GSCA (bottom) uptake. (c) γ-counting of myocardial sections confirmed ^{111}In-GSAO uptake in infarct was higher than in remote area and higher than ^{111}In-GSCA uptake in infarct. Although low, ^{111}In-GSCA uptake in infarct was higher than remote. Difference Between ^{111}In-GSAO and ^{99m}Tc-annexin A5 uptake did not reach significant uptake. Black horizontal lines denote Kruskal-Wallis ANOVAs + Bonferroni correction, and red lines denote Wilcoxon signed rank tests + Bonferroni correction. (d) Serial imaging revealed that ^{111}In-GSAO uptake (top) was predominantly localized in the region of the ^{99m}Tc-sestamibi perfusion defect (bottom). (e) γ-counting of myocardial sections showed high ^{111}In-GSAO uptake in sections with low ^{99m}Tc-sestamibi uptake and vice versa. (f) A significant inverse Spearman's correlation between uptake of ^{111}In-GSAO and ^{99m}Tc-sestamibi was observed. (g) Serial planar imaging in acute myocardial infarction rabbit demonstrates similar uptake region and higher uptake of ^{111}In-GSAO (top) when compared with ^{99m}Tc-annexin A5 (bottom). (h) γ-counting of myocardial sections showed high ^{111}In-GSAO uptake in sections with high ^{99m}Tc-annexin A5 uptake and vice versa (i). A significant Spearman's correlation between uptake of ^{111}In-GSAO and ^{99m}Tc-annexin A5 was observed. %ID/g = percent injected dose per gram of tissue; AA5 = ^{99m}Tc-annexin 5; MIBI = ^{99m}Tc-sestamibi.

To study the specificity of ^{111}In-GSAO, the myocardial uptake of negative control compound GSCA was evaluated in rabbits with acute myocardial infarction (n = 5). *In vivo* (Figure 3a) and *ex vivo* SPECT/CT imaging and planar (Figure 3b) imaging revealed very low cardiac uptake of GSCA; only slightly increased infarct uptake was observed. This was confirmed by γ-counting (Figure 3c); when compared with ^{111}In-GSAO, ^{111}In-GSCA uptake (%ID/g) in the infarct area was significantly lower (0.07 ± 0.03 ID/g, P = 0.002). Although low, ^{111}In-GSCA uptake in the infarct area was higher than in the remote area (0.03 ± 0.01, P = 0.043, Figure 3c). This demonstrated that the trivalent arsenical group was necessary for targeting of dying cells. Moreover, myocardial ^{111}In-GSAO uptake in an unmanipulated control animal was similar to ^{111}In-GSAO uptake in the spared myocardium of rabbits with myocardial infarction (0.01 versus 0.03 ± 0.01, data not shown), further supporting specificity of GSAO.

To evaluate localization of cardiac ^{111}In-GSAO uptake, three of ten animals receiving ^{111}In-GSAO also received the myocardial perfusion tracer ^{99m}Tc-sestamibi, immediately after coronary ligation. Serial *in vivo* SPECT/CT imaging confirmed that ^{111}In-GSAO uptake was localized in the infarct zone as identified by ^{99m}Tc-sestamibi perfusion defect (not shown). Similarly, *ex vivo* serial SPECT/CT imaging and serial planar imaging (Figure 3d) revealed uptake of ^{111}In-GSAO in the infarct zone as shown by ^{99m}Tc-sestamibi perfusion defect. In each animal, γ-counting of ^{99m}Tc-sestamibi and ^{111}In-GSAO in myocardial sections confirmed increased uptake of ^{111}In-GSAO in the perfusion defects as sections with low ^{99m}Tc-sestamibi uptake showed increased ^{111}In-GSAO uptake and vice versa (Figure 3e). γ-counting of all myocardial sections from the animals receiving both ^{111}In-GSAO and ^{99m}Tc-sestamibi revealed an inverse correlation between ^{111}In-GSAO uptake and ^{99m}Tc-sestamibi uptake (ρ = −0.70, P < 0.01, Figure 3f).

Of ten animals receiving ^{111}In-GSAO, three also received ^{99m}Tc-annexin A5. Serial *in vivo* SPECT/CT imaging with ^{111}In-GSAO and ^{99m}Tc-annexin A5 revealed similar area of increased uptake; ^{111}In-GSAO uptake was more intense than ^{99m}Tc-annexin A5 uptake. This was confirmed by *ex vivo* serial SPECT/CT imaging and *ex vivo* serial planar imaging (Figure 3g). Quantitative tracer uptake paralleled the imaging data. In each animal, in sections with increased ^{99m}Tc-annexin A5 uptake, ^{111}In-GSAO uptake was also increased (Figure 3h). Using all myocardial sections in all animals receiving ^{111}In-GSAO and ^{99m}Tc-annexin A5, a strong correlation between uptake of the radiotracers was observed (ρ = 0.82, P < 0.01, Figure 3i). Like the fluorescence experiments, this supports that secondary necrosis after apoptotic signaling may be the dominant mode of cell death in (reperfused) myocardial infarction. The ^{111}In-GSAO uptake (%ID/g) in the infarct zone was higher than ^{99m}Tc-annexin A5 uptake, although the results did not reach statistical significance, due to the small sample size (1.10 ± 0.45 versus 0.47 ± 0.23, P = 0.47). Uptake in the remote area was low for both tracers (0.03 ± 0.01% versus 0.04 ± 0.02, P = NS).

(Immuno)histopathological evaluation of cardiac damage in rabbits

After γ-counting myocardial pieces from infarct, border and remote zones were histologically characterized. Representative examples of the stainings are given in Figure 4a. H&E staining revealed hypereosinophilic change and contraction band necrosis in the myocardial sections from the infarct area; the morphological changes were less frequent in the border zone. The remote area was morphologically normal. The rate of apoptosis as shown by TUNEL staining (expressed as percent area positive) was higher in the infarct (2.83 ± 1.42) and border zone (2.55 ± 1.84) than in the remote zone

(0.02 ± 0.0, P < 0.001 for both). Caspase staining (expressed as percent area positive) revealed similar results: the percentage of the are positively stained was higher in the infarct than in the remote zone (1.04 ± 0.48 versus 0.46 ± 0.48, P = 0.054). ^{111}In-GSAO uptake in the myocardial sections showed a direct correlation with TUNEL (ρ: 0.743, P < 0.001, Figure 4b) and Caspase-3 (ρ = 0.533, P < 0.001, Figure 4c) stains, further supporting that necrosis as shown by GSAO is secondary after apoptotic signaling.
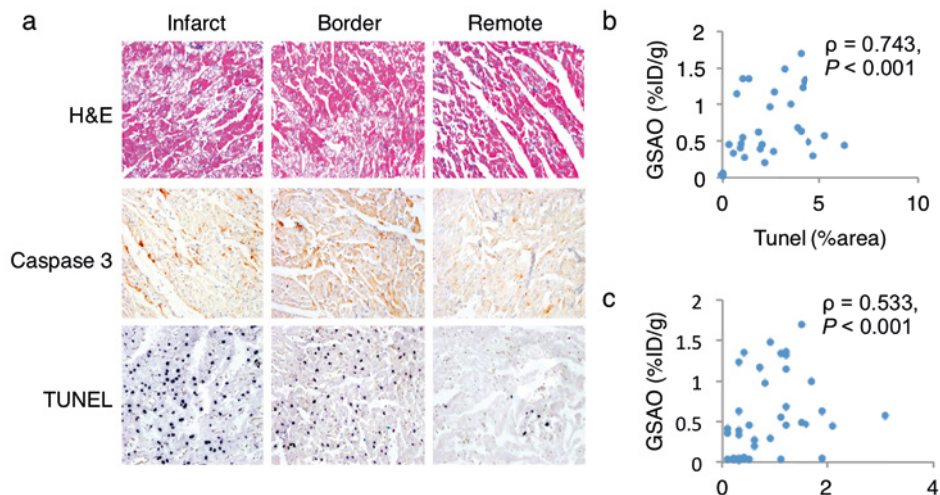
Figure 4: Histopathological characterization and relationship with of ^{111}In-GSAO uptake in rabbits with experimental acute myocardial infarction. H&E staining demonstrates clear signs of tissue damage in infarct and border zone, whereas the remote zone is morphologically normal. TUNEL and Caspase-3 stains demonstrate substantial apoptosis in the infarct zone, whereas positive cells are rarely seen in the remote area. Significant Spearman's rank correlations between ^{111}In-GSAO uptake and apoptotic signaling as shown by TUNEL (b) and Caspase-3 (c) stains were observed. H&E = haematoxylin and eosin; TUNEL = terminal deoxynucleotidyl transferase-mediated deoxyuridine triphosphate nick-end labeling.

Pharmacokinetic and biodistribution studies in rabbits

The non-target organ distribution of ^{111}In-GSAO and ^{111}In-GSCA demonstrated kidney to be the major organ of radiation burden and urine major route of excretion; all other organs revealed minimum burden for both radiotracers (Figure 5a). Serial blood samples from six animals revealed bi-exponential blood clearance with an initial fast component $T_{1/2}\alpha$ of 5.3 min followed by a slower component $T_{1/2}\beta$ of 9.7 h; the plateau phase was approached at 15 min (Figure 5b).
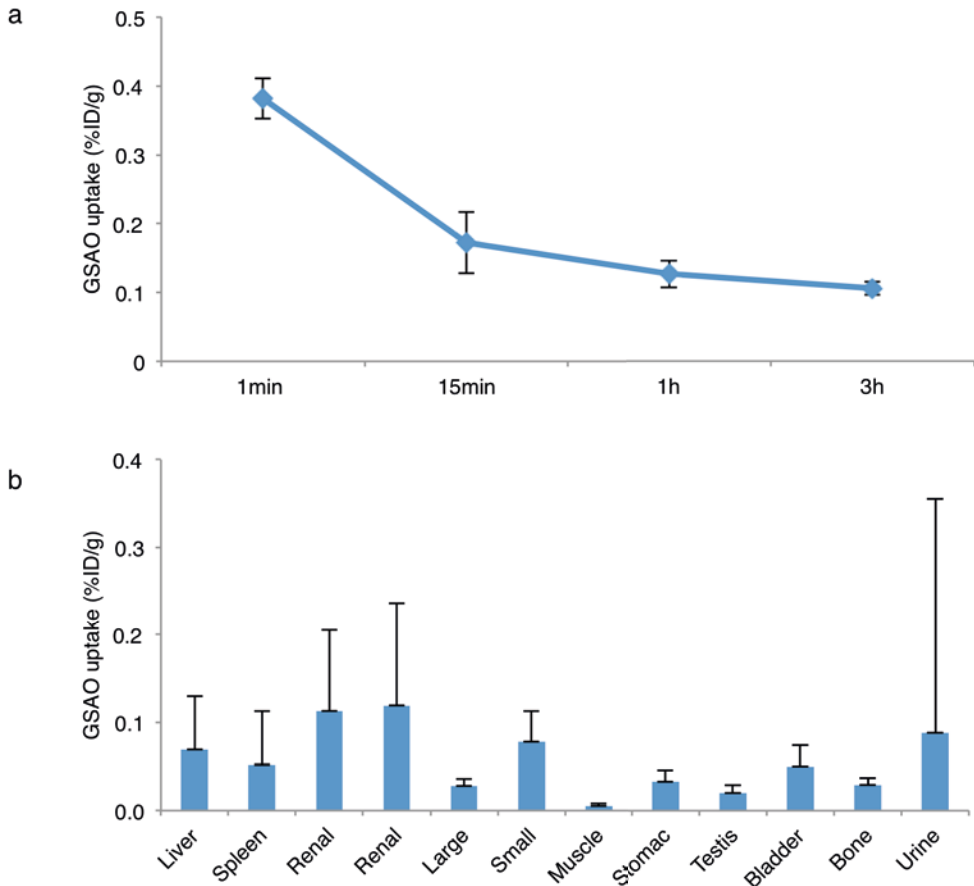
Figure 5. Blood clearance and biodistribution studies. (a) Serial blood sampling revealed rapid clearance of ^{111}In-GSAO from the blood. (b) Biodistribution studies revealed mostly renal clearance and low background uptake in the other organs.

In vivo SPECT/CT imaging in mice after acute myocardial infarction (n = 6) demonstrated high ^{111}In-GSAO uptake (Figure 6a); the use of CT allowed precise localization of the radioactivity in the infarcted region of the heart (Figure 6b). Specific apical uptake was confirmed by *ex vivo* SPECT/CT (not shown) and planar imaging (Figure 6c). Imaging experiments revealed absence of specific ^{111}In-GSAO uptake in control animals. ^{111}In-GSAO uptake (%ID/g) in the infarct area was markedly higher than in remote myocardium (2.56 ± 2.75 versus 0.48 ± 0.22, P = 0.028, Figure 6d) and 20-fold higher than apical uptake in non-manipulated control animals (n = 5, 0.13 ± 0.02; P = 0.004, Figure 6d).
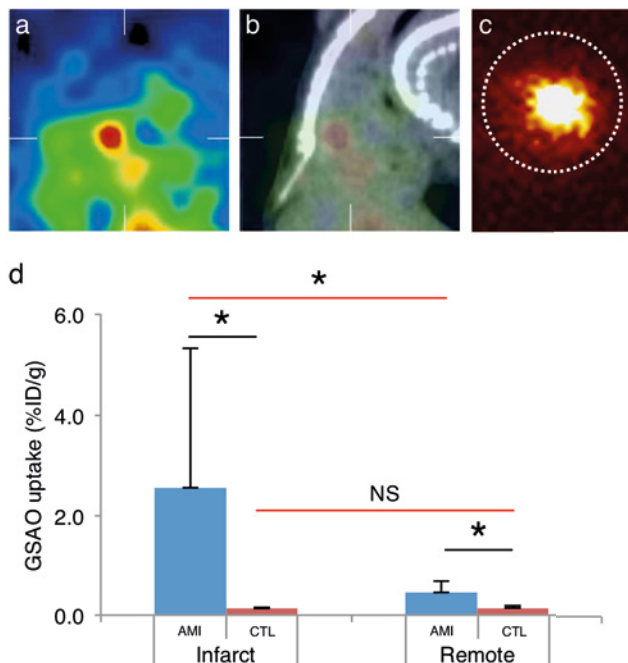
Figure 6. In vivo and ex vivo ^{111}In-GSAO imaging and quantification in mice with acute myocardial infarction. *In vivo* SPECT (a), and fused SPECT/CT images (b) in rabbits with acute myocardial infarction revealed intense cardiac ^{111}In-GSAO uptake. (c) *Ex vivo* planar images confirmed intense ^{111}In-GSAO uptake. (d) γ-counting of myocardial sections confirmed ^{111}In-GSAO uptake in infarct (apex) was higher manyfold higher than in remote area and higher than apical ^{111}In-GSAO uptake in non-manipulated control animals. Black horizontal lines denote Mann-Whitney U tests and red lines denote Wilcoxon signed rank tests. AMI = acute myocardial infarction; CT = computed tomography; ctl = control; NS = statistically not significant; SPECT = single photon emission computed tomography.

^{111}In-GSAO imaging in mice with chronic myocardial infarction

^{111}In-GSAO uptake was also evaluated in a mouse model of chronic myocardial infarction, in which the LCA territory was not reperfused. Subgroups underwent imaging experiments at different time points. Also, a disease control group consisting of animals that did not undergo infarction surgery before ^{111}In-GSAO imaging, and a radiotracer control group consisting of animals receiving negative control compound ^{111}In-GSCA imaging at 2 weeks after myocardial infarction were used. Results of radiotracer uptake quantification are shown in Figure 7. ^{111}In-GSAO uptake in mice with chronic myocardial infarction was markedly lower than in those with acute myocardial infarction, and could not be detected by *in vivo* SPECT/CT imaging. Quantification of radionuclide uptake in short axis slices confirmed that infarct uptake of ^{111}In-GSAO (%ID/g) in mice at 2 weeks after myocardial infarction (n = 6) was higher than in the five disease control animals that did not undergo infarction surgery (0.42 ± 0.17 versus 0.13 ± 0.02, P = 0.025); remote uptake was not statistically different (0.25 ± 0.12 versus 0.14 ± 0.04, P = 1.0). Moreover, ^{111}In-GSAO uptake at 2 weeks after myocardial infarction was significantly higher than uptake of the negative control compound ^{111}In-GSCA in the infarct and remote area (0.04 ± 0.02, P < 0.001 and 0.04 ± 0.03, P = 0.004, respectively).
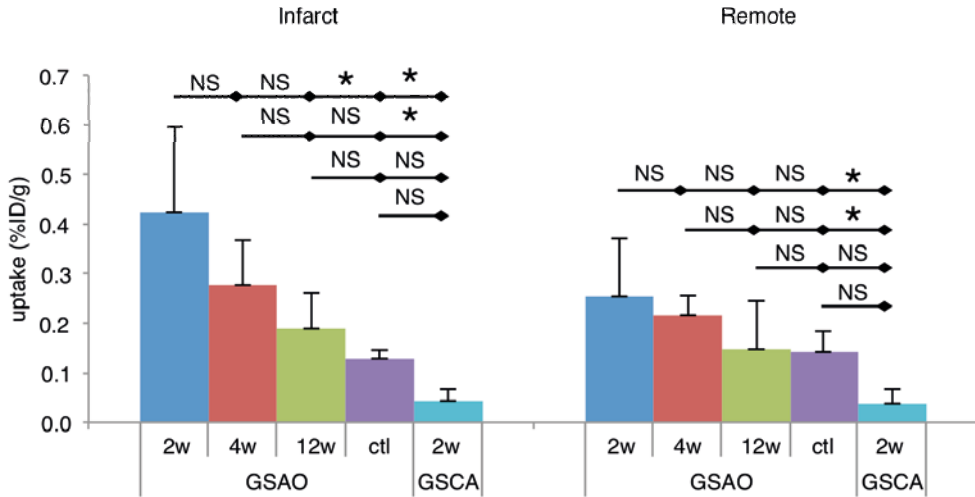
Figure 7. Quantification of ^{111}In-GSAO uptake in mice with chronic myocardial infarction. γ-counting revealed ^{111}In-GSAO uptake in the infarct area at 2 weeks; uptake was significantly higher than ^{111}In-GSAO uptake in non-manipulated control animals and uptake of negative control compound ^{111}In-GSCA at 2w after myocardial infarction. A trend of declining ^{111}In-GSAO uptake over time was observed, but did not reach statistical significance. ^{111}In-GSAO uptake in remote area was higher than ^{111}In-GSCA uptake at 2w after myocardial infarction. Results of Kruskal-Wallis ANOVAs + Bonferroni correction are shown.

Discussion

Here we demonstrate cell death imaging using ^{111}In-GSAO in animal models of acute and chronic myocardial infarction. The specificity of the radiotracer was confirmed by the localization of ^{111}In-GSAO in the infarct zone as shown by ^{99m}Tc-sestamibi. This was further supported by the lack of uptake of fluorescently labeled GSAO in sham-operated animals outside of the regions directly damaged by the suture. The lack of GSCA uptake in our radionuclide studies confirmed that the trivalent arsenic group on GSAO is responsible for its targeting characteristics (209,215,216). The radiotracer showed favorable pharmacokinetic profile with rapid blood clearance and low background uptake in most organs.

In the 1990's evidence of apoptotic signaling in myocardial infarction accumulated (217-220) sparking the discussion over the relative importance of the apoptotic and necrotic forms of cell death. In 2000, ^{99m}Tc-annexin A5 SPECT in patients with acute myocardial infarction revealed intense uptake in the entire region of the perfusion defect (121). This observation was provocative as ^{99m}Tc-annexin A5 was believed to identify apoptotic cell death but the infarct area was traditionally expected to be necrotic. It was subsequently proposed that the ischemic insult may be initiated as apoptosis but conclude with secondary necrosis. Ischemic loss of adenosine triphosphate (ATP) production during myocardial infarction would preclude completion of the energy-dependent apoptosis program (123). Restoration of blood flow by reperfusion may either interrupt the apoptotic process to allow cell salvage (126,202) or resume the process of apoptosis in critically damaged cells (218,220). The latter may even be augmented further by production of radical oxygen species (221), or intracellular calcium overload

(222). These changes may also contribute to secondary necrosis by opening of the mitochondrial permeability transition pore (182,215,216,223). It is conceivable that the apoptotic process initiated by noxious stimuli may not follow classical picture of physiologic apoptosis observed during normal turnover of skin or mucosal cells.

The feasibility of cell death imaging using fluorescently labeled and radiolabelled GSAO has recently been demonstrated in tumor-bearing mice and mice with experimental brain trauma (207-209). GSAO accumulation was characterized by fluorescent microscopy in various cell models of apoptotic and in explanted brains and tumors after *in vivo* GSAO administration. GSAO was observed intracellularly and co-localized with propidium iodide and Sytox blue, standard markers of membrane disruption, which supported GSAO uptake in secondarily necrotic cells. Similarly, our fluorescent experiments showed that GSAO accumulated intracellularly and only occurred in annexin A5-positive cells, thereby supported the notion that necrosis follows apoptotic signaling in the setting of acute myocardial infarction.

In vivo and *ex vivo* ^{111}In-GSAO imaging in rabbits and mice with acute myocardial infarction injury showed intense dual serial imaging with ^{99m}Tc-annexin A5 and ^{111}In-GSAO in rabbits after acute myocardial ischemia and reperfusion revealed the same area of uptake. At a segment level, ^{111}In-GSAO uptake showed the same pattern as ^{99m}Tc-annexin A5 and a strong correlation between uptakes of the two tracers was shown. In addition, ^{111}In-GSAO correlated with presence of Caspase-3 and TUNEL staining, classic markers of apoptosis. This shows that not only does secondary necrosis after apoptotic signaling occur in myocardial ischemia and reperfusion, it may play a dominant role. As in rabbits, high ^{111}In-GSAO uptake was seen in mice with acute myocardial infarction. However, ^{111}In-GSAO uptake in mice with chronic myocardial infarction was too low to be detected by SPECT/CT imaging. The most important explanation for this is the lower rate of necrotic cell death at later stages after myocardial infarction and during heart failure (224-226). It is tempting to speculate that the more benign circumstances such as lesser energy depletion and radical oxygen species cause lower transition from apoptosis to necrosis in this setting. In fact, the apoptotic process may remain suspended in chronic heart failure (227).

A number of imaging tracers for myocardial necrosis have been clinically evaluated. Like ^{111}In-GSAO, most tracers exploited membrane disruption, the hallmark of necrosis as a target. ^{111}In-labeled antimyosin antibody was the most widely studied necrosis tracer. Antimyosin antibody imaging has been successfully employed for the detection of myocardial necrosis associated with myocardial infarction (204), myocarditis (204), heart failure (206) and cardiac allograft rejection (206). However, because of long circulation time of the radiolabelled antibody, imaging was not feasible for up to 6–12 hours after administration of the agent. ^{99m}Tc-pyrophosphate on the other hand, showed maximal myocardial uptake at 24 − 72 hours after injection, although necrosis imaging at 3 hours after administration was feasible, maximum myocardial uptake was at 24 − 72 h. Also, this tracer required residual blood flow, which precluded uptake in the infarct center (228). ^{99m}Tc-glucarate can be used to necrotic cells in myocardial infarction (116,213), and has good imaging characteristics but in the setting of myocardial infarction, use is limited to a clinical window of > 9 hours after onset as its target, histone bodies, quickly wash out of the tissue (116). Late gadolinium-enhanced MRI has also been used to assess cardiac cell death; the contrast medium accumulates in necrotic cells through the disrupted membranes. However, its specificity is limited, as gadolinium accumulates in all instances of increased extracellular space

such as cardiac edema, fibrosis, sarcoidosis and amyloidosis (229-231). ^{111}In-GSAO appears to have advantages over the previously evaluated cell death imaging techniques. First, ^{111}In-GSAO requires membrane disruption, the hallmark of necrotic or late-apoptotic cell death, for reaching its intracellular targets. Therefore it does not suffer from the lack of specificity of late-gadolinium enhanced MRI. Moreover, its rapid blood clearance results in feasibility of early imaging of cell death using ^{111}In-GSAO. This gives ^{111}In-GSAO an advantage over ^{99m}Tc-antimyosin and ^{99m}Tc-pyrophosphate. HSP90, the main target of GSAO, functions in complexes. This may allow for targeting over a longer time period, giving ^{111}In-GSAO an edge over ^{99m}Tc-glucarate. However, this has to be evaluated in follow-up studies. SPECT/CT imaging using ^{111}In-GSAO can be used to visualize necrotic cell death in animals with experimental acute myocardial infarction. The uptake in the chronic myocardial infarction model was too low to allow imaging. Because the GSAO uptake reflects membrane permeabilization, and occurs predominantly in annexin A5-positive cells, we propose that secondary necrosis is a dominant mode of cell death in the setting of myocardial ischemia and reperfusion.

4

Chapter 5

Cardioprotection by Minocycline in a Rabbit Model of Acute Myocardial Infarction: Detection of Cell Death by *In Vivo* ^{111}In-GSAO SPECT

Hans J. de Haas[1,2]*, Takayoshi Yamaki[3]*, Nobuhiro Tahara[4], Artiom Petrov[1], Dilbahar Mohar[6], Nezam Haider[1], Jun Zhou[6], Atsuko Tahara[4], Yasuchika Takeishi[3], Hendrikus H. Boersma[2,5], Tiziano Scarabelli[1], Annapoorna Kini[1],H. William Strauss[1], Jagat Narula[1]

1. Zena and Michael A. Wiener Cardiovascular Institute, Icahn School of Medicine at Mount Sinai, New York, New York
2. University of Groningen, University Medical Center Groningen, Department of Nuclear Medicine and Molecular Imaging, The Netherlands
3. Department of Cardiology and Hematology, Fukushima Medical University, Fukushima, Japan;
4. Department of Medicine, Division of Cardio-Vascular Medicine, Kurume University School of Medicine, Kurume, Japan;
5. University of Groningen, University Medical Center Groningen, Department of Clinical Pharmacy and Pharmacology, The Netherlands
6. Division of Cardiology, University of California, Irvine, California

* Authors contributed equally

Abstract

Background: Preclinical studies indicate that minocycline protects against acute myocardial infarction. In these studies, minocycline was administered before ischemia, which can rarely occur in clinical practice. The current study aimed to evaluate cardioprotection by minocycline treatment upon reperfusion.

Methods: To simulate reperfused acute myocardial infarction, rabbits were subjected to myocardial ischemia and reperfusion and received either intravenous minocycline (30mg/kg, n = 8) or saline (n = 8) upon reperfusion.

Cardiac cell death was assessed by *in vivo* single photon emission computed tomography (SPECT) and computed tomography (CT) after injection of ^{111}In-labeled 4-(N-(S-glutathionylacetyl)amino) phenylarsonous acid (^{111}In-GSAO). Thereafter, hearts were explanted for *ex vivo* imaging, γ-counting and histopathological characterization.

Results: Myocardial damage was visualized by SPECT/CT imaging. Quantitative GSAO uptake (expressed as percent injected dose per gram of tissue) in the area at risk was lower in minocycline-treated animals than in saline-treated control animals (0.32 ± 0.13 versus 0.48 ± 0.15, P = 0.04). Terminal deoxynucleotidyl transferase-mediated deoxyuridine triphosphate nick-end labeling (TUNEL) staining confirmed the reduction of cell death in minocycline-treated animals.

Conclusions: This study demonstrates cardioprotection by minocycline in a clinically translatable protocol.

Introduction

In acute myocardial infarction, timely reperfusion therapy can salvage part of the ischemic myocardium. However, a subset of cells suffers from ischemia/reperfusion injury and is lost through accelerated apoptosis or (secondary) necrosis (123). Additional cardioprotective strategies could probably salvage this subset.

Preclinical and clinical studies have demonstrated significant neuroprotection by minocycline therapy after ischemic stroke (183). Similarly, several preclinical studies have shown protective effects of minocycline against myocardial inschemia/reperfusion injury through inhibition of apoptosis (188), inflammation (188,190) and oxidative stress (188), but pre-ischemic administration of minocycline in these studies precludes comparison to clinical practice.

Imaging probes based on 4-(N-(S-glutathionylacetyl)amino) phenylarsonous acid (GSAO), have been used to detect cell death in animal models of tumors (207), traumatic brain injury (209), and myocardial ischemia (232). GSAO consists of the trivalent arsenical molecule phenylarsenoxide connected to a glutathione molecule in the reduced state. The arsenic group binds to dithiol moieties, the presence of which is virtually limited to the intracellular space (210). Of various dithiol-bearing molecules, heat shock protein 90 is GSAO's most abundant target (207). When reporter molecules are connected to the gamma-glutamyl residue of its glutathione pendant, GSAO is membrane impermeable. Thus, to reach their intracellular target molecules, GSAO-based imaging probes exploit sarcolemmal disruption, a hallmark of irreversible cell death.

The present study evaluated the efficacy of acute minocycline administration in a rabbit model of acute myocardial infarction. Minocycline was administered at the time of reperfusion to simulate the clinical situation. For detection of irreversible cardiac damage, ^{111}In-GSAO Single Photon Emission Computed Tomography (SPECT) imaging was performed.

Methods

Induction of acute myocardial infarction in rabbits and ^{111}In-GSAO administration.

The protocol followed the NIH guidelines and was approved by the Institutional Laboratory Animal Care and Use Committee at the University of California, Irvine.

To simulate reperfused acute myocardial infarction, cardiac ischemia and reperfusion were induced in 16 New Zealand White rabbits (2.5 to 3.0 kg, Western Oregon Breeding laboratories, Philomath, OR) according to an established protocol (213,232). Briefly, anesthetized and mechanically ventilated rabbits underwent parasternal thoracotomy. After removal of the pericardium, the lateral branch of the left coronary artery was occluded by tightening a suture through a polyethylene tube. Forty min thereafter, the suture was loosened but left in place to institute reperfusion. Immediately before onset of reperfusion, rabbits randomly received either minocycline hydrochloride (Sigma-Aldrich, St. Louis, MO, 30 mg/kg, IV, n = 8) or 0.9% saline (IV, n = 8). Assuming a correction factor of 30% for the first pass effect, this dosage is consistent with previously published studies, in which intraperitoneal dosages of

~ 50 mg/kg/day were used (188-190). Thirty min after onset of reperfusion, 18.3 ± 2.5 MBq of ^{111}In-GSAO was administered intravenously to all animals. GSAO coupled with diethylenetriaminepentaacetic acid (DTPA) (kind gift of Covidien Imaging Solutions, Hazelwood, Missouri) was labeled with ^{111}In as described in chapter 4 and in (207). Figure 1 depicts the study design.
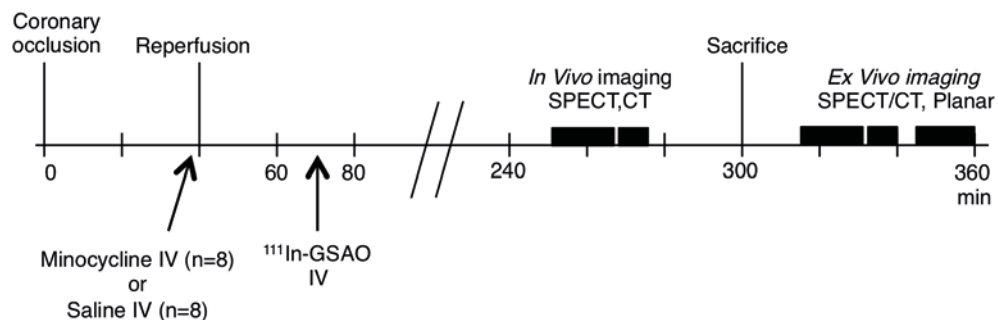

Figure 1. Study design. Schematic diagram illustrating the experimental procedures, the treatment and imaging protocols. ^{111}In-GSAO = ^{111}In-labeled 4-(N-(S-glutathionylacetyl)amino) phenylarsonous acid; CT = computed tomography; IV = intravenous; SPECT = single photon emission computed tomography.

In vivo and *ex vivo* ^{111}In-GSAO imaging

Radionuclide imaging (X-SPECT, Gamma Medica, Inc., Northridge, CA) was performed 3 hours after administration of ^{111}In-GSAO. This is consistent with our previous study (232), which based on ^{111}In-GSAO clearance from the blood ($T_{1/2}\alpha$: 5.3 min, $T_{1/2}\beta$: 9.7 h), undertook imaging 3h after radionuclide administration. SPECT images of the heart were acquired in a 64 × 64 matrix, with 32 stops at 30 seconds per stop. A medium energy parallel-hole collimator was used and a 15% energy window was set for the 247 keV photopeak of [111]In. After the SPECT scan, a Computed Tomography (CT) scan was acquired using an X-ray tube operating at 50 kVp and 0.8 mA. Images were captured for 2.5 seconds per view for 256 views in 360° rotation. SPECT and CT images were transferred to a 256 × 256 matrix and fused. To delineate the ischemic area at risk after imaging, the suture around the left coronary artery was re-tied, the aortic arch was clamped and 1% Evans blue (Sigma-Aldrich, St Louis, MO) solution was injected through a catheter into the ascending aorta.

The animals were sacrificed with an overdose of pentobarbital. *Ex vivo* SPECT/CT imaging of explanted hearts was performed using the same imaging protocol, followed by planar imaging for 15 min using a parallel-hole collimator. Next, hearts were cut into 4 equidistant short-axis slices; slices were photographed and cut into a total of 32 pieces per heart. Each piece was weighed and radiotracer uptake was quantified by γ-counting (Perkin ElmerWallac, Inc., Gaithersburg, MA). To correct for the radioactive decay and permit calculation of the radioactivity in pieces as percent injected dose per gram of tissue (%ID/g), aliquots of the injected dose were counted simultaneously. After γ-counting, the myocardial pieces were formalin-fixed and paraffin-embedded for histopathological characterization.

Myocardial pieces from the area at risk were identified based on lack of Evans Blue staining. Radiotracer uptake in the area at risk and the remote area were calculated in each animal for slices 1-3. Right

ventricular pieces and the basal slice containing tissue damaged by the suture and remote tissue were removed from analyses.

(Immuno)histopathological examinations

Based on Evan's blue staining, cardiac pieces from area at risk and from the remote area were selected from minocycline-treated (n = 6) and saline-treated (n = 3) animals. For each animal, two pieces per region were evaluated per animal and results were averaged.

For morphological evaluation, deparaffinized 4-μm thick sections were stained with Hematoxylin & Eosin, and Masson's trichrome; the rate of apoptosis was evaluated by terminal deoxyribonucleotide transferase TdT-mediated nick-end label (TUNEL) staining using a commercially available kit (TACS, Trevigen, Inc., Gaithersburg, MD) as described previously (49). For quantification of % TUNEL positive area (%area positive), stained tissue sections were observed under appropriate magnification (Zeiss Axivert-200 microscope, Carl Zeiss, Inc., Thornwood, NY), and images were captured with a high resolution digital camera (Axiocam, 1,300 × 1,030 pixels, Carl Zeiss) using Axivision 3.1 software.

Statistical analyses

The sample size was based on a sample size table for two-sided t-tests (233) and the following parameters: effect size (d) of 1.5, significance level (α) of 0.05, power (β) of 0.8. For pairwise comparisons of normally distributed data (expressed as mean ± SD), the Student's T-test was used. For pairwise comparisons of non-normally distributed data (expressed as median (interquartile range)), the Mann-Whitney U test was used. P values < 0.05 were considered significant. All statistical analyses were performed using IBM SPSS Statistics (IBM corporation, Chicago, IL).

5

Results

In vivo and *ex vivo* ¹¹¹In-GSAO imaging

In vivo SPECT/CT with ¹¹¹In-GSAO allowed visualization of irreversible myocardial damage (Figure 2a). Myocardial GSAO uptake was observed in the infarcted apical area in all animals. The area and intensity of GSAO uptake was markedly lower in minocycline-treated animals than in saline-treated animals. *Ex vivo* SPECT/CT (not shown) and *ex vivo* planar (Figure 2b) imaging confirmed the minocycline-induced reduction of intensity and area of uptake.
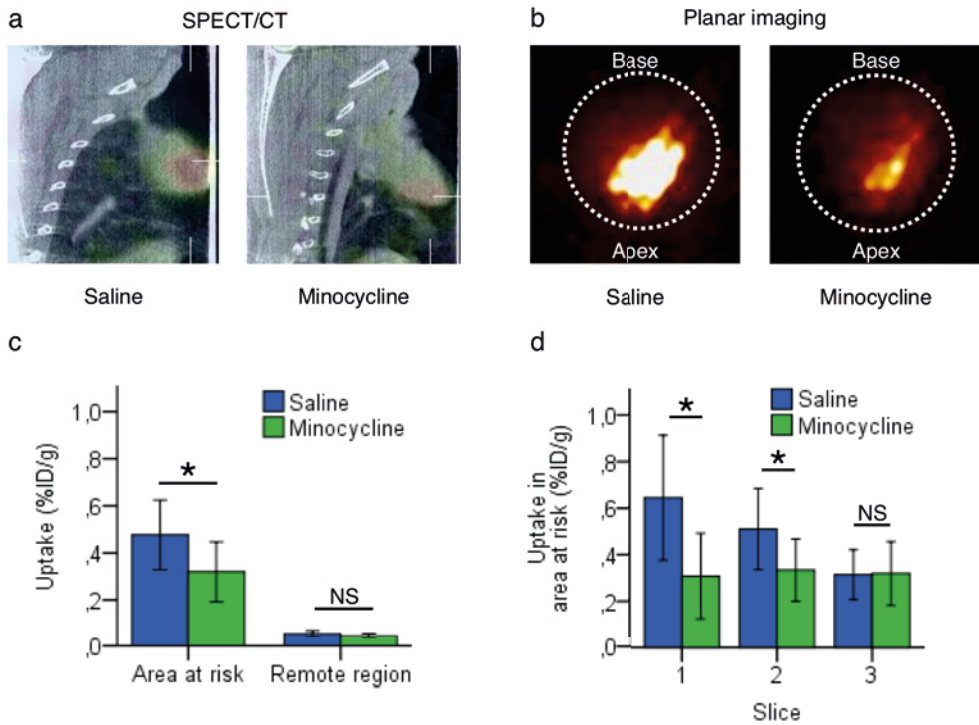
Figure 2. ¹¹¹In-GSAO imaging and quantification, and TUNEL staining. (a) *In vivo* ¹¹¹In-GSAO SPECT/CT images and (b) *ex vivo* planar images reveal lower ¹¹¹In-GSAO uptake in minocycline-treated versus saline-treated animals. (c) Quantification of ¹¹¹In-GSAO uptake confirms lower uptake in area at risk of minocycline-treated animals versus saline-treated animals. Uptake in remote region is similar among minocycline- and saline-treated animals. (d) Quantitative ¹¹¹In-GSAO uptake in area at risk; comparison at heart slice level. In apical slices 1 and slice 2, ¹¹¹In-GSAO uptake is lower in minocycline-treated animals than in saline treated-animals. * = P < 0.05; NS = not statistically significant; %ID/g = percent injected dose.

Quantification of ¹¹¹In-GSAO uptake

Figure 3a shows photographs of heart slices after Evans Blue staining. Generally, slice 1 (apex) contained mainly area at risk, slices 2 and 3 contained a mixture of area at risk and remote tissue. There was no significant difference in size of the area at risk (expressed of percentage of left ventricular weight)

between minocycline-treated and saline-treated animals (32.01 ± 5.89 versus 33.65 ± 5.77, P = 0.58, Figure 3b).
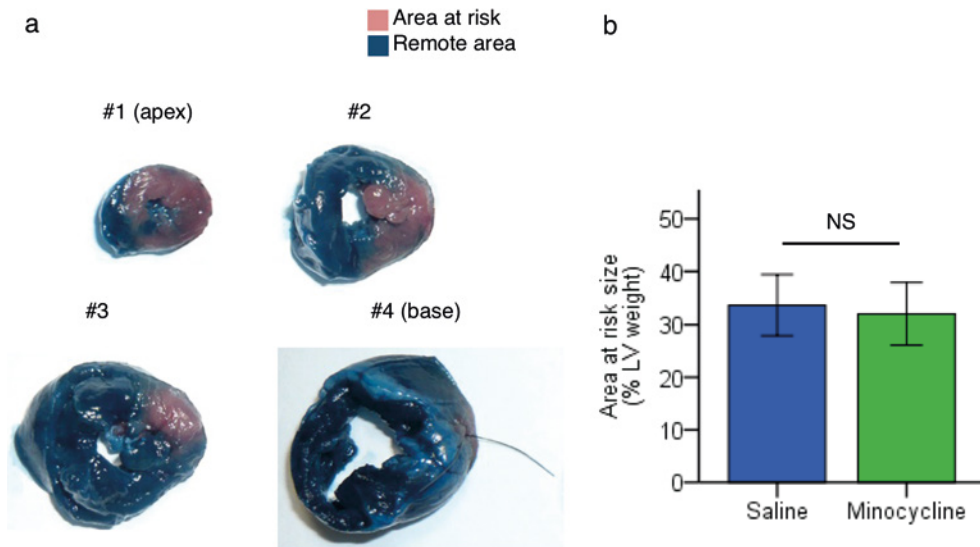
Figure 3. Identification and quantification of area at risk. (a) Short axis slices of Evans blue-stained rabbits hearts. Infarcted myocardium was identified by lack of blue coloration. (b) Quantification of area at risk size in minocycline-treated versus control animals reveals similar area at risk size among minocycline- and saline-treated animals. LV, left ventricle.

Figure 2c shows results of quantification of radiotracer uptake by γ-counting in the area at risk and the remote area. GSAO uptake (expressed as %ID/g) in the area at risk was significantly lower in minocycline-treated animals than in saline-treated animals (0.32 ± 0.13 versus 0.48 ± 0.15, P = 0.04). Uptake in the remote area was similar among minocycline-treated and saline-treated animals (0.05 ± 0.01 versus 0.06 ± 0.01, P = 0.17). Radiotracer uptake in the area at risk was also compared at the heart slice level in minocycline-treated animals versus saline treated animals (Figure 2d). Uptake in the area at risk of the apical slice 1 was markedly lower in minocycline-treated than in saline-treated animals (0.30 ± 0.18 versus 0.64 ± 0.27, P = 0.01). In slice 2, radiotracer uptake in the area at risk was also significantly lower in minocycline-treated than in saline-treated animals (0.33 ± 0.13 versus 0.51 ± 0.17, P = 0.04). Radiotracer uptake in the area at risk of slice 3 was similar among minocycline- and saline-treated animals (0.32 ± 0.14% versus 0.31 ± 0.11%, P = 0.94).

Histopathological and immunohistochemical evaluation of cardiac damage
Figure 4 shows representative examples and quantification of TUNEL staining. In the area at risk, the rate of apoptosis as demonstrated by TUNEL staining (expressed as area percentage of positive staining) was significantly lower in the minocycline group compared with the saline-treated group (0.16 (0.10-0.54) versus 2.47 (1.25-3.59), P = 0.02). In the remote zones, TUNEL positivity was low in both the minocycline-treated as well as in the saline-treated animals (0.03 (0.02-0.05) versus 0.02 (0.02-0.02), P = 0.17).
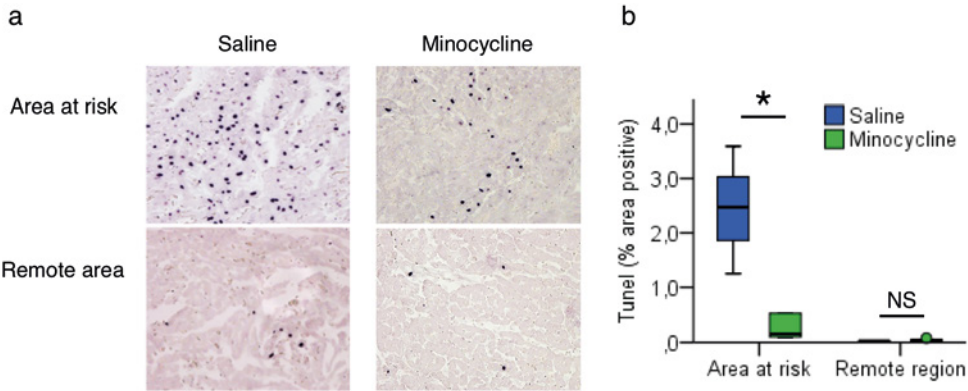
Figure 4. Histopathological characterization of cardiac cell death. (a) Representative examples and (b) quantification of TUNEL staining in area at risk and remote area. The rate of apoptosis in area at risk is lower in minocycline-treated versus saline-treated rabbits. In remote area, rates of apoptosis are similar among minocycline- and saline-treated rabbits. TUNEL = terminal deoxynucleotidyl transferase dUTP nick end labeling.

Similarly, qualitative evaluation of Hematoxylin & Eosin and Masson's trichrome staining revealed that morphological signs of tissue damage including hypereosinophilic myocytes with ground glass character and pyknotic nuclear change in the area at risk were more modest in minocycline-treated than in saline-treated animals (Figure 5). No difference was observed in remote areas.
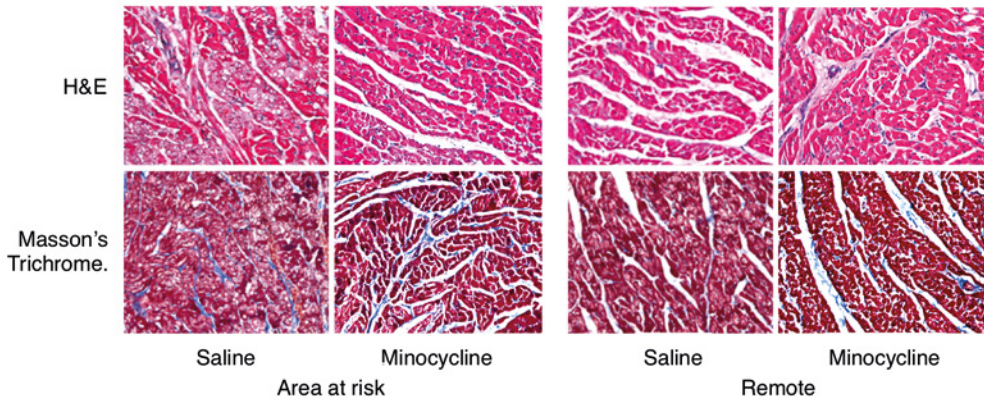
Figure 5. Histopathology. H&E staining, and Masson's trichrome staining in minocycline-treated and saline-treated rabbits with experimental acute myocardial infarction in the area at risk and remote area. In the infarct area, but not in the remote area, morphological signs of myocardial damage are less pronounced in minocycline-treated than in saline-treated rabbits. H&E = hematoxylin & eosin.

Discussion

Here we demonstrate that minocycline markedly reduces cardiac damage in a rabbit model of acute myocardial infarction. To simulate the clinical scenario, minocycline was administered upon reperfusion. For optimal assessment of cardiac damage and efficacy of minocycline, *in vivo* SPECT imaging of cell death using ^{111}In-GSAO was used in addition to immunohistochemistry. In all previous preclinical studies employing animal models of myocardial infarction, minocycline was administered before coronary occlusion.

Over the past twenty years, the most widely studied imaging probe for detection of cell death was ^{99m}Tc-annexin A5 (201). This molecule targets apoptotic cells by binding to the membrane marker phosphatidylserine (PS). As apoptosis is a programmed cell death process that can be halted or reversed, ^{99m}Tc-annexin A5 uptake does not show irreversible cell death (126). Indeed, in a clinical study, the area of ^{99m}Tc-annexin A5 uptake in the acute phase of myocardial infarction exceeded the infarct size by perfusion imaging in a later stage (202). As ^{111}In-GSAO targets irreversibly dead cells, it may be better suited to assess the degree of cell death than ^{99m}Tc-annexin A5.

Several imaging tracers which like GSAO target dead cells through sarcolemmal disruption have been evaluated, including ^{99m}Tc-pyrophosphate, ^{99m}Tc-glucarate and ^{111}In-Antimyosin (228). Most experience has been obtained with ^{111}In-antimyosin, which obtained approval of the United States Food and Drug Association (FDA) for diagnosis of myocardial infarction. However, this probe has been discontinued, mostly because its long circulation half-life, necessitating imaging at long after the injection (228).

Here ^{111}In-GSAO has an advantage over ^{111}In-antimyosin: in the current and previous study (232), we demonstrate feasibility of ^{111}In-GSAO SPECT imaging at three hours after radiotracer administration. Moreover, this suggests that labeling GSAO with radioisotopes with shorter half lives and more favorable imaging characteristics such as ^{99m}Tc may be a viable approach.

The cardioprotective effect of minocycline results from the prevention of cytochrome c release from the mitochondria and direct inhibition of apoptotic signaling cascade (189). We accordingly observed a significant reduction in TUNEL positivity in the area at risk. Cell death of a necrotic phenotype characterized by sarcolemmal disruption often follows initial apoptotic insult (123). Indeed, in our previous study we reported that in hearts of mice receiving fluorescently labeled annexin A5 and GSAO after cardiac ischemia and reperfusion, all GSAO-positive cardiomyocytes were annexin A5-positive (232). Thus reduction of apoptotic signaling likely has contributed to the lower loss of cardiac tissue. Further, direct reductions of oxidative stress (188), release of matrix metalloproteinase 9 (188) and high-mobility group protein 1 may contribute to myocardial salvage (190).

Conclusions

The present study shows that minocycline reduced the extent of myocardial damage in a rabbit model of acute myocardial infarction, as assessed by ^{111}In-labeled GSAO imaging and supported by histopathologic characterization. As opposed to previous studies, a clinically translatable protocol was used, with minocycline administration upon reperfusion. A clinically available and safe antibiotic, minocycline holds strong promise as a cardioprotective agent in acute coronary syndromes. We support initiation of further pre-clinical studies to evaluate its long-term cardioprotective efficacy.

Chapter 6

- **References**
- **List of Abbreviations**
- **Summary, general discussion and future perspectives**
- **Nederlandse samenvatting**
- **List of publications**
- **Acknowledgements**
- **Curriculum vitae**

References

1. Finn AV, Nakano M, Narula J, Kolodgie FD, Virmani R. Concept of vulnerable/unstable plaque. Arterioscler Thromb Vasc Biol 2010 Jul;30(7):1282-1292.
2. Virmani R, Burke AP, Farb A, Kolodgie FD. Pathology of the vulnerable plaque. J Am Coll Cardiol 2006;47(8 Supplement):C13-C18.
3. Arbab-Zadeh A, Nakano M, Virmani R, Fuster V. Acute coronary events. Circulation 2012 Mar 6;125(9):1147-1156.
4. Dweck MR, Aikawa E, Newby DE, Tarkin J, Rudd J, Narula J, et al. Non-Invasive Molecular Imaging of Disease Activity in Atherosclerosis. 2016.
5. Notghi A, Low CS. Myocardial perfusion scintigraphy: past, present and future. Br J Radiol 2014.
6. Marcassa C, Bax JJ, Bengel F, Hesse B, Petersen CL, Reyes E, et al. Clinical value, cost-effectiveness, and safety of myocardial perfusion scintigraphy: a position statement. Eur Heart J 2008 Feb;29(4):557-563.
7. Hansen CL, Goldstein RA, Akinboboye OO, Berman DS, Botvinick EH, Churchwell KB, et al. Myocardial perfusion and function: single photon emission computed tomography. Journal of Nuclear Cardiology 2007;14(6):e39-e60.
8. Dorbala S, Di Carli MF. Cardiac PET perfusion: prognosis, risk stratification, and clinical management. Semin Nucl Med 2014 Sep;44(5):344-357.
9. Maddahi J, Packard RR. Cardiac PET perfusion tracers: current status and future directions. Semin Nucl Med 2014 Sep;44(5):333-343.
10. Jin KN, De Cecco CN, Caruso D, Tesche C, Spandorfer A, Varga-Szemes A, et al. Myocardial perfusion imaging with dual energy CT. Eur J Radiol 2016;85(10):1914-1921.
11. Williams M, Newby D. CT myocardial perfusion imaging: current status and future directions. Clin Radiol 2016;71(8):739-749.
12. Hendel RC, Friedrich MG, Schulz-Menger J, Zemmrich C, Bengel F, Berman DS, et al. CMR First-Pass Perfusion for Suspected Inducible Myocardial Ischemia. JACC: Cardiovascular Imaging 2016;9(11):1338-1348.
13. Marano R, Natale L, Chiribiri A, Pirro F, Silvestri V, Coppola G, et al. Cardiac MR perfusion imaging: where we are. Radiol Med 2015;120(2):190-205.
14. Libby P, Ridker PM, Maseri A. Inflammation and atherosclerosis. Circulation 2002 Mar 5;105(9):1135-1143.
15. (Libby P. The molecular mechanisms of the thrombotic complications of atherosclerosis. J Intern Med 2008 May;263(5):517-527.
16. Kelloff GJ, Hoffman JM, Johnson B, Scher HI, Siegel BA, Cheng EY, et al. Progress and promise of FDG-PET imaging for cancer patient management and oncologic drug development. Clin Cancer Res 2005 Apr 15;11(8):2785-2808.
17. Ben-Haim S, Ell P. 18F-FDG PET and PET/CT in the evaluation of cancer treatment response. J Nucl Med 2009 Jan;50(1):88-99.
18. Love C, Tomas MB, Tronco GG, Palestro CJ. FDG PET of Infection and Inflammation 1. Radiographics 2005;25(5):1357-1368.
19. Allman KC. Noninvasive assessment myocardial viability: current status and future directions. Journal of Nuclear Cardiology 2013;20(4):618-637.
20. Defawe OD, Hustinx R, Defraigne JO, Limet R, Sakalihasan N. Distribution of F-18 fluorodeoxyglucose (F-18 FDG) in abdominal aortic aneurysm: high accumulation in macrophages seen on PET imaging and immunohistology. Clin Nucl Med 2005 May;30(5):340-341.
21. Walter MA, Melzer RA, Schindler C, Müller-Brand J, Tyndall A, Nitzsche EU. The value of [18F] FDG-PET in the diagnosis of large-vessel vasculitis and the assessment of activity and extent of disease. European journal of nuclear medicine and molecular imaging 2005;32(6):674-681.
22. Yun M, Jang S, Cucchiara A, Newberg AB, Alavi A. 18F FDG uptake in the large arteries: a correlation study with

the atherogenic risk factors. Semin Nucl Med 2002 Jan;32(1):70-76.

23. Figueroa AL, Abdelbaky A, Truong QA, Corsini E, MacNabb MH, Lavender ZR, et al. Measurement of arterial activity on routine FDG PET/CT images improves prediction of risk of future CV events. JACC: Cardiovascular Imaging 2013;6(12):1250-1259.

24. Rominger A, Saam T, Wolpers S, Cyran CC, Schmidt M, Foerster S, et al. 18F-FDG PET/CT identifies patients at risk for future vascular events in an otherwise asymptomatic cohort with neoplastic disease. J Nucl Med 2009 Oct;50(10):1611-1620.

25. Marnane M, Merwick A, Sheehan OC, Hannon N, Foran P, Grant T, et al. Carotid plaque inflammation on 18F-fluorodeoxyglucose positron emission tomography predicts early stroke recurrence. Ann Neurol 2012;71(5):709-718.

26. Tahara N, Kai H, Ishibashi M, Nakaura H, Kaida H, Baba K, et al. Simvastatin attenuates plaque inflammation: evaluation by fluorodeoxyglucose positron emission tomography. J Am Coll Cardiol 2006;48(9):1825-1831.

27. Ogawa M, Magata Y, Kato T, Hatano K, Ishino S, Mukai T, et al. Application of 18F-FDG PET for monitoring the therapeutic effect of antiinflammatory drugs on stabilization of vulnerable atherosclerotic plaques. J Nucl Med 2006 Nov;47(11):1845-1850.

28. Mizoguchi M, Tahara N, Tahara A, Nitta Y, Kodama N, Oba T, et al. Pioglitazone attenuates atherosclerotic plaque inflammation in patients with impaired glucose tolerance or diabetes: a prospective, randomized, comparator-controlled study using serial FDG PET/CT imaging study of carotid artery and ascending aorta. JACC: Cardiovascular Imaging 2011;4(10):1110-1118.

29. Nitta Y, Tahara N, Tahara A, Honda A, Kodama N, Mizoguchi M, et al. Pioglitazone decreases coronary artery inflammation in impaired glucose tolerance and diabetes mellitus: evaluation by FDG-PET/CT imaging. JACC: Cardiovascular Imaging 2013;6(11):1172-1182.

30. Nissen SE, Nicholls SJ, Sipahi I, Libby P, Raichlen JS, Ballantyne CM, et al. Effect of very high-intensity statin therapy on regression of coronary atherosclerosis: the ASTEROID trial. JAMA 2006;295(13):1556-1565.

31. Amarenco P, Labreuche J, Lavallee P, Touboul PJ. Statins in stroke prevention and carotid atherosclerosis: systematic review and up-to-date meta-analysis. Stroke 2004 Dec;35(12):2902-2909.

32. Tawakol A, Singh P, Rudd JH, Soffer J, Cai G, Vucic E, et al. Effect of Treatment for 12 Weeks With Rilapladib, a Lipoprotein-Associated Phospholipase A2 Inhibitor, on Arterial Inflammation as Assessed With F-Fluorodeoxyglucose-Positron Emission Tomography Imaging. J Am Coll Cardiol 2014;63(1):86-88.

33. Fayad ZA, Mani V, Woodward M, Kallend D, Abt M, Burgess T, et al. Safety and efficacy of dalcetrapib on atherosclerotic disease using novel non-invasive multimodality imaging (dal-PLAQUE): a randomised clinical trial. The Lancet 2011;378(9802):1547-1559.

34. Stability Investigators. Darapladib for preventing ischemic events in stable coronary heart disease. N Engl J Med 2014;2014(370):1702-1711.

35. Schwartz GG, Olsson AG, Abt M, Ballantyne CM, Barter PJ, Brumm J, et al. Effects of dalcetrapib in patients with a recent acute coronary syndrome. N Engl J Med 2012;367(22):2089-2099.

36. Dweck MR, Jenkins WS, Vesey AT, Pringle MA, Chin CW, Malley TS, et al. 18F-sodium fluoride uptake is a marker of active calcification and disease progression in patients with aortic stenosis. Circ Cardiovasc Imaging 2014 Mar;7(2):371-378.

37. Dalm VA, van Hagen PM, van Koetsveld PM, Achilefu S, Houtsmuller AB, Pols DH, et al. Expression of somatostatin, cortistatin, and somatostatin receptors in human monocytes, macrophages, and dendritic cells. Am J Physiol Endocrinol Metab 2003 Aug;285(2):E344-53.

38. Rominger A, Saam T, Vogl E, Ubleis C, la Fougere C, Forster S, et al. In vivo imaging of macrophage activity in the coronary arteries using 68Ga-DOTATATE PET/CT: correlation with coronary calcium burden and risk factors. J Nucl Med 2010 Feb;51(2):193-197.

39. Tarkin JM, Joshi FR, Evans NR, Chowdhury MM, Figg NL, Shah AV, et al. Detection of Atherosclerotic Inflammation

6

by 68Ga-DOTATATE PET Compared to [18F] FDG PET Imaging. J Am Coll Cardiol 2017;69(14):1774-1791.

40. Kooi ME, Cappendijk VC, Cleutjens KB, Kessels AG, Kitslaar PJ, Borgers M, et al. Accumulation of ultrasmall superparamagnetic particles of iron oxide in human atherosclerotic plaques can be detected by in vivo magnetic resonance imaging. Circulation 2003 May 20;107(19):2453-2458.

41. Trivedi RA, U-King-Im JM, Graves MJ, Cross JJ, Horsley J, Goddard MJ, et al. In vivo detection of macrophages in human carotid atheroma: temporal dependence of ultrasmall superparamagnetic particles of iron oxide-enhanced MRI. Stroke 2004 Jul;35(7):1631-1635.

42. Trivedi RA, Mallawarachi C, U-King-Im JM, Graves MJ, Horsley J, Goddard MJ, et al. Identifying inflamed carotid plaques using in vivo USPIO-enhanced MR imaging to label plaque macrophages. Arterioscler Thromb Vasc Biol 2006 Jul;26(7):1601-1606.

43. Tang TY, Howarth SP, Miller SR, Graves MJ, Patterson AJ, Jean-Marie U, et al. The ATHEROMA (Atorvastatin Therapy: Effects on Reduction of Macrophage Activity) Study: evaluation using ultrasmall superparamagnetic iron oxide-enhanced magnetic resonance imaging in carotid disease. J Am Coll Cardiol 2009;53(22):2039-2050.

44. Okubo R, Nakanishi R, Toda M, Saito D, Watanabe I, Yabe T, et al. Pericoronary adipose tissue ratio is a stronger associated factor of plaque vulnerability than epicardial adipose tissue on coronary computed tomography angiography. Heart Vessels 2017 Jul;32(7):813-822.

45. Antonopoulos AS, Sanna F, Sabharwal N, Thomas S, Oikonomou EK, Herdman L, et al. Detecting human coronary inflammation by imaging perivascular fat. Sci Transl Med 2017 Jul 12;9(398):10.1126/scitranslmed.aal2658.

46. Kolodgie FD, Petrov A, Virmani R, Narula N, Verjans JW, Weber DK, et al. Targeting of apoptotic macrophages and experimental atheroma with radiolabeled annexin V: a technique with potential for noninvasive imaging of vulnerable plaque. Circulation 2003 Dec 23;108(25):3134-3139.

47. Johnson LL, Schofield L, Donahay T, Narula N, Narula J. 99mTc-annexin V imaging for in vivo detection of atherosclerotic lesions in porcine coronary arteries. J Nucl Med 2005 Jul;46(7):1186-1193.

48. Kietselaer BL, Reutelingsperger CP, Heidendal GA, Daemen MJ, Mess WH, Hofstra L, et al. Noninvasive detection of plaque instability with use of radiolabeled annexin A5 in patients with carotid-artery atherosclerosis. N Engl J Med 2004;350(14):1472-1473.

49. Sarai M, Hartung D, Petrov A, Zhou J, Narula N, Hofstra L, et al. Broad and specific caspase inhibitor-induced acute repression of apoptosis in atherosclerotic lesions evaluated by radiolabeled annexin A5 imaging. J Am Coll Cardiol 2007;50(24):2305-2312.

50. Hartung D, Sarai M, Petrov A, Kolodgie F, Narula N, Verjans J, et al. Resolution of apoptosis in atherosclerotic plaque by dietary modification and statin therapy. J Nucl Med 2005 Dec;46(12):2051-2056.

51. Fujimoto S, Hartung D, Ohshima S, Edwards DS, Zhou J, Yalamanchili P, et al. Molecular imaging of matrix metalloproteinase in atherosclerotic lesions: resolution with dietary modification and statin therapy. J Am Coll Cardiol 2008 Dec 2;52(23):1847-1857.

52. Ohshima S, Petrov A, Fujimoto S, Zhou J, Azure M, Edwards DS, et al. Molecular imaging of matrix metalloproteinase expression in atherosclerotic plaques of mice deficient in apolipoprotein e or low-density-lipoprotein receptor. J Nucl Med 2009 Apr;50(4):612-617.

53. Ohshima S, Fujimoto S, Petrov A, Nakagami H, Haider N, Zhou J, et al. Effect of an antimicrobial agent on atherosclerotic plaques: assessment of metalloproteinase activity by molecular imaging. J Am Coll Cardiol 2010 Mar 23;55(12):1240-1249.

54. Razavian M, Nie L, Challa A, Zhang J, Golestani R, Jung JJ, et al. Lipid lowering and imaging protease activation in atherosclerosis. J Nucl Cardiol 2014 Apr;21(2):319-328.

55. Haider N, Hartung D, Fujimoto S, Petrov A, Kolodgie FD, Virmani R, et al. Dual molecular imaging for targeting metalloproteinase activity and apoptosis in atherosclerosis: molecular imaging facilitates understanding of pathogenesis. J Nucl Cardiol 2009 Sep-Oct;16(5):753-762.

56. Tekabe Y, Li Q, Luma J, Weisenberger D, Sedlar M, Harja E, et al. Noninvasive monitoring the biology of

atherosclerotic plaque development with radiolabeled annexin V and matrix metalloproteinase inhibitor in spontaneous atherosclerotic mice. J Nucl Cardiol 2010 Dec;17(6):1073-1081.

57. Golestani R, Razavian M, Nie L, Zhang J, Jung JJ, Ye Y, et al. Imaging vessel wall biology to predict outcome in abdominal aortic aneurysm. Circ Cardiovasc Imaging 2014 Dec 30;8(1):10.1161/CIRCIMAGING.114.002471. Print 2015 Jan.

58. Su H, Spinale FG, Dobrucki LW, Song J, Hua J, Sweterlitsch S, et al. Noninvasive targeted imaging of matrix metalloproteinase activation in a murine model of postinfarction remodeling. Circulation 2005 Nov 15;112(20):3157-3167.

59. Jung JJ, Razavian M, Challa AA, Nie L, Golestani R, Zhang J, et al. Multimodality and molecular imaging of matrix metalloproteinase activation in calcific aortic valve disease. J Nucl Med 2015 Jun;56(6):933-938.

60. Golestani R, Toczek J, Razavian M, Zhang J, Ye Y, Lee CG, et al. Matrix metalloproteinase-targeted imaging of lung inflammation and remodeling. Journal of Nuclear Medicine 2016;57(supplement 2):488-488.

61. Lancelot E, Amirbekian V, Brigger I, Raynaud JS, Ballet S, David C, et al. Evaluation of matrix metalloproteinases in atherosclerosis using a novel noninvasive imaging approach. Arterioscler Thromb Vasc Biol 2008 Mar;28(3):425-432.

62. Amirbekian V, Aguinaldo JG, Amirbekian S, Hyafil F, Vucic E, Sirol M, et al. Atherosclerosis and matrix metalloproteinases: experimental molecular MR imaging in vivo. Radiology 2009 May;251(2):429-438.

63. Hyafil F, Vucic E, Cornily JC, Sharma R, Amirbekian V, Blackwell F, et al. Monitoring of arterial wall remodelling in atherosclerotic rabbits with a magnetic resonance imaging contrast agent binding to matrix metalloproteinases. Eur Heart J 2011 Jun;32(12):1561-1571.

64. Ouimet T, Lancelot E, Hyafil F, Rienzo M, Deux F, Lemaitre M, et al. Molecular and cellular targets of the MRI contrast agent P947 for atherosclerosis imaging. Mol Pharm 2012 Apr 2;9(4):850-861.

65. Deguchi JO, Aikawa M, Tung CH, Aikawa E, Kim DE, Ntziachristos V, et al. Inflammation in atherosclerosis: visualizing matrix metalloproteinase action in macrophages in vivo. Circulation 2006 Jul 4;114(1):55-62.

66. Chang K, Francis SA, Aikawa E, Figueiredo JL, Kohler RH, McCarthy JR, et al. Pioglitazone suppresses inflammation in vivo in murine carotid atherosclerosis: novel detection by dual-target fluorescence molecular imaging. Arterioscler Thromb Vasc Biol 2010 Oct;30(10):1933-1939.

67. Irkle A, Vesey AT, Lewis DY, Skepper JN, Bird JL, Dweck MR, et al. Identifying active vascular microcalcification by (18)F-sodium fluoride positron emission tomography. Nat Commun 2015 Jul 7;6:7495.

68. Alexopoulos N, Raggi P. Calcification in atherosclerosis. Nature Reviews Cardiology 2009;6(11):681-688.

69. Clarke MC, Littlewood TD, Figg N, Maguire JJ, Davenport AP, Goddard M, et al. Chronic apoptosis of vascular smooth muscle cells accelerates atherosclerosis and promotes calcification and medial degeneration. Circ Res 2008 Jun 20;102(12):1529-1538.

70. Derlin T, Wisotzki C, Richter U, Apostolova I, Bannas P, Weber C, et al. In vivo imaging of mineral deposition in carotid plaque using 18F-sodium fluoride PET/CT: correlation with atherogenic risk factors. J Nucl Med 2011 Mar;52(3):362-368.

71. Beheshti M, Saboury B, Mehta NN, Torigian DA, Werner T, Mohler E, et al. Detection and global quantification of cardiovascular molecular calcification by fluoro18-fluoride positron emission tomography/computed tomography--a novel concept. Hell J Nucl Med 2011 May-Aug;14(2):114-120.

72. Joshi NV, Vesey AT, Williams MC, Shah AS, Calvert PA, Craighead FH, et al. 18F-fluoride positron emission tomography for identification of ruptured and high-risk coronary atherosclerotic plaques: a prospective clinical trial. Lancet 2014 Feb 22;383(9918):705-713.

73. Quirce R, Martinez-Rodriguez I, Banzo I, Jimenez-Bonilla J, Martinez-Amador N, Ibanez-Bravo S, et al. New insight of functional molecular imaging into the atheroma biology: 18F-NaF and 18F-FDG in symptomatic and asymptomatic carotid plaques after recent CVA. Preliminary results. Clin Physiol Funct Imaging 2016 Nov;36(6):499-503.

6

74. Weis SM, Cheresh DA. Tumor angiogenesis: molecular pathways and therapeutic targets. Nat Med 2011;17(11):1359-1370.

75. Wilder RL. Integrin alpha V beta 3 as a target for treatment of rheumatoid arthritis and related rheumatic diseases. Ann Rheum Dis 2002 Nov;61 Suppl 2:ii96-9.

76. Bennett J, Berger B, Billings P. The structure and function of platelet integrins. Journal of Thrombosis and Haemostasis 2009;7(s1):200-205.

77. van den Borne SW, Diez J, Blankesteijn WM, Verjans J, Hofstra L, Narula J. Myocardial remodeling after infarction: the role of myofibroblasts. Nat Rev Cardiol 2010 Jan;7(1):30-37.

78. Saraste A, Laitinen I, Weidl E, Wildgruber M, Weber AW, Nekolla SG, et al. Diet intervention reduces uptake of alphavbeta3 integrin-targeted PET tracer 18F-galacto-RGD in mouse atherosclerotic plaques. J Nucl Cardiol 2012 Aug;19(4):775-784.

79. Laitinen I, Saraste A, Weidl E, Poethko T, Weber AW, Nekolla SG, et al. Evaluation of alphavbeta3 integrin-targeted positron emission tomography tracer 18F-galacto-RGD for imaging of vascular inflammation in atherosclerotic mice. Circ Cardiovasc Imaging 2009 Jul;2(4):331-338.

80. Beer AJ, Pelisek J, Heider P, Saraste A, Reeps C, Metz S, et al. PET/CT imaging of integrin alphavbeta3 expression in human carotid atherosclerosis. JACC Cardiovasc Imaging 2014 Feb;7(2):178-187.

81. Golestani R, Mirfeizi L, Zeebregts CJ, Westra J, de Haas HJ, Glaudemans AW, et al. Feasibility of [18F]-RGD for ex vivo imaging of atherosclerosis in detection of alphavbeta3 integrin expression. J Nucl Cardiol 2015 Dec;22(6):1179-1186.

82. Paeng JC, Lee Y, Lee JS, Jeong JM, Kim K, Chung J, et al. Feasibility and kinetic characteristics of 68Ga-NOTA-RGD PET for in vivo atherosclerosis imaging. Ann Nucl Med 2013;27(9):847-854.

83. Kitagawa T, Kosuge H, Uchida M, Iida Y, Dalman RL, Douglas T, et al. RGD targeting of human ferritin iron oxide nanoparticles enhances in vivo MRI of vascular inflammation and angiogenesis in experimental carotid disease and abdominal aortic aneurysm. J Magn Reson Imaging 2016 Sep 30.

84. Burtea C, Laurent S, Murariu O, Rattat D, Toubeau G, Verbruggen A, et al. Molecular imaging of alpha v beta3 integrin expression in atherosclerotic plaques with a mimetic of RGD peptide grafted to Gd-DTPA. Cardiovasc Res 2008 Apr 1;78(1):148-157.

85. Yoo JS, Lee J, Jung JH, Moon BS, Kim S, Lee BC, et al. SPECT/CT Imaging of High-Risk Atherosclerotic Plaques using Integrin-Binding RGD Dimer Peptides. Sci Rep 2015 Jun 30;5:11752.

86. Yao Y, Jiang Y, Sheng Z, Zhang Y, An Y, Yan F, et al. Analysis of in situ and ex vivo alphaVbeta3 integrin expression during experimental carotid atherogenesis. Int J Nanomedicine 2012;7:641-649.

87. Waldeck J, Hager F, Holtke C, Lanckohr C, von Wallbrunn A, Torsello G, et al. Fluorescence reflectance imaging of macrophage-rich atherosclerotic plaques using an alphavbeta3 integrin-targeted fluorochrome. J Nucl Med 2008 Nov;49(11):1845-1851.

88. Knight LC, Maurer AH, Robbins PS, Malmud LS, Budzynski AZ. Fragment E1 labeled with I-123 in the detection of venous thrombosis. Radiology 1985 Aug;156(2):509-514.

89. Rosenthall L, Leclerc J. A new thrombus imaging agent. Human recombinant fibrin binding domain labeled with In-111. Clin Nucl Med 1995 May;20(5):398-402.

90. Andia ME, Saha P, Jenkins J, Modarai B, Wiethoff AJ, Phinikaridou A, et al. Fibrin-targeted magnetic resonance imaging allows in vivo quantification of thrombus fibrin content and identifies thrombi amenable for thrombolysis. Arterioscler Thromb Vasc Biol 2014 Jun;34(6):1193-1198.

91. Stracke CP, Katoh M, Wiethoff AJ, Parsons EC, Spangenberg P, Spuntrup E. Molecular MRI of cerebral venous sinus thrombosis using a new fibrin-specific MR contrast agent. Stroke 2007 May;38(5):1476-1481.

92. Uppal R, Ay I, Dai G, Kim YR, Sorensen AG, Caravan P. Molecular MRI of intracranial thrombus in a rat ischemic stroke model. Stroke 2010 Jun;41(6):1271-1277.

93. Katoh M, Haage P, Wiethoff AJ, Gunther RW, Bucker A, Tacke J, et al. Molecular magnetic resonance imaging

of deep vein thrombosis using a fibrin-targeted contrast agent: a feasibility study. Invest Radiol 2009 Mar;44(3):146-150.

94. Spuentrup E, Fausten B, Kinzel S, Wiethoff AJ, Botnar RM, Graham PB, et al. Molecular magnetic resonance imaging of atrial clots in a swine model. Circulation 2005 Jul 19;112(3):396-399.

95. Botnar RM, Buecker A, Wiethoff AJ, Parsons EC,Jr, Katoh M, Katsimaglis G, et al. In vivo magnetic resonance imaging of coronary thrombosis using a fibrin-binding molecular magnetic resonance contrast agent. Circulation 2004 Sep 14;110(11):1463-1466.

96. Spuentrup E, Botnar RM, Wiethoff AJ, Ibrahim T, Kelle S, Katoh M, et al. MR imaging of thrombi using EP-2104R, a fibrin-specific contrast agent: initial results in patients. Eur Radiol 2008 Sep;18(9):1995-2005.

97. Starmans LW, van Duijnhoven SM, Rossin R, Berben M, Aime S, Daemen MJ, et al. Evaluation of 111In-labeled EPep and FibPep as tracers for fibrin SPECT imaging. Mol Pharm 2013 Nov 4;10(11):4309-4321.

98. Starmans LW, van Duijnhoven SM, Rossin R, Aime S, Daemen MJ, Nicolay K, et al. SPECT imaging of fibrin using fibrin-binding peptides. Contrast Media Mol Imaging 2013 May-Jun;8(3):229-237.

99. Ay I, Blasi F, Rietz TA, Rotile NJ, Kura S, Brownell AL, et al. In Vivo Molecular Imaging of Thrombosis and Thrombolysis Using a Fibrin-binding Positron Emission Tomography Probe. Circ Cardiovasc Imaging 2014 Apr 28.

100. Jaffer FA, Tung CH, Gerszten RE, Weissleder R. In vivo imaging of thrombin activity in experimental thrombi with thrombin-sensitive near-infrared molecular probe. Arterioscler Thromb Vasc Biol 2002 Nov 1;22(11):1929-1935.

101. Olson ES, Whitney MA, Friedman B, Aguilera TA, Crisp JL, Baik FM, et al. In vivo fluorescence imaging of atherosclerotic plaques with activatable cell-penetrating peptides targeting thrombin activity. Integr Biol (Camb) 2012 Jun;4(6):595-605.

102. Kim DE, Kim JY, Nahrendorf M, Lee SK, Ryu JH, Kim K, et al. Direct thrombus imaging as a means to control the variability of mouse embolic infarct models: the role of optical molecular imaging. Stroke 2011 Dec;42(12):3566-3573.

103. Jaffer FA, Tung CH, Wykrzykowska JJ, Ho NH, Houng AK, Reed GL, et al. Molecular imaging of factor XIIIa activity in thrombosis using a novel, near-infrared fluorescent contrast agent that covalently links to thrombi. Circulation 2004 Jul 13;110(2):170-176.

104. Alonso A, Della Martina A, Stroick M, Fatar M, Griebe M, Pochon S, et al. Molecular imaging of human thrombus with novel abciximab immunobubbles and ultrasound. Stroke 2007 May;38(5):1508-1514.

105. Wang X, Hagemeyer CE, Hohmann JD, Leitner E, Armstrong PC, Jia F, et al. Novel single-chain antibody-targeted microbubbles for molecular ultrasound imaging of thrombosis: validation of a unique noninvasive method for rapid and sensitive detection of thrombi and monitoring of success or failure of thrombolysis in mice. Circulation 2012 Jun 26;125(25):3117-3126.

106. Knight LC, Baidoo KE, Romano JE, Gabriel JL, Maurer AH. Imaging pulmonary emboli and deep venous thrombi with 99mTc-bitistatin, a platelet-binding polypeptide from viper venom. J Nucl Med 2000 Jun;41(6):1056-1064.

107. Sakuma T, Sklenar J, Leong-Poi H, Goodman NC, Glover DK, Kaul S. Molecular imaging identifies regions with microthromboemboli during primary angioplasty in acute coronary thrombosis. J Nucl Med 2004 Jul;45(7):1194-1200.

108. Klink A, Lancelot E, Ballet S, Vucic E, Fabre JE, Gonzalez W, et al. Magnetic resonance molecular imaging of thrombosis in an arachidonic acid mouse model using an activated platelet targeted probe. Arterioscler Thromb Vasc Biol 2010 Mar;30(3):403-410.

109. von Elverfeldt D, von zur Muhlen C, Wiens K, Neudorfer I, Zirlik A, Meissner M, et al. In vivo detection of activated platelets allows characterizing rupture of atherosclerotic plaques with molecular magnetic resonance imaging in mice. PLoS One 2012;7(9):e45008.

110. White HD, Chew DP. Acute myocardial infarction. Lancet 2008 Aug 16;372(9638):570-584.

6

111. Yellon DM, Hausenloy DJ. Myocardial reperfusion injury. N Engl J Med 2007;357(11):1121-1135.

112. Yasuda T, Palacios IF, Dec GW, Fallon JT, Gold HK, Leinbach RC, et al. Indium 111-monoclonal antimyosin antibody imaging in the diagnosis of acute myocarditis. Circulation 1987 Aug;76(2):306-311.

113. Frist W, Yasuda T, Segall G, Khaw BA, Strauss HW, Gold H, et al. Noninvasive detection of human cardiac transplant rejection with indium-111 antimyosin (Fab) imaging. Circulation 1987 Nov;76(5 Pt 2):V81-5.

114. Estorch M, Carrio I, Berna L, Martinez-Duncker C, Alonso C, Germa JR, et al. Indium-111-antimyosin scintigraphy after doxorubicin therapy in patients with advanced breast cancer. J Nucl Med 1990 Dec;31(12):1965-1969.

115. Matsumori A, Yamada T, Tamaki N, Watanabe Y, Yonekura Y, Endo K, et al. Prognostic significance of indium-111 antimyosin antibody uptake in patients with dilated and hypertrophic cardiomyopathy. Int J Cardiol 1991;32(1):75-81.

116. Mariani G, Villa G, Rossettin PF, Spallarossa P, Bezante GP, Brunelli C, et al. Detection of Acute Myocardial Infarction by^ 9^ 9^ mTc-Labeled D-Glucaric Acid Imaging in Patients with Acute Chest Pain. Journal of Nuclear Medicine 1999;40:1832-1839.

117. Willerson JT, Parkey RW, Bonte FJ, Meyer SL, Stokely EM. Acute subendocardial myocardial infarction in patients. Its detection by Technetium 99-m stannous pyrophosphate myocardial scintigrams. Circulation 1975 Mar;51(3):436-441.

118. Dumont EA, Hofstra L, van Heerde WL, van den Eijnde S, Doevendans PA, DeMuinck E, et al. Cardiomyocyte death induced by myocardial ischemia and reperfusion: measurement with recombinant human annexin-V in a mouse model. Circulation 2000 Sep 26;102(13):1564-1568.

119. Dumont E, Reutelingsperger C, Smits J, Daemen M, Doevendans P, Wellens H, et al. Real-time imaging of apoptotic cell-membrane changes at the single-cell level in the beating murine heart. Nat Med 2001;7(12):1352-1355.

120. Blankenberg F, Strauss HW. Non-invasive diagnosis of acute heart-or lung-transplant rejection using radiolabeled annexin V. Pediatr Radiol 1999;29(5):299-305.

121. Hofstra L, Liem H, Dumont EA, Boersma HH, van Heerde WL, Doevendans PA, et al. Visualisation of cell death in vivo in patients with acute myocardial infarction. The Lancet 2000;356(9225):209-212.

122. Kietselaer BL, Reutelingsperger CP, Boersma HH, Heidendal GA, Liem IH, Crijns HJ, et al. Noninvasive detection of programmed cell loss with 99mTc-labeled annexin A5 in heart failure. J Nucl Med 2007 Apr;48(4):562-567.

123. Narula J, Strauss HW. Invited commentary: P.S.* I love you: implications of phosphatidyl serine (PS) reversal in acute ischemic syndromes. J Nucl Med 2003 Mar;44(3):397-399.

124. Sarda-Mantel L, Hervatin F, Michel J, Louedec L, Martet G, Rouzet F, et al. Myocardial uptake of 99mTc-annexin-V and 111In-antimyosin-antibodies after ischemia-reperfusion in rats. European journal of nuclear medicine and molecular imaging 2008;35(1):158-165.

125. Doue T, Ohtsuki K, Ogawa K, Ueda M, Azuma A, Saji H, et al. Cardioprotective effects of erythropoietin in rats subjected to ischemia-reperfusion injury: assessment of infarct size with 99mTc-annexin V. J Nucl Med 2008 Oct;49(10):1694-1700.

126. Kenis H, Zandbergen HR, Hofstra L, Petrov AD, Dumont EA, Blankenberg FD, et al. Annexin A5 uptake in ischemic myocardium: demonstration of reversible phosphatidylserine externalization and feasibility of radionuclide imaging. J Nucl Med 2010 Feb;51(2):259-267.

127. Salerno M, Janardhanan R, Jiji RS, Brooks J, Adenaw N, Mehta B, et al. Comparison of methods for determining the partition coefficient of gadolinium in the myocardium using T1 mapping. Journal of Magnetic Resonance Imaging 2013;38(1):217-224.

128. Polasek M, Fuchs BC, Uppal R, Schühle DT, Alford JK, Loving GS, et al. Molecular MR imaging of liver fibrosis: a feasibility study using rat and mouse models. J Hepatol 2012;57(3):549-555.

129. Caravan P, Yang Y, Zachariah R, Schmitt A, Mino-Kenudson M, Chen HH, et al. Molecular magnetic resonance imaging of pulmonary fibrosis in mice. American journal of respiratory cell and molecular biology

2013;49(6):1120-1126.

130. Fuchs BC, Wang H, Yang Y, Wei L, Polasek M, Schühle DT, et al. Molecular MRI of collagen to diagnose and stage liver fibrosis. J Hepatol 2013;59(5):992-998.

131. Helm PA, Caravan P, French BA, Jacques V, Shen L, Xu Y, et al. Postinfarction Myocardial Scarring in Mice: Molecular MR Imaging with Use of a Collagen-targeting Contrast Agent 1. Radiology 2008;247(3):788-796.

132. Klink A, Heynens J, Herranz B, Lobatto ME, Arias T, Sanders HM, et al. In vivo characterization of a new abdominal aortic aneurysm mouse model with conventional and molecular magnetic resonance imaging. J Am Coll Cardiol 2011;58(24):2522-2530.

133. Megens RT, Oude Egbrink MG, Cleutjens JP, Kuijpers MJ, Schiffers PH, Merkx M, et al. Imaging collagen in intact viable healthy and atherosclerotic arteries using fluorescently labeled CNA35 and two-photon laser scanning microscopy. Mol Imaging 2007 Jul-Aug;6(4):247-260.

134. Mees G, Dierckx R, Mertens K, Vermeire S, Van Steenkiste M, Reutelingsperger C, et al. 99mTc-labeled tricarbonyl his-CNA35 as an imaging agent for the detection of tumor vasculature. J Nucl Med 2012 Mar;53(3):464-471.

135. Muzard J, Sarda-Mantel L, Loyau S, Meulemans A, Louedec L, Bantsimba-Malanda C, et al. Non-invasive molecular imaging of fibrosis using a collagen-targeted peptidomimetic of the platelet collagen receptor glycoprotein VI. PLoS One 2009;4(5):e5585.

136. Wenzel S, Taimor G, Piper HM, Schluter KD. Redox-sensitive intermediates mediate angiotensin II-induced p38 MAP kinase activation, AP-1 binding activity, and TGF-beta expression in adult ventricular cardiomyocytes. FASEB J 2001 Oct;15(12):2291-2293.

137. Schultz Jel J, Witt SA, Glascock BJ, Nieman ML, Reiser PJ, Nix SL, et al. TGF-beta1 mediates the hypertrophic cardiomyocyte growth induced by angiotensin II. J Clin Invest 2002 Mar;109(6):787-796.

138. Dostal DE. Regulation of cardiac collagen: angiotensin and cross-talk with local growth factors. Hypertension 2001 Mar;37(3):841-844.

139. Femia FJ, Maresca KP, Hillier SM, Zimmerman CN, Joyal JL, Barrett JA, et al. Synthesis and evaluation of a series of 99mTc(CO)3+ lisinopril complexes for in vivo imaging of angiotensin-converting enzyme expression. J Nucl Med 2008 Jun;49(6):970-977.

140. Dilsizian V, Zynda TK, Petrov A, Ohshima S, Tahara N, Haider N, et al. Molecular imaging of human ACE-1 expression in transgenic rats. JACC: Cardiovascular Imaging 2012;5(4):409-418.

141. Verjans JW, Lovhaug D, Narula N, Petrov AD, Indrevoll B, Bjurgert E, et al. Noninvasive imaging of angiotensin receptors after myocardial infarction. JACC: Cardiovascular Imaging 2008;1(3):354-362.

142. Fukushima K, Bravo PE, Higuchi T, Schuleri KH, Lin X, Abraham MR, et al. Molecular hybrid positron emission tomography/computed tomography imaging of cardiac angiotensin II type 1 receptors. J Am Coll Cardiol 2012;60(24):2527-2534.

143. van den Borne SW, Isobe S, Verjans JW, Petrov A, Lovhaug D, Li P, et al. Molecular imaging of interstitial alterations in remodeling myocardium after myocardial infarction. J Am Coll Cardiol 2008;52(24):2017-2028.

144. van den Borne SW, Isobe S, Zandbergen HR, Li P, Petrov A, Wong ND, et al. Molecular imaging for efficacy of pharmacologic intervention in myocardial remodeling. JACC: Cardiovascular Imaging 2009;2(2):187-198.

145. Verjans J, Wolters S, Laufer W, Schellings M, Lax M, Lovhaug D, et al. Early molecular imaging of interstitial changes in patients after myocardial infarction: comparison with delayed contrast-enhanced magnetic resonance imaging. Journal of nuclear cardiology 2010;17(6):1065-1072.

146. Meoli DF, Sadeghi MM, Krassilnikova S, Bourke BN, Giordano FJ, Dione DP, et al. Noninvasive imaging of myocardial angiogenesis following experimental myocardial infarction. J Clin Invest 2004 Jun;113(12):1684-1691.

147. Higuchi T, Bengel FM, Seidl S, Watzlowik P, Kessler H, Hegenloh R, et al. Assessment of alphavbeta3 integrin expression after myocardial infarction by positron emission tomography. Cardiovasc Res 2008 May 1;78(2):395-403.

148. Sherif HM, Saraste A, Nekolla SG, Weidl E, Reder S, Tapfer A, et al. Molecular imaging of early alphavbeta3 integrin expression predicts long-term left-ventricle remodeling after myocardial infarction in rats. J Nucl Med 2012 Feb;53(2):318-323.

149. Makowski MR, Ebersberger U, Nekolla S, Schwaiger M. In vivo molecular imaging of angiogenesis, targeting alphavbeta3 integrin expression, in a patient after acute myocardial infarction. Eur Heart J 2008 Sep;29(18):2201.

150. Chen J, Tung CH, Allport JR, Chen S, Weissleder R, Huang PL. Near-infrared fluorescent imaging of matrix metalloproteinase activity after myocardial infarction. Circulation 2005 Apr 12;111(14):1800-1805.

151. Sahul ZH, Mukherjee R, Song J, McAteer J, Stroud RE, Dione DP, et al. Targeted imaging of the spatial and temporal variation of matrix metalloproteinase activity in a porcine model of postinfarct remodeling: relationship to myocardial dysfunction. Circ Cardiovasc Imaging 2011 Jul;4(4):381-391.

152. van Duijnhoven SM, Robillard MS, Hermann S, Kuhlmann MT, Schäfers M, Nicolay K, et al. Imaging of MMP activity in postischemic cardiac remodeling using radiolabeled MMP-2/9 activatable peptide probes. Molecular pharmaceutics 2014;11(5):1415-1423.

153. Nakajima K, Taki J, Tonami N, Hisada K. Decreased 123I-MIBG uptake and increased clearance in various cardiac diseases. Nucl Med Commun 1994 May;15(5):317-323.

154. Travin MI. Clinical Applications of Myocardial Innervation Imaging. Cardiol Clin 2016 Feb;34(1):133-147.

155. Jacobson AF, Senior R, Cerqueira MD, Wong ND, Thomas GS, Lopez VA, et al. Myocardial iodine-123 meta-iodobenzylguanidine imaging and cardiac events in heart failure. J Am Coll Cardiol 2010;55(20):2212-2221.

156. Ketchum ES, Jacobson AF, Caldwell JH, Senior R, Cerqueira MD, Thomas GS, et al. Selective improvement in Seattle Heart Failure Model risk stratification using iodine-123 meta-iodobenzylguanidine imaging. Journal of Nuclear Cardiology 2012;19(5):1007-1016.

157. Narula J, Gerson M, Thomas GS, Cerqueira MD, Jacobson AF. (1)(2)(3)I-MIBG Imaging for Prediction of Mortality and Potentially Fatal Events in Heart Failure: The ADMIRE-HFX Study. J Nucl Med 2015 Jul;56(7):1011-1018.

158. Senior R, Friberg L, Travin M, Hudnut F, Chandna H, Agostini D, et al. Prognostic usefulness of AdreView scintigraphy in identifying heart failure patients at lower risk of death during 5-year follow-up in the ADMIRE-HF Study. J Am Coll Cardiol 2016;67(13):1812.

159. Boogers MJ, Borleffs CJW, Henneman MM, van Bommel RJ, van Ramshorst J, Boersma E, et al. Cardiac sympathetic denervation assessed with 123-iodine metaiodobenzylguanidine imaging predicts ventricular arrhythmias in implantable cardioverter-defibrillator patients. J Am Coll Cardiol 2010;55(24):2769-2777.

160. Travin MI, Henzlova MJ, van Eck-Smit BL, Jain D, Carrió I, Folks RD, et al. Assessment of 123I-mIBG and 99mTc-tetrofosmin single-photon emission computed tomographic images for the prediction of arrhythmic events in patients with ischemic heart failure: Intermediate severity innervation defects are associated with higher arrhythmic risk. Journal of Nuclear Cardiology 2016:1-15.

161. Tanaka H, Tatsumi K, Fujiwara S, Tsuji T, Kaneko A, Fukuda Y, et al. Effect of left ventricular dyssynchrony on cardiac sympathetic activity in heart failure patients with wide QRS duration. Circulation Journal 2012;76(2):382-389.

162. Nishioka SA, Martinelli Filho M, Brandão SCS, Giorgi MC, Vieira ML, Costa R, et al. Cardiac sympathetic activity pre and post resynchronization therapy evaluated by 123I-MIBG myocardial scintigraphy. Journal of Nuclear Cardiology 2007;14(6):852-859.

163. Fallavollita JA, Banas MD, Suzuki G, Sajjad M, Canty Jr JM. 11C-meta-hydroxyephedrine defects persist despite functional improvement in hibernating myocardium. Journal of nuclear cardiology 2010;17(1):85-96.

164. Münch G, Nguyen NT, Nekolla S, Ziegler S, Muzik O, Chakraborty P, et al. Evaluation of sympathetic nerve terminals with [11C] epinephrine and [11C] hydroxyephedrine and positron emission tomography. Circulation 2000;101(5):516-523.

165. Hansson GK. Inflammation, atherosclerosis, and coronary artery disease. N Engl J Med 2005;352:1685-1695.

166. Otsuka F, Fuster V, Narula J&, Virmani R. Omnipresent atherosclerotic disease: time to depart from analysis of individual vascular beds. Mt Sinai J Med 2012;79:641-653.

167. Narula J, Nakano M, Virmani R, Kolodgie FD, Petersen R, Newcomb R, et al. Histopathologic characteristics of atherosclerotic coronary disease and implications of the findings for the invasive and noninvasive detection of vulnerable plaques. J Am Coll Cardiol 2013 Mar 12;61(10):1041-1051.

168. Narula J, Garg P, Achenbach S, Motoyama S, Virmani R, Strauss HW. Arithmetic of vulnerable plaques for noninvasive imaging. Nat Clin Pract Cardiovasc Med 2008 Aug;5 Suppl 2:S2-10.

169. Rogers IS, Nasir K, Figueroa AL, Cury RC, Hoffmann U, Vermylen DA, et al. Feasibility of FDG imaging of the coronary arteries: comparison between acute coronary syndrome and stable angina. JACC Cardiovasc Imaging 2010 Apr;3(4):388-397.

170. Rudd JH, Narula J, Strauss HW, Virmani R, Machac J, Klimas M, et al. Imaging atherosclerotic plaque inflammation by fluorodeoxyglucose with positron emission tomography: ready for prime time? J Am Coll Cardiol 2010 Jun 8;55(23):2527-2535.

171. Shepherd PR, Kahn BB. Glucose transporters and insulin action: implications for insulin resistance and diabetes mellitus. N Engl J Med 1999;341:248-257.

172. Narula J, Strauss HW. The popcorn plaques. Nat Med 2007;13:532-534.

173. Villanueva FS, Jankowski RJ, Klibanov S, Pina ML, Alber SM, Watkins SC, et al. Microbubbles targeted to intercellular adhesion molecule-1 bind to activated coronary artery endothelial cells. Circulation 1998 Jul 7;98(1):1-5.

174. Kaufmann BA, Sanders JM, Davis C, Xie A, Aldred P, Sarembock IJ, et al. Molecular imaging of inflammation in atherosclerosis with targeted ultrasound detection of vascular cell adhesion molecule-1. Circulation 2007 Jul 17;116(3):276-284.

175. Hartung D, Petrov A, Haider N, Fujimoto S, Blankenberg F, Fujimoto A, et al. Radiolabeled Monocyte Chemotactic Protein 1 for the detection of inflammation in experimental atherosclerosis. J Nucl Med 2007 Nov;48(11):1816-1821.

176. Tsimikas S. Noninvasive imaging of oxidized low-density lipoprotein in atherosclerotic plaques with tagged oxidation-specific antibodies. Am J Cardiol 2002;90:22L-27L.

177. Finn AV, Nakano M, Polavarapu R, Karmali V, Saeed O, Zhao X, et al. Hemoglobin directs macrophage differentiation and prevents foam cell formation in human atherosclerotic plaques. J Am Coll Cardiol 2012 Jan 10;59(2):166-177.

178. Bouhlel MA, Derudas B, Rigamonti E, Dievart R, Brozek J, Haulon S, et al. PPARgamma activation primes human monocytes into alternative M2 macrophages with anti-inflammatory properties. Cell Metab 2007 Aug;6(2):137-143.

179. Gould GW, Thomas HM, Jess TJ, Bell GI. Expression of human glucose transporters in Xenopus oocytes: kinetic characterization and substrate specificities of the erythrocyte, liver, and brain isoforms. Biochemistry 1991;30:5139-5145.

180. de la Fuente M, Hernanz A. Enzymes of mannose metabolism in murine and human lymphocytic leukaemia. Br J Cancer 1988;58:567-569.

181. Furumoto S, Shinbo R, Iwata R, Ishikawa Y, Yanai K, Yoshioka T, et al. In vitro and in vivo characterization of 2-deoxy-2-18F-fluoro-D-mannose as a tumor-imaging agent for PET. J Nucl Med 2013 Aug;54(8):1354-1361.

182. Halestrap AP. Calcium, mitochondria and reperfusion injury: a pore way to die. Biochem Soc Trans 2006;34:232-237.

183. Vivian Liao T, C Forehand C, C Hess D, C Fagan S. Minocycline Repurposing in Critical Illness: Focus on Stroke. Current topics in medicinal chemistry 2013;13(18):2283-2290.

184. Fagan SC, Waller JL, Nichols FT, Edwards DJ, Pettigrew LC, Clark WM, et al. Minocycline to improve neurologic outcome in stroke (MINOS): a dose-finding study. Stroke 2010 Oct;41(10):2283-2287.

185. Amiri-Nikpour MR, Nazarbaghi S, Hamdi-Holasou M, Rezaei Y. An open-label evaluator-blinded clinical study of minocycline neuroprotection in ischemic stroke: gender-dependent effect. Acta Neurol Scand 2015;131(1):45-

6

50.

186. Padma Srivastava MV, Bhasin A, Bhatia R, Garg A, Gaikwad S, Prasad K, et al. Efficacy of minocycline in acute ischemic stroke: a single-blinded, placebo-controlled trial. Neurol India 2012 Jan-Feb;60(1):23-28.

187. Lampl Y, Boaz M, Gilad R, Lorberboym M, Dabby R, Rapoport A, et al. Minocycline treatment in acute stroke: an open-label, evaluator-blinded study. Neurology 2007 Oct 2;69(14):1404-1410.

188. Romero-Perez D, Fricovsky E, Yamasaki KG, Griffin M, Barraza-Hidalgo M, Dillmann W, et al. Cardiac uptake of minocycline and mechanisms for in vivo cardioprotection. J Am Coll Cardiol 2008;52(13):1086-1094.

189. Scarabelli TM, Stephanou A, Pasini E, Gitti G, Townsend P, Lawrence K, et al. Minocycline inhibits caspase activation and reactivation, increases the ratio of XIAP to smac/DIABLO, and reduces the mitochondrial leakage of cytochrome C and smac/DIABLO. J Am Coll Cardiol 2004;43(5):865-874.

190. Hu X, Zhou X, He B, Xu C, Wu L, Cui B, et al. Minocycline protects against myocardial ischemia and reperfusion injury by inhibiting high mobility group box 1 protein in rats. Eur J Pharmacol 2010;638(1):84-89.

191. Hu X, Wu B, Wang X, Xu C, He B, Cui B, et al. Minocycline attenuates ischemia-induced ventricular arrhythmias in rats. Eur J Pharmacol 2011;654(3):274-279.

192. Fadok VA, Voelker DR, Campbell PA, Cohen JJ, Bratton DL, Henson PM. Exposure of phosphatidylserine on the surface of apoptotic lymphocytes triggers specific recognition and removal by macrophages. J Immunol 1992 Apr 1;148(7):2207-2216.

193. van der Have F, Vastenhouw B, Ramakers RM, Branderhorst W, Krah JO, Ji C, et al. U-SPECT-II: An Ultra-High-Resolution Device for Molecular Small-Animal Imaging. J Nucl Med 2009 Apr;50(4):599-605.

194. Branderhorst W, Vastenhouw B, Beekman FJ. Pixel-based subsets for rapid multi-pinhole SPECT reconstruction. Phys Med Biol 2010;55(7):2023.

195. Bowsher JE, Johnson VE, Turkington TG, Jaszczak RJ, Floyd C, Coleman RE. Bayesian reconstruction and use of anatomical a priori information for emission tomography. IEEE Trans Med Imaging 1996;15(5):673-686.

196. Wu C, van der Have F, Vastenhouw B, Dierckx RA, Paans AM, Beekman FJ. Absolute quantitative total-body small-animal SPECT with focusing pinholes. European journal of nuclear medicine and molecular imaging 2010;37(11):2127-2135.

197. Switzer JA, Hess DC, Ergul A, Waller JL, Machado LS, Portik-Dobos V, et al. Matrix metalloproteinase-9 in an exploratory trial of intravenous minocycline for acute ischemic stroke. Stroke 2011 Sep;42(9):2633-2635.

198. Konstantinidis K, Whelan RS, Kitsis RN. Mechanisms of cell death in heart disease. Arterioscler Thromb Vasc Biol 2012;32:1552-1562.

199. Nikoletopoulou V, Markaki M, Palikaras K, Tavernarakis N. Crosstalk between apoptosis, necrosis and autophagy. Biochimica et Biophysica Acta (BBA)-Molecular Cell Research 2013;1833(12):3448-3459.

200. Nicotera P, Melino G. Regulation of the apoptosis-necrosis switch. Oncogene 2004;23:2757-2765.

201. Boersma HH, Kietselaer BL, Stolk LM, Bennaghmouch A, Hofstra L, Narula J, et al. Past, present, and future of annexin A5: from protein discovery to clinical applications. J Nucl Med 2005 Dec;46(12):2035-2050.

202. Thimister PW, Hofstra L, Liem IH, Boersma HH, Kemerink G, Reutelingsperger CP, et al. In vivo detection of cell death in the area at risk in acute myocardial infarction. J Nucl Med 2003 Mar;44(3):391-396.

203. Narula J, Acio ER, Narula N, Samuels LE, Fyfe B, Wood D, et al. Annexin-V imaging for noninvasive detection of cardiac allograft rejection. Nat Med 2001 Dec;7(12):1347-1352.

204. Khaw BA, Narula J. Non-invasive detection of myocyte necrosis in myocarditis and dilated cardiomyopathy with radiolabelled antimyosin. Eur Heart J 1995;16 Suppl O:119-123.

205. Corbett JR, Lewis M, Willerson JT, Nicod PH, Huxley RL, Simon T, et al. 99mTc-pyrophosphate imaging in patients with acute myocardial infarction: comparison of planar imaging with single-photon tomography with and without blood pool overlay. Circulation 1984 Jun;69(6):1120-1128.

206. Narula J, Southern JF, Dec GW, Palacios IF, Newell JB, Fallon JT, et al. Antimyosin uptake and myofibrillarlysis in dilated cardiomyopathy. J Nucl Cardiol 1995 Nov-Dec;2(6):470-477.

207. Park D, Don AS, Massamiri T, Karwa A, Warner B, MacDonald J, et al. Noninvasive imaging of cell death using an Hsp90 ligand. J Am Chem Soc 2011;133(9):2832-2835.

208. Park D, Xie B, Van Beek ER, Blankevoort V, Que I, Löwik CW, et al. Optical imaging of treatment-related tumor cell death using a heat shock protein-90 alkylator. Molecular Pharmaceutics 2013;10(10):3882-3891.

209. Xie B, Park D, Van Beek E, Blankevoort V, Orabi Y, Que I, et al. Optical imaging of cell death in traumatic brain injury using a heat shock protein-90 alkylator. Cell death & disease 2013;4(1):e473.

210. Donoghue N, Yam PT, Jiang XM, Hogg PJ. Presence of closely spaced protein thiols on the surface of mammalian cells. Protein Sci 2000;9:2436-2445.

211. Dilda PJ, Ramsay EE, Corti A, Pompella A, Hogg PJ. Metabolism of the tumor angiogenesis inhibitor 4-(N-(S-Glutathionylacetyl)amino)phenylarsonous acid. J Biol Chem 2008;283:35428-35434.

212. Goetz MP, Toft DO, Ames MM, Erlichman C. The Hsp90 chaperone complex as a novel target for cancer therapy. Ann Oncol 2003;14:1169-1176.

213. Narula J, Petrov A, Pak KY, Lister BC, Khaw BA. Very early noninvasive detection of acute experimental nonreperfused myocardial infarction with 99mTc-labeled glucarate. Circulation 1997 Mar 18;95(6):1577-1584.

214. Proost JH, Meijer DK. MW/Pharm, an integrated software package for drug dosage regimen calculation and therapeutic drug monitoring. Comput Biol Med 1992;22:155-163.

215. Halestrap AP, Gillespie JP, O'Toole A, Doran E. Mitochondria and cell death: a pore way to die? Symp Soc Exp Biol 2000;52:65-80.

216. Arbustini E, Narula J. Cyclosporin a in reperfusion injury: not opening to cell death knocking at the door? Ann Thorac Surg 2010;89:1349-1351.

217. Scarabelli TM. Clinical implications of apoptosis in ischemic myocardium. Curr Probl Cardiol 2006;31:181-264.

218. Fliss H, Gattinger D. Apoptosis in ischemic and reperfused rat myocardium. Circ Res 1996;79:949-956.

219. Freude B, Masters TN, Robicsek F, Fokin A, Kostin S, Zimmermann R, et al. Apoptosis is initiated by myocardial ischemia and executed during reperfusion. J Mol Cell Cardiol 2000 Feb;32(2):197-208.

220. Gottlieb RA, Burleson KO, Kloner RA, Babior BM, Engler RL. Reperfusion injury induces apoptosis in rabbit cardiomyocytes. J Clin Invest 1994;94:1621-1628.

221. Li C, Jackson RM. Reactive species mechanisms of cellular hypoxia-reoxygenation injury. Am J Physiol Cell Physiol 2002 Feb;282(2):C227-41.

222. Orrenius S, Zhivotovsky B, Nicotera P. Regulation of cell death: the calcium-apoptosis link. Nat Rev Mol Cell Biol 2003;4:552-565.

223. Halestrap A. Biochemistry: a pore way to die. Nature 2005;434:578-579.

224. Yue TL, Ma XL, Wang X, Romanic AM, Liu GL, Louden C, et al. Possible involvement of stress-activated protein kinase signaling pathway and Fas receptor expression in prevention of ischemia/reperfusion-induced cardiomyocyte apoptosis by carvedilol. Circ Res 1998 Feb 9;82(2):166-174.

225. Condorelli G, Morisco C, Stassi G, Notte A, Farina F, Sgaramella G, et al. Increased cardiomyocyte apoptosis and changes in proapoptotic and antiapoptotic genes bax and bcl-2 during left ventricular adaptations to chronic pressure overload in the rat. Circulation 1999 Jun 15;99(23):3071-3078.

226. Li Z, Bing OH, Long X, Robinson KG, Lakatta EG. Increased cardiomyocyte apoptosis during the transition to heart failure in the spontaneously hypertensive rat. Am J Physiol 1997;272:H2313-2319.

227. Narula J, Haider N, Arbustini E, Chandrashekhar Y. Mechanisms of disease: apoptosis in heart failure—seeing hope in death. Nature Clinical Practice Cardiovascular Medicine 2006;3(12):681-688.

228. De Saint-Hubert M, Prinsen K, Mortelmans L, Verbruggen A, Mottaghy FM. Molecular imaging of cell death. Methods 2009;48(2):178-187.

229. Perugini E, Rapezzi C, Piva T, Leone O, Bacchi-Reggiani L, Riva L, et al. Non-invasive evaluation of the myocardial substrate of cardiac amyloidosis by gadolinium cardiac magnetic resonance. Heart 2006 Mar;92(3):343-349.

230. Shimada T, Shimada K, Sakane T, Ochiai K, Tsukihashi H, Fukui M, et al. Diagnosis of cardiac sarcoidosis and

6

evaluation of the effects of steroid therapy by gadolinium-DTPA-enhanced magnetic resonance imaging. Am J Med 2001 May;110(7):520-527.

231. de Haas HJ, Arbustini E, Fuster V, Kramer CM, Narula J. Molecular imaging of the cardiac extracellular matrix. Circ Res 2014 Feb 28;114(5):903-915.

232. Tahara N, Zandbergen HR, de Haas HJ, Petrov A, Pandurangi R, Yamaki T, et al. Noninvasive molecular imaging of cell death in myocardial infarction using 111In-GSAO. Sci Rep 2014 Oct 29;4:6826.

233. Cohen J. Statistical power analysis for the behavioral sciences Lawrence Earlbaum Associates. Hillsdale, NJ 1988:20-26.

List of Abbreviations

^{123}I-MIBG = ^{123}I-meta-iodobenzylguanidine

^{14}C-CDG = ^{14}C-2-deoxy-2-carbon-D-glucose

^{18}F-FDG = ^{18}F-2-fluoro-2-deoxy-D-glucose

^{18}F-FDM = ^{18}F-2-fluoro-2-deoxy-D-mannose

^{18}F-NaF = ^{18}F-Sodium Fluoride

4,6-diamino-2-phenylindole (DAPI)

^{99}mTc-CRIP = ^{99}mTc-Cy5.5 RGD imaging peptide

^{99}mTc-RIP = ^{99m}Tc-RGD imaging peptide

α-SMA = smooth muscle actin

ACE = angiotensin converting enzyme

ANOVA = analysis of variance

AT1R = angiotensin II receptor type 1

ATP = adenosine triphosphate

CABG = and coronary artery bypass graft surgery

CPCU = chemistry processing computer unit

CT = computed tomography

CVA = cerebrovascular accident

DLU = digital light units

GGT = γ-glutamyl transferase

GLUT = glucose transporter

GSAO = 4-(N-(S-glutathionylacetyl)amino)phenylarsonous acid

GSCA = (4-(N-(S-cysteinylglycylacetyl)amino) phenylarsonous acid)

HMR = heart/mediastinum ratio

HSP90 = heat shock protein 90

LAD = left anterior descending coronary artery

LDL = low density lipoprotein

LDLox = oxidized low density lipoprotein

LGE = late gadolinium enhancement

MMP = matrix metalloproteinases

MRI = magnetic resonance imaging

PBS = phosphate-buffered saline

PCI = percutaneous coronary intervention

PDI = protein disulfide isomerase

PET = positron emission tomography

POSEM = pixel-based ordered subset expectation maximization

PS = phosphatidyl serine

RGD = arginine-glycine-aspartate

6

ROI = region of interest

SPECT = single photon emission computed tomography

SUV = standardized uptake value

TCFA = thin-cap fibroatheromas

TUNEL = Terminal deoxynucleotidyl transferase-mediated deoxyuridine triphosphate nick-end labeling

USPIO = ultra small superparamagnetic particles of iron oxide

General summary

Atherosclerotic cardiovascular disease is one of the main causes of mortality worldwide. Atherosclerosis is an inflammatory disease, which is characterized by the formation of lipid plaques in the arterial wall. Myocardial infarction is caused an acute coronary artery obstruction, usually resulting from a plaque rupture and thrombotization. This gives rise to lack of blood flow and subsequent tissue loss through programmed (apoptosis) and unprogrammed (necrosis) cell death. Primary percutaneous coronary intervention (PCI) is the mainstay of treatment. This procedure reopens the coronary, restores the blood flow and salvages part of the ischemic cardiac tissue. Additional therapies to reduce cardiac cell death are required to further enhance outcomes after myocardial infarction.

Molecular imaging allows visualization of biological processes. For this, tracer molecules targeting specific molecules or cells are administered to patients or laboratory animals. As these tracers are labeled, their accumulation can be detected.

Clinical applications of molecular imaging include optimization of diagnosis and choice and monitoring of therapeutic strategies. For instance, patients at high risk of myocardial infarction can be identified through detection of high-risk atherosclerotic plaques by molecular imaging techniques. Moreover, molecular imaging can be used to study pathology and develop novel therapies.

Chapter 1 provides a general overview of cardiovascular molecular imaging. The concept of molecular imaging is defined, the various molecular imaging platforms are described, and the clinical and academic usages are discussed. Additionally, an overview of the various molecular imaging strategies in atherosclerosis, myocardial infarction and adverse remodeling explored so far is given.

In chapter 2 we report feasibility of atherosclerotic plaque imaging by positron emission tomography (PET) using ^{18}F-labeled mannose (2-fluoro-2-deoxy-D-mannose, ^{18}F-FDM).

We first performed histological studies on human coronary atherosclerotic plaques and demonstrated substantial presence of mannose receptor-bearing macrophages in plaques with high-risk morphology, establishing this cell type as a potential target for high-risk plaque imaging.

Second, we performed extensive experiments in cultured macrophages and demonstrated that ^{18}F-FDM is taken up by activated macrophages through the same mechanism as ^{18}F-FDG, the gold standard for molecular atherosclerosis imaging. Moreover, we observed that ^{18}F-FDM binds to mannose receptors on cultured macrophages. This suggests that ^{18}F-FDM may accumulate in high-risk plaques through targeting of the mannose receptor in addition to its metabolic targeting of macrophages.

Finally, we evaluated *in vivo* ^{18}F-FDM PET in animal experiments. As animal models of atherosclerotic plaques containing mannose receptor-bearing macrophages are currently unavailable, we were unable to determine whether ^{18}F-FDM uptake is higher than ^{18}F-FDG uptake based on specific targeting of this cell type. However, by comparing uptake of both radiotracers in atherosclerotic rabbits we demonstrated non-inferiority of ^{18}F-FDM to ^{18}F-FDG.

We thus conclude that for atherosclerotic plaque imaging, ^{18}F-FDM PET is non-inferior to ^{18}F-FDG PET imaging and through targeting of mannose receptor-bearing macrophages may be superior for detection of high risk plaques in patients.

The next chapters focus on molecular imaging of cell death for the evaluation of the cardioprotective effects of minocycline. Previous pre-clinical studies had demonstrated efficacy of minocycline treatment before the onset of myocardial infarction, which can rarely occur in clinical practice. To simulate reperfused acute myocardial infarction, we used animal models of myocardial ischemia and reperfusion. We used clinically translatable therapeutic protocols with minocycline therapy upon onset of reperfusion.

In chapter 3 we employed ^{99m}Tc-annexin A5 imaging to obtain initial data suggesting cardioprotection of minocycline therapy. ^{99m}Tc-annexin A5 binds to phosphatidyl Serine (PS), which translocates to the outer leaflet of cells undergoing apoptosis, a form of programmed cell death.

Cardiac ischemia and subsequent reperfusion were induced in mice and rabbits by temporary coronary ligation. Subgroups of animals were treated with minocycline upon onset of reperfusion. In rabbits, *ex vivo* planar imaging showed lower uptake in minocycline-treated animals. Subsequent quantification of radiotracer uptake by gamma counting revealed a trend of lower uptake in minocycline-treated rabbits, although statistical significance was not reached in this small-sample study.

In mice, absolutely quantified *in vivo* ^{99m}Tc-annexin A5 single photon emission computed tomography (SPECT) imaging revealed lower uptake in minocycline-treated than in untreated animals. This was confirmed by immunohistological evaluation of apoptosis by terminal deoxynucleotidyl transferase-mediated deoxyuridine triphosphate nick-end labeling (TUNEL) staining.

For more definitive results, efficacy of minocycline was evaluated in the rabbit model of acute myocardial infarction using ^{111}In-labeled 4-(N-(s-glutathionylacetyl) amino) phenylarsenoide (^{111}In-GSAO). GSAO is an organoarsenical molecule that binds to intracellular molecules with dithiol moieties. When labeled with radioactive or fluorescent reporter molecules, GSAO is membrane impermeable. As the cell membrane of dying cells is compromised, GSAO gains access to its target molecules, allowing its accumulation.

In chapter 4, we describe validation of cardiac cell death imaging using ^{111}In-GSAO in rabbit and mouse models of myocardial infarction. First, we co-administered fluorescently labeled GSAO and Annexin A5 to mice with experimental acute myocardial infarction. We demonstrated that GSAO accumulated intracellularly, with low extracellular background, in annexin A5-positive cells, suggesting that GSAO predominantly recognized secondary necrotic cell death following initial upregulation in apoptotic signaling.

Next, we went on to *in vivo* nuclear imaging experiments in rabbits with experimental acute myocardial infarction; subsets of animals underwent dual-tracer imaging protocols. We demonstrated high cardiac ^{111}In-GSAO uptake in the infarct area as demonstrated by perfusion tracer ^{99m}Tc-sestamibi. Moreover, ^{111}In-GSAO uptake colocalized and strongly correlated with ^{99m}Tc-annexin A5 uptake. Lack of uptake of ^{111}In-GSCA, (4-(N-(S-glutathionylacetyl)amino)benzoic acid), a control compound, demonstrated specificity of ^{111}In-GSAO.

Next, experiments in mice with acute myocardial infarction confirmed high cardiac uptake ^{111}In-GSAO. Imaging in mice with chronic myocardial infarction (persistent coronary occlusion followed by imaging at 2, 4 or 12 weeks) revealed markedly lower cardiac ^{111}In-GSAO uptake than in mice with acute myocardial infarction. Our data demonstrate that ^{111}In-GSAO can be used to identify cell death in acute

myocardial infarction. Low uptake of ^{111}In-GSAO in mice with chronic myocardial infarction is probably due to limited rates of cell death during remodeling after myocardial infarction.

In the study described in chapter 5, we employed ^{111}In-GSAO imaging to evaluate minocycline therapy in rabbits with experimental acute myocardial infarction. Rabbits with experimental acute myocardial infarction were were divided into a minocycline-treated group and a control group. *In vivo* and *ex vivo* ^{111}In-GSAO SPECT imaging and subsequent gamma counting revealed markedly lower ^{111}In-GSAO uptake in minocycline treated animals. (Immuno)histology confirmed lower rates of apoptosis and reduced morphological signs of tissue damage in minocycline-treated animals.

General discussion and future perspectives

Imaging of atherosclerosis: focus on FDM

Currently, treatment of atherosclerosis is mainly guided by risk-factor-based risk scores. A drawback of these scores is that the predictive value of applying epidemiologic data to individual patients is limited. Molecular imaging has been extensively investigated as a tool to optimize risk stratification of cardiovascular patients. Initially, the field of atherosclerosis imaging focused on identifying atherosclerotic plaques at risk of rupture and thus would require aggressive (invasive) therapy. This approach however, has not reached clinical acceptance as recent studies have shown that in most cases, plaques with a "vulnerable" phenotype stabilize over time rather than cause events. Thus, the field has shifted to evaluating disease activity over the global arterial bed, aiming to identify "vulnerable patients".

Given the drawbacks of molecular imaging including radiation burden and use of resources, large clinical studies will have to demonstrate substantial added value compared with risk factor and biosoluble risk scores in terms of improving cardiovascular outcomes.

In fact, the main purpose of molecular imaging may lie in (pre)clinical research. It is the penultimate tool to investigate pathology *in vivo*, which can lead to novel therapeutic and preventative strategies. Moreover, molecular imaging is increasingly being used to evaluate the efficacy of (targeted) therapies. For atherosclerosis, various targets have been evaluated including matrix metallo proteinases, markers of angiogenesis, vascular calcification and apoptosis.

The most widely studied molecular imaging technique is imaging vascular inflammation using ^{18}F-FDG PET. Vascular ^{18}F-FDG uptake correlates with cardiovascular risk factors, cardiovascular outcomes and is able to identify high-risk plaques at the individual plaque level. ^{18}F-FDG PET is also widely used measure the effect of therapies in clinical studies.

We have demonstrated in chapter 2 that ^{18}F-FDM PET is non-inferior to ^{18}F-FDG PET in visualizing atherosclerotic plaques and propose that it may be more sensitive to plaques with a high-risk phenotype due to additional targeting of the mannose receptor on M2 macrophages. As these macrophages are not present in animal models, we have been unable to definitively demonstrate superiority of ^{18}F-FDM over ^{18}F-FDG. For this purpose, clinical studies are required. Moreover, the radiolabeling procedure needs to be optimized, as the current low radiochemical yield would challenge clinical usage.

Besides FDG and FDM, various other molecular imaging strategies targeting inflammatory cells are emerging. A relevant example of this is magnetic resonance imaging (MRI) using ultra small particles of iron oxide (USPIO), which are phagocytized by macrophages in the vascular wall. Another candidate is PET imaging using ^{18}F-Dotatate, which binds to the somatostatin receptor, present on M2 macrophages in high-risk plaques. Although experience with these probes is limited compared to FDG, a major advantage of both is that there is no physiological uptake of these tracers by cardiac muscle. This would allow coronary imaging, which remains a major challenge for FDG and FDM PET.

Molecular imaging of cardiac injury and remodeling.

Cell death was one of the first molecular cardiovascular targets to be visualized by *in vivo* molecular imaging. In the 1990's, the necrosis tracer ^{111}In-antimyosin was even approved by the United States Food and Drug Association (FDA) diagnosis of myocardial infarction. It never reached widespread usage, largely because of its long circulating half life and the emergence of soluble biomarkers of cardiac damage. Given the success of this diagnostic approach, the clinical role of cell death imaging in acute coronary syndromes, even with superior imaging tracers, is limited. However, cardiac cell death imaging could play a diagnostic role in assessing cardiac transplant rejection, which currently requires serial endomyocardial biopsy, an invasive procedure associated with considerable patient discomfort, risk of complications and cost.

Moreover, cardiac cell death imaging could be a valuable research tool in the development of (novel) cardioprotective therapies for myocardial infarction. The gold-standard endpoints for such studies are major adverse cardiac events (such as death, or hospitalization for heart failure) or reduction of left ventricular ejection fraction, which require large study populations. As a surrogate endpoint myocardial salvage is often estimated as a ratio of infarct size as assessed by late gadolinium enhancement (LGE)-MRI to area at risk (as assessed by T2 weighted MRI). However, the validity of this approach is disputed. Molecular imaging of cell death could serve as an ideal direct endpoint in this setting.

In recent years the most widely studied radiotracer for cardiac cell death was apoptosis-targeting ^{99m}Tc-annexin A5. Initial pilot studies have shown feasibility of imaging with this tracer in myocardial infarction, transplant rejection, cardiomyopathy and other instances. However, as apoptosis is a reversible process, annexin A5 uptake not necessarily reflects irreversible cardiac damage.

For this purpose, we evaluated ^{111}In-GSAO in chapter 4, and demonstrated feasibility of irreversible cell death imaging in rabbits and mice with experimental acute myocardial infarction using this tracer. Because of its short circulating half life, imaging with this tracer can be performed substantially earlier after injection than with ^{111}In-antimyosin.

Moreover, given the fact that it is labeled with ^{111}In, dual tracer imaging with ^{99m}Tc-annexin A5 can be performed, allowing simultaneous evaluation of apoptotic signaling and necrotic cell death.

In addition, we have employed molecular imaging techniques to evaluate cardioprotective effects of minocycline. Preclinical and clinical studies had shown protective effects in stroke and shown that high doses are well tolerated. Moreover, initial pre-clinical studies had shown protective effect of minocycline in animal models of myocardial infarction, based on inhibition of apoptosis, oxidative stress and inflammation. In all studies, minocycline was administered before induction of cardiac ischemia,

which is rarely possible in clinical practice.

In chapter 3 we obtained initial data supporting cardioprotective effects of minocycline therapy upon reperfusion in mouse and rabbit models of acute myocardial infarction. In this study, we used *in vivo* and *ex vivo* [99mTc]-annexin A5 imaging for evaluation of cell death. Next, we corroborated cardiac efficacy of minocycline therapy upon reperfusion in rabbits with experimental acute myocardial infarction, applying *in vivo* ^{111}In-GSAO imaging. These reductions of cell death in clinically translatable models support continuation of research regarding of minocycline as a cardioprotective agent. As we have been unable to study the long-term effects of minocycline therapy for myocardial infarction, this will be an important next step. In the case of promising results, we support initiation of clinical trials regarding this widely used, well-tolerated and affordable drug.

Conclusions

In this thesis, we describe novel imaging techniques to visualize inflammation in atherosclerotic vessels and cardiac cell death. Moreover, we apply molecular imaging techniques to assess cardioprotective effects of minocycline in animal models of myocardial infarction. These, and similar imaging technqiues hold promise to optimize diagnosis, risk stratification, and thereby facilitate personalized cardiovascular medicine. Moreover, we expect to see a growing contribution of molecular imaging in (pre)clinical investigations into pathology and (novel) preventative and therapeutic strategies.

6

Nederlandse samenvatting

Atherosclerotische cardiovasculaire ziekten behoren wereldwijd tot de belangrijkste doodsoorzaken. Atherosclerose is een ontstekingsziekte, die leidt tot de vorming van vetrijke plaques in de slagaderwand. Het scheuren van kransslagaderplaques kan leiden tot vaatafsluiting door thrombusvorming en vormt de belangrijkste oorzaak van het myocardinfarct. Hierbij krijgt een deel van de hartspier onvoldoende bloed (ischemie), hetgeen leidt tot geprogrammeerde (apoptose) en ongeprogrammeerde (necrose) celdood en daarmee tot het afsterven van spierweefsel. Primaire percutane interventie (PCI, ofwel dotterbehandeling) is de standaardbehandeling voor het myocardinfart. Hierbij wordt het bloedvat heropend, de doorbloeding hersteld (reperfusie), en daarmee een deel van het ischemische hartspiergebied gered. Aanvullende therapieën om celdood in de hartspier te verminderen zijn nodig om de overleving en kwaliteit van leven van patiënten na een hartinfarct te verbeteren.

Bij moleculaire beeldvorming worden tracermoleculen toegediend aan mensen of proefdieren, om biologische processen te visualiseren. Deze tracermoleculen binden aan moleculaire targets of worden door specifieke cellen opgenomen. Doordat deze tracermoleculen gelabeld zijn, kan de opstapeling ervan in het lichaam in beeld gebracht worden.

Klinische toepassingen van moleculaire beeldvorming zijn het optimaliseren van diagnostiek, en het kiezen en evalueren van behandelingen. Door plaques op te sporen die een hoog risico hebben om in te scheuren, kunnen bijvoorbeeld patiënten met een hoog risico op het hartinfarct worden geïdentificeerd. Daarnaast kan moleculaire beeldvorming worden gebruikt worden voor het onderzoeken van ziektemechanismen, en de ontwikkeling van behandelingen.

In hoofdstuk 1 wordt een algemeen overzicht gegeven van cardiovasculaire moleculaire beeldvorming. Het begrip moleculaire beeldvorming wordt gedefinieerd, de verschillende moleculaire beeldvormingsmethoden worden beschreven en er wordt ingegaan op de klinische en academische toepassingen ervan. Daarnaast wordt een overzicht gegeven van verschillende vormen van moleculaire beeldvorming om atherosclerose, het hartinfarct en veranderingen van de hartspier na het hartinfarct (remodeling) in beeld te brengen.

In hoofdstuk 2 worden de resultaten van een onderzoek naar beeldvorming van atherosclerotische plaques middels positron emission tomography (PET) en de radiotracer 2-fluoro-2-deoxy-D-mannose (^{18}F-FDM) beschreven.

Ten eerste hebben we met histologische experimenten laten zien dat de subpopulatie van macrofagen die mannose receptoren op hun celmembranen presenteert, in substantiële mate aanwezig is in hoog-risico atherosclerotische plaques. Hierdoor vormen deze cellen een potentieel target voor moleculaire beeldvorming om deze categorie atherosclerotische plaques te detecteren.

Ten tweede hebben we met uitgebreide celexperimenten zien dat ^{18}F-FDM in geactiveerde macrofagen wordt opgenomen middels hetzelfde mechanisme als ^{18}F-FDG, de meest onderzochte tracer voor atherosclerose beeldvorming. Daarnaast hebben we middels cel-experimenten aangetoond dat ^{18}F-FDM aan mannosereceptoren op macrofagen bindt. Dit suggereert dat ^{18}F-FDM het koolhydraatmetabolisme van macrofagen als beeldvormingstarget in atherosclerotische plaques deelt met ^{18}F-FDG en vanwege

extra binding aan de mannose receptor een hogere opname in hoog-risicoplaques zou kunnen hebben. Ten slotte hebben we ^{18}F-FDM PET onderzocht in proefdierexperimenten. Helaas waren proefdiermodellen van atherosclerotische plaques waarin de macrofagen van het mannosereceptor-presenterende subtype voorkomen niet beschikbaar. Derhalve was het niet mogelijk te onderzoeken of ^{18}F-FDM een hogere opname vertoont dan ^{18}F-FDG op basis binding aan deze receptor. Echter, door de opname van beide tracers te vergelijken in een konijnmodel van atherosclerose, hebben we kunnen aantonen dat de accumulatie van ^{18}F-FDM in atherosclerotische plaques vergelijkbaar is met die van ^{18}F-FDG. We concluderen derhalve dat ^{18}F-FDM PET non-inferieur is aan ^{18}F-FDG PET, en vanwege additionele binding aan de mannose receptor-presenterende macrofagen superieur zou kunnen zijn voor de identificatie van hoog-risico atherosclerotische plaques in mensen.

In de hierop volgende hoofdstukken wordt ingegaan op moleculaire beeldvorming van celdood voor het evalueren van minocycline als behandeling voor het hartinfarct. Voorgaande proefdierstudies hadden laten zien dat minocyclinebehandeling voorafgaand aan het myocardinfarct effectief is. In patiënten met een acuut myocardinfarct kan behandeling echter pas later worden toegepast. Om de klinische situatie van het acute myocardinfarct gevolgd door behandeling met primaire percutane coronaire interventie te simuleren, hebben wij proefdiermodellen van cardiale ischemie-reperfusie gebruikt, waarbij een kransslagader tijdelijk werd gesloten middels een hechting. In de behandelde dieren werd minocycline pas rond de start van reperfusie (het losmaken van de hechting) toegediend.

Voor het onderzoek dat wordt beschreven in hoofdstuk 3, hebben we ^{99m}Tc-annexine A5 beeldvorming gebruikt om de effecten van minocycline te evalueren. ^{99m}Tc-annexine A5 bindt aan cellen die apoptose (een vorm van geprogrammeerde celdood), via phosphatidyl serine (PS) op de celmembraan van deze cellen.

Voor dit onderzoek werden muizen en konijnen met een acuut hartinfarctinfarct gebruikt. Subgroepen van de muizen en konijnen werden behandeld met minocycline aan het begin van de reperfusie. In konijnen toonde *ex vivo* beeldvorming een beperktere stapeling van ^{99m}Tc-annexine A5 in de harten van met minocycline behandelde dieren aan, dan in die van onbehandelde controledieren. Kwantificatie van de radiotracerstapeling middels gamma counting liet een trend van lagere opname in met minocycline behandelde konijnen zien, hoewel statistische significantie niet werd bereikt in dit kleine experiment.

In muizen werd *in vivo* ^{99m}Tc-Annexine A5 SPECT beeldvorming uitgevoerd en gekwantificeerd. Hierbij werd een lagere cardiale opname gezien in met minocycline behandelde muizen dan in onbehandelde controlemuizen. De lagere mate van geprogrammeerde celdood werd vervolgens bevestigd met de terminal deoxynucleotidyl transferase-mediated deoxyuridine triphosphate nick-end labeling (TUNEL) kleuring.

Voor verdere ondersteuning van bovenstaande resultaten werd de effectiviteit van minocycline in konijnen nader onderzocht met ^{111}In-4-(N-(s-glutathionylacetyl) amino) phenylarsenoide (^{111}In-GSAO). GSAO is een organoarsenicummolecuul dat aan intracellulaire moleculen met dithiol groepen bindt. Als GSAO gelabeld is met een radioactief of fluorescent molecuul, kan het niet over intacte celmembranen getransporteerd worden. In necrotische (stervende of dode) cellen vallen er gaten in de celmembraan, waardoor GSAO toegang verkrijgt tot zijn targetmoleculen en kan accumuleren. Derhalve kan GSAO gebruikt worden als tracermolecuul voor celdood.

6

In hoofdstuk 4 wordt de validatie van beeldvorming van cardiale celdood middels ^{111}In-GSAO beschreven. Ten eerste hebben we fluorescent gelabeld GSAO en annexine A5 toegediend aan muizen met experimentele acute myocardinfarcten. We laten GSAO accumulatie in annexine A5-positieve cellen zien. Dit suggereert dat GSAO voornamelijk necrose volgend op apoptotische activiteit herkent.

Vervolgens hebben we uitgebreide *in vivo* moleculaire beeldvormingsexperimenten uitgevoerd in konijnen met acuut myocardinfarct. In sommige subgroepen werden meerdere radiotracers tegelijk toegediend om de relatie van ^{111}In-GSAO opname en andere processen te onderzoeken. We lieten een In konijnen die zowel ^{111}In-GSAO en de ^{99m}Tc-sestamibi toegediend kregen, lieten we zien dat ^{111}In-GSAO accumuleert in het door ^{99m}Tc-sestamibi geïdentificeerde infarctgebied. In een tweede groep konijnen die zowel ^{99m}Tc-annexine als ^{111}In-GSAO toegediend kreeg, bleek opname van beide radiotracers sterk met elkaar te correleren. Tenslotte werd de specificiteit van ^{111}In-GSAO bevestigd door het uitblijven van accumulatie van ^{111}In-GSCA, een negatieve controletracer.

Vervolgens werden experimenten uitgevoerd in muizen met acuut hartinfarct dat werd geïnduceerd zoals hierboven beschreven, en in muizen met chronisch hartinfarct, waarbij de coronairarterie permanent werd afgebonden. Radiotracer kwantificatie liet zien dat ^{111}In-GSAO accumulatie in muizen met acuut myocardinfarct significant hoger is dan in muizen met chronisch myocardinfarct op de tijdstippen 2, 4 en 12 weken na afbinden van de coronairarterie.

Deze data laten zien dat ^{111}In-GSAO gebruikt kan worden om celdood in het acute myocardinfarct in beeld te brengen. De lage opname van ^{111}In-GSAO in muizen met een chronisch hartinfarct wordt waarschijnlijk verklaard door de beperkte mate van celdood op de langere termijn na start van het myocardinfarct.

In het onderzoek dat we beschrijven in hoofdstuk 5, hebben we ^{111}In-GSAO toegepast om de effectiviteit van minocycline als behandeling voor het myocardinfarct te bevestigen. Konijnen met een acuut hartinfarct werden verdeeld over een met minocycline behandelde groep en een controlegroep. *In vivo* en *ex vivo* SPECT beeldvorming en gamma counting lieten een lagere accumulatie van ^{111}In-GSAO in de met minocycline behandelde groep dan in onbehandelde controledieren. De verminderde mate van celdood in de minocycline groep werd bevestigd middels (immuno)histologische kleuringen.

List of publications

Journal articles

1. Boersma HH, **de Haas HJ**, Reutelingsperger CP, Slart RH. P-selectin imaging in cardiovascular disease: what you see is what you get? J Nucl Med 2011 Sep;52(9):1337-1338.

2. **de Haas HJ***, van den Borne SW*, Boersma HH, Slart RH, Fuster V, Narula J. Evolving role of molecular imaging for new understanding: targeting myofibroblasts to predict remodeling. Ann N Y Acad Sci 2012 Apr;1254:33-41.

3. Chen J, Petrov A, Yaniz-Galende E, Liang L, **de Haas HJ**, Narula J, et al. The impact of pressure overload on coronary vascular changes following myocardial infarction in rats. Am J Physiol Heart Circ Physiol 2013 Mar 1;304(5):H719-28.

4. **de Haas HJ***, Tahara N*, Mukherjee J*, Petrov AD, Tawakol A, Haider N, et al. 2-deoxy-2-[18F] fluoro-D-mannose positron emission tomography imaging in atherosclerosis. Nat Med 2014 Feb;20(2):215-219.

5. **de Haas HJ**, Arbustini E, Fuster V, Kramer CM, Narula J. Molecular imaging of the cardiac extracellular matrix. Circ Res 2014 Feb 28;114(5):903-915.

6. **de Haas HJ**, Narula J, Fuster V. From molecular imaging to pathogenesis and vice versa... Circ Cardiovasc Imaging 2014 Jul;7(4):581-585.

7. Friedman JI, Tang CY, **de Haas HJ**, Changchien L, Goliasch G, Dabas P, et al. Brain imaging changes associated with risk factors for cardiovascular and cerebrovascular disease in asymptomatic patients. JACC: Cardiovascular Imaging 2014;7(10):1039-1053.

8. **de Haas HJ***, Tahara N*, Zandbergen HR*, Petrov A, Pandurangi R, Yamaki T, et al. Noninvasive molecular imaging of cell death in myocardial infarction using 111In-GSAO. Sci Rep 2014 Oct 29;4:6826.

9. Golestani R, Mirfeizi L, Zeebregts CJ, Westra J, , Glaudemans AW, et al. Feasibility of [18F]-RGD for *ex vivo* imaging of atherosclerosis in detection of alphavbeta3 integrin expression. J Nucl Cardiol 2015 Dec;22(6):1179-1186.

10. Arias T, Petrov A, Chen J, de Haas H, Pérez-Medina C, Strijkers GJ, et al. Labeling galectin-3 for the assessment of myocardial infarction in rats. EJNMMI Research 2014;1(4):1-9.

11. **de Haas HJ**, Narula J. Playing slot to hitting the jackpot in molecular imaging: On probability of uncovering subcellular pathogenesis vs achieving clinical applicability. J Nucl Cardiol 2017 Mar 28. [Epub ahead of print]

12. **de Haas HJ***, Yamaki T*, Tahara N, Petrov A, Mohar D, Haider N, et al. Cardioprotection by minocycline in a rabbit model of ischemia/reperfusion injury: Detection of cell death by *in vivo* (111)In-GSAO SPECT. J Nucl Cardiol. 2018 Feb;25(1):94-100

* Co-first author

Book chapter

1. van der Veen E, de Haas HJ, Petrov AD, Reutelingsperger C, Kosterink J, Zeebregts CJ, et al. The story of myocardial infarction - before, when it strikes, and afterwards: A tale in images. In: Ahmadzadehfar H, Habibi E, editors. SPECT: technology, procedures and applications. 1st ed. Hauppauge, NY, USA: Nova Sciences Publishers, Inc.; 2013. p. 159-187.

Acknowledgements

It has taken a while, and now it's done. Doing a PhD, with its highlights and hardships has been a.. formative experience. Meeting people in and out of labs has been the best part. When I graduated medical school, thanking people was not allowed. I am glad that here I can try to express my gratitude to everyone (even remotely) involved in this project.

(co)promotors

Dear prof. dr. J. Narula, the amount I learned from you during the countless evenings and weekends discussing projects and finishing papers in your office is hard to exaggerate. The width and depth of your knowledge on basic and clinical (imaging) research, clinical cardiology, and two or three non-medical topics was shocking. Still what I will remember most is the personal pleasure of working with you and how I and everyone else always leaves your office with a smile. Working with you has been a privilege.

Dear prof. dr. R. Slart, dear Riemer, when in the early days of my PhD program I got the chance to move to NY and do my research, you were fully supportive of this. You yourself have been extremely active clinically as well as academically in Groningen and Twente, where you hold your chair. Still you were always ready to help in whichever way necessary, which is deeply appreciated. I thank you kindly for your friendliness, flexibility, expertise and encouragement.

Dear prof. dr. R. Dierckx, dear Rudi, we met infrequently, yet I could not have wished for a better presence in the background. With your knowledge, management skill and persona you are an inspiration. And you encouraged me throughout, came up with numerous fruitful ideas and solutions to problems I encountered, and facilitated me in every way possible. I am grateful for your support.

Dear dr. H. Boersma, dear Hendrikus. You are the one who brought me in touch with Prof. Narula before I had even been accepted to the MD/PhD program – I am grateful for your trust. Over the years we regularly talked over Skype or coffee and discussed the progress in detail. I have valued your advice, flexibility and constant support. Also with your friendliness, optimism, generosity, poetic perspective and personal communication style you have been a magnificent person to get to know.

Dear dr. R. Tio, dear René, I contacted you when after a JSM science course I decided to apply for the MD/PhD program. I am grateful for showing me the way to the cardiovascular imaging group Groningen. and the practical and intellectual support you have offered during the numerous lab meetings.

Reading committee

Dear prof. dr. C. Zeebregts, prof. dr. L. Hofstra and prof. dr. H. Strauss, thank you for meticulously reading my thesis and providing me with relevant comments and suggestions.

Funding

First of all, I want to thank Junior Scientific Masterclass, the institute behind the MD/PhD programme and all of its staff and associates, for their funding and support. For additional funding the Dutch Heart

6

Co authors

I want to thank all other co-authors and other collaborators, including dr. T. Yamaki, dr. N. Tahara, dr. H.R. Zandbergen, dr. S. van den Borne, prof. dr. C. Reutelingsperger, prof. dr. R. Hajjar, prof. dr. A. Tawakol, prof. dr. R. Virmani, prof. dr. L. Bosca, prof. dr. E. Arbustini, prof. dr. C. Kramer, dr. J. Friedman, dr. T Scarabelli, prof. dr. R. Henning, prof. dr. J.L. Hillebrand and prof. dr. Z. Fayad for their valued efforts.

New York supervisors

Prof. Dr. Fuster. I feel grateful to have worked in your department and benefited tremendously from attending the meetings and conferences you chaired. Your genius and passion as a clinician, researcher, educator and leader have left an indelible impression.

Prof. Dr. Partho Sengupta. Your energy, excitement, creativity and of course echocardiography expertise are unparalleled. It was a pleasure to have you as one of the supervisors in our group.

New York colleagues and friends

Artiom, my friend. You are undoubtedly the person I worked with the most during my PhD. Collaborating with you on innumerable animal experiments in the lab, analyzing the data and writing applications are good memories. With your kindness, humor, modesty, generosity and work ethic, you have been an enormously comforting presence. I hope you're still doing the yearly brewery thing.

Dear Dr. Haider, dear Nezam, during your time in New York, your bench has moved various times. Regrettably there was never enough room for it in our imaging lab. Still you dropped in every day and exposed us to your quirky humor. We laughed.

Dear Chiara, you were one of the first people I met in New York and I'm glad. You showed me Roberta's, the fat cat and Italian hand gestures. And it seems like we're colleagues again, as you are becoming a psychotherapist. Our paths will cross again!

Georg! I'm older now then you were when we met at Sinai. Your pubmed counter says 86. Seems like you're still doing well. Soon you'll move to Hawai and surf.

Zach, my friend! We didn't always agree on politics or ethics, but I certainly did approve of your behavior. I'm sure you will become a wonderful lawyer and have fun on the way.

Meagan! Smiles, 14 hour days, no you aren't aging fast, weekends looking at echo images, margaritas, Foster, that angry lady. You will find your garden.

Wissam, king of le bain. Go on.

And Giuseppe, Ayumi, Dong-Bin, Makoto, Sayyar, Mark, Teresa and the other Sinai Researchers, thanks for the shared jokes, complaints, walks in the park, and all.

PhD students, Msc students, roommates, technicians and all others from the department of Nuclear Medicine and Molecular Imaging in the UMCG

With its lively and personal atmosphere and stimulating academic climate, the department of NMBI (NGMB) has been a brilliant place to work. I'm sure I'm forgetting some names, but thanks everyone!

Nynke, Vincent, Luis, Andrea, Hannerieke, Erik, Martijn. You were a fantastic cardiovascular imaging group, have fun in life in and outside of cardiovascular imaging.

Andrea, Mehrsima, Valentina, Ines, Leyla (Sheida), Giuseppe, Janine, Anna, David, Jurgen, Bram, Silvana, Mark, Joris, Niek, Lara, Rodrigo and who am I forgetting? –thanks. Monday mornings, Friday evenings, Ni Hao dinners, EANM conferences, the coffeeroom, a complaint about dutch culture here and there.. The good times will be missed.

Reza! Meeting you in a basement as cardiovascular imaging as PhD students has been one of the happy coincidences. We didn't only discuss cardiovascular molecular imaging. I now carry with me a reservoir of Persian idioms (alright, insults) that I wish I could use more often. What can I say here. Cut your fingernails twice a week and don't go bald!

Maaike! Schatje. You were a fantastic distraction during the last months. Have fun at Harvard or MIT or whatever obscure institution you're at now. Ah and good luck with interacting with doctors!

And Carlos, Nobel laureate of being Cuban, salsa dancer, expert on national archetypes, latin mentality in a physics mind.. Our times in Groningen didn't overlap nearly as much as I would have wanted them to, but I am glad to have gained an amigo.

Dear Annegrit, once you answer your phone, the problem is solved. Thanks for solving many of mine.

Dear Sarita and Gerda, I wasn't always exactly organized when forms and documents were concerned.. Thanks for staying patient and saving me many times.

Friends, who helped by distraction

Tieme, Marije. You were there when times were tough. That is important, I will not forget. Ah and good times. The floating cultural platform, moving corpses, not calling the ambulance, the unexpected ambulance, videoclips in the forest, and at last leaving Groningen. Get rich and happy, tovarishchi.

Jan Wolter. Surfing oracle, ruminerende rouwdouwer. I am glad you've got one spare blanket now.

Freek. We met at science camp, studied Kant together and where I went for MDPhD, it says MDMA behind your name. Keep on making good choices, I hope they will involve moving back to Netherlands and having another Maredsous or four in de Mulder at some point.

Rosa. The coffees eased my cardiological problems, but the walks in the rain didn't always help on the existential ones. Enjoy the tropics, you deserve them!

Nel. An explosion of feeling, analysis, language. I am looking forward to your first collection of stories. In the meantime let's waste some more time.

Marco. My oldest friend. Lots of skateboarding, beaches, tents, that photograph. Did you see the stylish kids in the riots?

Anne. A person I care about (ha). You were there during the first - what is it - four years of my PhD. And now you are married! So finalizing the PhD is not the only thing that did not exactly go according to schedule. Three kisses, I wish you happiness.

6

Paranymphs

Jos. Jossie. I don't think we expected this when we were eating Ben&Jerry's at Albert Heijn ten years ago. Ha yes it happened, it's TEN YEARS ago. It's not as bad as we thought eh.

Since then we have shared many things. I am glad to have you as my paranymph, Jos.

Marieke. Proud to have you as my paranymph – thank you – but you're mostly sister. Read on.

Family

Lieve Anja, Moeder. Where to begin. You are always there, not just for me. I deeply appreciate your support and love. Elsschot said it better. Marieke, Mariek, zus. For lack of a father, I will do the pride thing. It's easy, you're terrific. Mem en zus, we hit a few bumps in the road over the past few years, and I could not be happier with how we stuck together.

Olaf. I can only mention him because he died. He was there when I got my MD and didn't care that much about the PhD, so no tears there. But discussing psychiatry would have been nice. Or taking a walk through Amsterdam. I miss him.

And Hasse-Eva! I am glad we did go for that coffee or whiskey.

Curriculum vitae

Hans Joachim de Haas was born in Scheveningen on January 29th 1988. After graduating from high school, he started his medical studies at the University of Groningen (UG) in 2006. He also took courses in philosophy and obtained a BA in this field with a thesis on explanatory models in psychiatry. In 2010 he was admitted to the MD/PhD program of the UG, which allowed him to combine his clinical rotations with research in cardiovascular molecular imaging. He soon transferred to New York, where he worked as visiting researcher at the Icahn School of Medicine at Mount Sinai. After returning to the Netherlands, he started his clinical rotations and obtained is medical license in 2015. His first clinical job was at the department of cardiology at the University Medical Center Groningen. He finally decided to pursue a career in psychiatry, and worked at mental health services in Groningen and Amsterdam. He will start his residency training in psychiatry at Arkin Amsterdam in April 2018.

6